Advanced Engineering Research

(Rostov-on-Don)

Mechanics

Machine Buiding
and Machine Science

Information Technology,
Computer Science
and Management

The journal is aimed at informing the readership about the latest achievements and prospects in the field of mechanics, mechanical engineering, computer science and computer technology. The publication is a forum for cooperation between Russian and foreign scientists, it contributes to the convergence of the Russian and world scientific and information space.

The journal is included in the List of the leading peer-reviewed scientific publications (Higher Attestation Commission under the Ministry of Science and Higher Education of the Russian Federation), where basic scientific results of dissertations for the degrees of Doctor and Candidate of Science in scientific specialties and their respective branches of science should be published.

The journal publishes articles in the following fields of science:

– Theoretical Mechanics, Dynamics of Machines (Engineering Sciences)
– Deformable Solid Mechanics (Engineering, Physical and Mathematical Sciences)
– Mechanics of Liquid, Gas and Plasma (Engineering Sciences)
– Mathematical Simulation, Numerical Methods and Program Systems (Engineering Sciences)
– System Analysis, Information Management and Processing, Statistics (Engineering Sciences)
– Automation and Control of Technological Processes and Productions (Engineering Sciences)
– Software and Mathematical Support of Machines, Complexes and Computer Networks (Engineering Sciences)
– Computer Modeling and Design Automation (Engineering, Physical and Mathematical Sciences)
– Computer Science and Information Processes (Engineering Sciences)
– Machine Science (Engineering Sciences)
– Machine Friction and Wear (Engineering Sciences)
– Technology and Equipment of Mechanical and Physicotechnical Processing (Engineering Sciences)
– Engineering Technology (Engineering Sciences)
– Welding, Allied Processes and Technologies (Engineering Sciences)
– Methods and Devices for Monitoring and Diagnostics of Materials, Products, Substances and the Natural Environment (Engineering Sciences)
– Hydraulic Machines, Vacuum, Compressor Equipment, Hydraulic and Pneumatic Systems (Engineering Sciences)

Contents

Содержание

MECHANICS
МЕХАНИКА

Check for updates

Assessment of Dynamic States of Railway Vehicles: Structural Mathematical Modeling

Roman S. Bolshakov [ID] ✉**, Valery E. Gozbenko** [ID]**, Vuong Quang Truc** [ID]
Irkutsk State Transport University, Irkutsk, Russian Federation
✉ bolshakov_rs@mail.ru

EDN: PEUPEC

Abstract

Introduction. The speed rise of railway transport and an increase in the loads on the axles of wheelsets necessitate the modernization of the existing fleet. Scientific studies in the field of rolling stock dynamics are aimed at taking into account the oscillatory processes that occur during the movement of railway vehicles in a traditional design. The attachment of supplementary elements was considered at the coupling level of two cars and the attachment of a third trolley in the center of gravity of the railway platform. The scientific literature has not paid enough attention to the construction of mathematical models that make it possible to assess the dynamic states of such constructive solutions. The objective of this study is to create a method for evaluating the dynamic conditions of a car. The situation is considered when an additional set of mass-inertial and elastic elements is introduced into its structure, and the general dynamic condition of the vehicle depends on the adjustment of their parameters.

Materials and Methods. The basic research tool is the structural mathematical modeling, which is based on an approach where the source design scheme is a mechanical oscillatory system in the form of a solid body on elastic supports with supplementary typical elements introduced into its structure. The dynamic analogue of the calculation scheme used is the block diagram of the automatic control system, the use of which provides detailing the connections between typical elastic and mass-inertia elements.

Results. A method for estimating the dynamic states of railway vehicles is proposed. It is based on the construction of mathematical models, taking into account the introduction of an additional structure of mass-inertia and elastic elements. The impact of additional parameters on the dynamic condition of the vehicle is investigated. Analytical relations have been obtained that provide reducing the dynamic loads on the major structural elastic elements when changing the corresponding parameters of a technical object. The transfer function of interpartial relations is given, which provides controlling the interaction between the coordinates of the vehicle movement under the action of two kinematic disturbances of the in-phase type.

Discussion and Conclusion. The generated mathematical model provides for assessment, monitoring and control of the dynamic state of the vehicle under conditions of kinematic disturbances. The research results can be used to modernize existing vehicles and create new ones with improved dynamics.

Keywords: vehicle dynamics, dynamic condition, structural mathematical modeling, block diagram

Mechanics

Оригинальное эмпирическое исследование

Возможности оценки динамических состояний железнодорожных транспортных средств: структурное математическое моделирование

Р.С. Большаков ⓘ ✉, **В.Е. Гозбенко** ⓘ, **К.Ч. Выонг** ⓘ

Иркутский государственный университет путей сообщения, г. Иркутск, Российская Федерация

✉ bolshakov_rs@mail.ru

Аннотация

Введение. Увеличение скоростей движения железнодорожного транспорта и повышение нагрузок на оси колесных пар обуславливают необходимость модернизации существующего парка. Научные исследования в области динамики подвижного состава направлены на учёт колебательных процессов, возникающих при движении железнодорожных транспортных средств в традиционном конструктивном исполнении. Присоединение дополнительных элементов рассматривалось на уровне сцепки двух вагонов и присоединении третьей тележки в центре тяжести железнодорожной платформы. Построению математических моделей, позволяющих оценить динамические состояния таких конструктивных решений, в научной литературе не уделено достаточно внимания. Цель данного исследования — создать метод оценки динамических состояний вагона. Рассматривается ситуация, когда в его структуру вводится дополнительная совокупность масс-инерционных и упругих элементов, причем от корректировки их параметров зависит общее динамическое состояние транспортного средства.

Материалы и методы. Базовым инструментом проведения исследований является структурное математическое моделирование, в основе которого лежит подход, когда исходная расчетная схема представляет собой механическую колебательную систему в виде твердого тела на упругих опорах с дополнительной введёнными в её структуру типовыми элементами. Динамическим аналогом используемой расчетной схемы является структурная схема системы автоматического управления, применение которой позволяет детализировать связи между типовыми упругими и масс-инерционными элементами.

Результаты исследования. Предложен метод оценки динамических состояний железнодорожных транспортных средств, основанный на построении математических моделей, с учетом введения дополнительной структуры масс-инерционных и упругих элементов. Исследовано влияние дополнительных параметров на динамическое состояние транспортного средства. Получены аналитические соотношения, позволяющие при изменении соответствующих параметров технического объекта снизить динамические нагрузки на основные конструктивные упругие элементы. Приведена передаточная функция межпарциальных связей, позволяющая контролировать взаимодействие между координатами движения транспортного средства при действии двух кинематических возмущений синфазного типа.

Обсуждение и заключение. Сформированная математическая модель позволяет оценить динамическое состояние железнодорожного транспортного средства в условиях действия кинематических возмущений. Результаты исследований могут быть применены при модернизации существующих и создании новых транспортных средств с улучшенной динамикой.

Ключевые слова: динамика транспортных средств, динамическое состояние, структурное математическое моделирование, структурная схема

Introduction. The expansion of technical-and-economic ties at the interregional level, providing the growth of the country's industrial engineering potential, and maintaining the growing system of international trade and commercial relations largely depends and relies on rail transport [1]. The rail traffic volume is constantly increasing. This drives the need to take into account the perverse effects of increased dynamic loads [2], which directly affect the reliability of operation of both rolling stock and the track structure. Despite such negative factors, it is necessary to fulfill the planned indicators, which include an increase in the service speed, compliance with weight and length standards for trains, increasing axle load to 30 tons or more. This reflects the real demands of the development of the Russian economy and stimulates the creation of new more powerful locomotives, the renewal of the fleet of rolling stock, and the modernization of track facilities [3]. At the same time, the possibility of negative consequences of the intensification of transportation processes should also be considered. One of the major issues is the increase in the rate of wear of the track structure with the corresponding resulting difficulties [4].

Currently, particular attention is being paid to the development of a methodology for assessing the dynamic condition of rolling stock, the interaction of technical means and rail tracks, energy savings, and improving the reliability and safety of transportation processes. The mathematical modeling methodology is described, e.g., in [5]. At the same time, there are other possibilities for finding rational solutions [6]. It is important to pay attention to the modernization of the existing fleet of freight wagons, whose operation is no longer effective under increased loads [7]. One of the approaches that could be adopted for the development is the concept of installing an additional two-axle bogie for freight 4ax wagons [8]. In this case, we can expect a more uniform distribution of the load on the track structure, as well as the possibility of increasing the weight of the transported goods while maintaining the regulations for axial load values within 22 tons [9]. The unevenness of the wheel-rail contact parameters initiates the oscillatory movements of the car, which in turn forms the oscillatory movements of the car body. The oscillation process is also formed by the conditions of interaction of wagons inside the train [10]. In this case, dynamic restraint forces occur, superimposing on the static components of the overall reaction, which can significantly increase the level of dynamic interactions in the wheel-rail contact [11, 12]. However, the possibilities of structural mathematical modeling in assessing the dynamic states of railway vehicles with the introduction of additional links have not yet been given enough attention. Therefore, the objective of this study is to form a method for evaluating the dynamic states of a railway vehicle when introducing an additional set of mass-inertial and elastic elements into its structure, the correction of the parameters of which would affect the overall dynamic state of the vehicle.

Materials and Methods. The methodological basis of the research is the structural theory of vibration isolation systems, which provides for the accurate assessment of the dynamic properties of a railway vehicle in a linear formulation, taking into account concentrated parameters and small oscillations relative to the position of static equilibrium or a steady-state process. The design scheme is a mechanical vibratory system with dynamic equivalent in the form of a block diagram of an automatic control system. This makes it possible to detail the connections between the elements of the vehicle, as well as to use methods characteristic of the theory of automatic control (transfer functions, transformations of structural circuits, convolution and simplification, frequency characteristics) [13].

Standard design schemes of freight railway vehicles are described by well-known calculation schemes, and their dynamic features can be estimated using linear calculation schemes. The article considers a railway vehicle in the form of a four-axle freight wagon designed for the transportation of heavy goods such as coal, ore, sand, rolled metal, small-sized metal structures, etc. (Fig. 1).

Mechanics
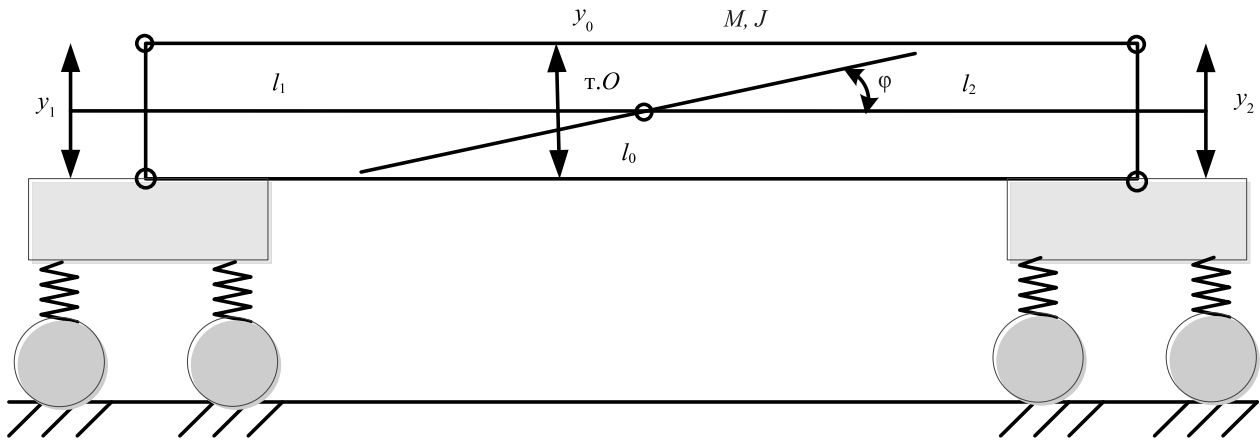
Fig. 1. Schematic diagram of a four-axle freight wagon

The structure of the presented railway vehicle contains a body with mass M and moment of inertia J. It is based on two four-wheel bogies, conventionally represented as a set of mass-inertial and elastic elements. The dynamic features of the system under consideration show the excessive impact on the structural elements of the bogies of the railway vehicle. In this regard, to improve its dynamic properties, a third two-axle truck is additionally introduced into the suspension structure, which is located in the center of the wagon (Fig. 2).
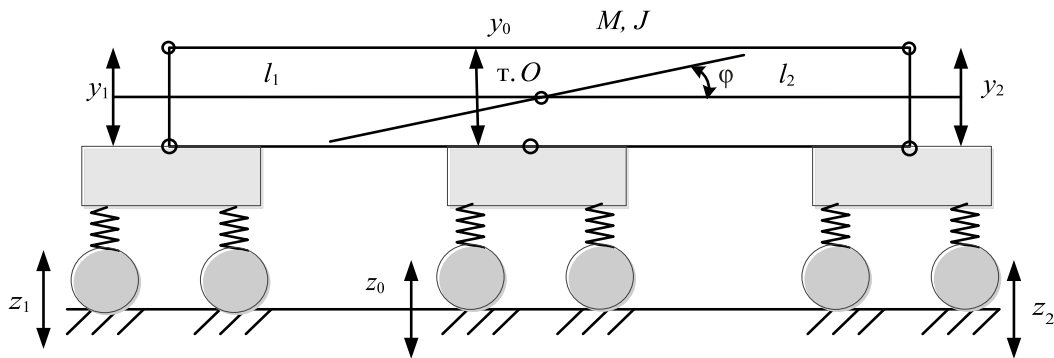
Fig. 2. Schematic diagram of a six-axle freight car

With a car's own weight of about 23 tons, and an axial load of 22 tons, this can provide an increase in the weight of transported goods by approximately 20 tons, i.e., significantly increase the efficiency of transportation processes without creating excessive dynamic loads on the track structure (TS). The practical implementation of the proposed approach requires the modernization of the design of a standard wagon. The modernization consists in creating an additional bogie attachment unit to reduce the load on the axle of a freight wagon by introducing an additional two-axle track. The upgrading of the attachment unit is carried out in the same structural and technical forms as the fastening using pins in two "standard" two-axle bogies, i.e., through the installation of over- and underpin bolsters with the corresponding standard-type pin assembly.

The proposed method of increasing the efficiency of using four-axle freight cars under conditions of additional loads is aimed at solving the problem of increasing the load on the axle of the wheelset to 30 tons, and speeding up the trains. This is achieved through upgrading a typical freight car by installing an additional two-axle bogie with an appropriate device that provides conditions for its dynamic interaction with the frame structure of the freight car.

The installation of an additional two-axle bogie by redistributing the load between a common set of wheelsets provides the possibility of transporting heavy loads while reducing the load on the axle. This maintains better operating conditions for the track and the superstructure while maintaining an acceptable length of the train.

It is assumed that the pin assembly has an elastic rubber gasket that provides cushioning for the interaction of the bogie and the frame of the wagon body. At the same time, it is not supposed to upgrade the wheels of the wheelsets. Only the form of wiring of the elements of the "regular" pneumatic braking system and the configuration of the supply of pneumatic pipelines are changed.

Research Results. The design scheme of the considered railway vehicle in the first approximation can be represented as a mechanical oscillatory system consisting of a solid body with mass m and moment of inertia J, based on three elastic elements with stiffness k_1, k_0, k_2. Kinematic effects are represented by in-phase harmonic functions of the same frequency (Fig. 3).
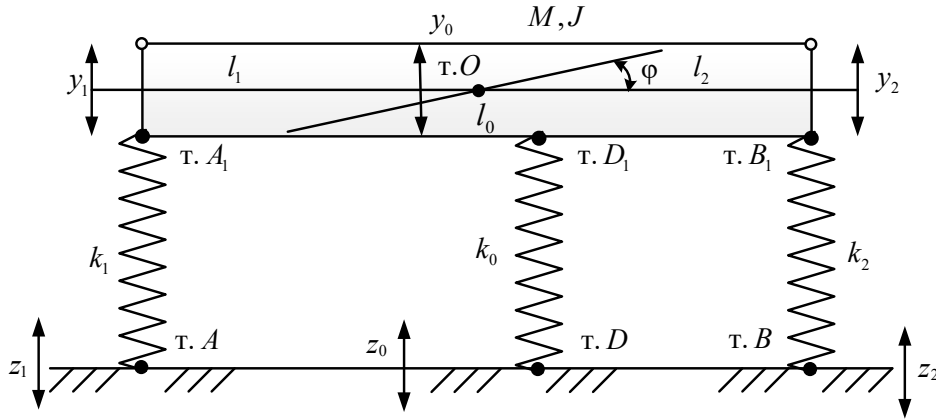
Fig. 3. Design scheme of a railway vehicle
under kinematic disturbance (z_1, z_2, z_0)

The center of mass of the system — point O is located at distances l_1 and l_2 from the ends of the solid (points A_1, B_1). The element with stiffness k_0 is fixed at points D and D_1; distance OD_1 is indicated as l_0. The movement of the system is considered in coordinates y_1, y_2 and y_0, φ, associated with a fixed basis. The calculations use the following ratios:

$$y_0 = ay_1 + by_2,\ \phi = c(y_2 - y_1),\ y_1 = y_0 - l_1\phi,\ y_2 = y_0 + l_2\phi,$$
$$y_D = y_0 + l_1\phi,\ a = \frac{l_2}{l_1 + l_2},\ b = \frac{l_1}{l_1 + l_2},\ c = \frac{1}{l_1 + l_2}. \tag{1}$$

Lagrange formalism is used to derive differential equations of motion [14], which requires the construction of expressions for kinetic and potential energies. In this case, we have:

$$T = \frac{1}{2}m\left(ay_1' + by_2'\right)^2 + Jc^2\left(y_2' - y_1'\right)^2, \tag{2}$$

$$\Pi = \frac{1}{2}k_1(y_1 - z_1)^2 + \frac{1}{2}k_0(y_D - z_0)^2 + \frac{1}{2}k_2(y_2 - z_2)^2. \tag{3}$$

Note that potential energy (3) can also be written as:

$$\Pi = \frac{1}{2}k_1(y_1 - z_1)^2 + \frac{1}{2}k_2(y_2 - z_2)^2 + \frac{1}{2}k_0\left[ay_1 + by_2 + l_0c(y_2 - y_1) - z_0\right]^2 =$$
$$\frac{1}{2}k_1(y_1 - z_1)^2 + \frac{1}{2}k_2(y_2 - z_2)^2 + \frac{1}{2}k_0\left[a_1y_1 + b_1y_2 - z_0\right]^2, \tag{4}$$

where $a_1 = a - l_0c$, $b_1 = b + l_0c$.

The system of equations of motion in coordinates y_1, y_2 in the time domain takes the form:

$$y_1''\left(ma^2 + Jc^2\right) + y_1\left(k_1 + k_0a_1^2\right) - y_2''\left(Jc^2 - mab\right) + y_2k_0a_1b_1 = k_1z_1 + k_0a_1z_0, \tag{5}$$

$$y_2''\left(mb^2 + Jc^2\right) + y_2\left(k_2 + k_0b_1^2\right) - y_1''\left(Jc^2 - mab\right) + y_1k_0a_1b_1 = k_2z_2 + k_0b_1z_0. \tag{6}$$

After applying the Laplace integral transformations under zero initial conditions [15], the system of equations (5), (6) can be represented in the operator form:

$$\overline{y}_1\left[\left(ma^2 + Jc^2\right)p^2 + k_1 + k_0a_1^2\right] - \overline{y}_2\left[\left(Jc^2 - mab\right)p^2 - k_0a_1b_1\right] = k_1\overline{z}_1 + k_0a_1\overline{z}_0, \tag{7}$$

$$\overline{y}_2\left[\left(mb^2 + Jc^2\right)p^2 + k_2 + k_0b_1^2\right] - \overline{y}_1\left[\left(Jc^2 - mab\right)p^2 - k_0a_1b_1\right] = k_2\overline{z}_2 + k_0b_1\overline{z}_0, \tag{8}$$

where $p = j\omega$ — complex variable ($j = \sqrt{-1}$), indicator $<\!\!-\!\!>$ above the variable means its Laplace image [5].

Mechanics

On the basis of (7), (8), in accordance with the provisions of the method of structural mathematical modeling [5], a structural mathematical model in the form of a block diagram is constructed, which is dynamically equivalent to an automatic control system (Fig. 4).
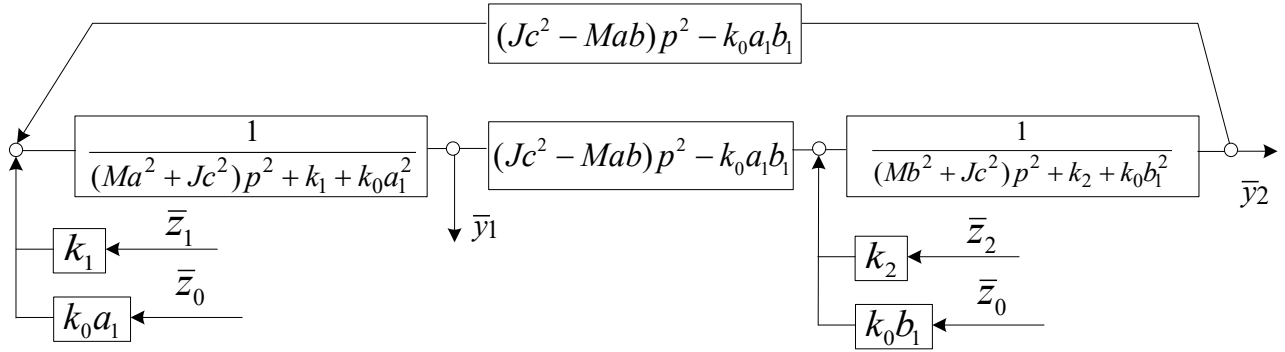
Fig. 4. Structural mathematical model of a railway vehicle

Discussion and Conclusion. The feature of the system is that it has two partial blocks, each of which determines the corresponding partial frequencies:

$$n_1^2 = \frac{k_1 + k_0 a_1^2}{ma^2 + Jc^2}, \tag{9}$$

$$n_2^2 = \frac{k_2 + k_0 b_1^2}{mb^2 + Jc^2}, \tag{10}$$

which, in turn, determine the boundaries of the location of the natural oscillation frequencies of the system as a whole:

$$\omega_{1\text{соб}}^2 < n_1^2 < n_2^2 < \omega_{2\text{соб}}^2, \tag{11}$$

where $\omega_{1\text{соб}}$, $\omega_{2\text{соб}}$ — natural oscillation frequencies of the system. When operating on them, resonant modes may occur.

Among the features of the system there are several simultaneously acting external disturbances. Assuming, for the sake of simplification, that $\bar{z}_1 = \bar{z}_2 = \bar{z}_0$ (quite acceptable at the stages of preliminary dynamic estimates), we consider that force factors act on the input of the first and second partial blocks:

$$\bar{Q}_1 = \bar{z}(k_1 + k_0 a_1), \tag{12}$$

$$\bar{Q}_2 = \bar{z}(k_2 + k_0 b_1). \tag{13}$$

Using the block diagram in Figure 4, we write down the expressions for the transfer functions, assuming that there is a relationship between the external perturbation factors formed by the ratio:

$$\bar{Q}_1 = \bar{Q}, \bar{Q}_2 = \alpha\bar{Q}, \tag{14}$$

$$W_1(p) = \frac{\bar{y}_1}{\bar{z}} = \frac{(k_1 + k_0 a_1)\left[(mb^2 + Jc^2)p^2 + k_2 + k_0 b_1^2\right] + \alpha(k_2 + k_0 b_1)\left[(Jc^2 - mab)p^2 - k_0 a_1 b_1\right]}{A(p)}, \tag{15}$$

$$W_2(p) = \frac{\bar{y}_2}{\bar{z}} = \frac{\alpha(k_2 + k_0 b_1)\left[(ma^2 + Jc^2)p^2 + k_1 + k_0 a_1^2\right] + (k_1 + k_0 a_1)\left[(Jc^2 - mab)p^2 - k_0 a_1 b_1\right]}{A(p)}, \tag{16}$$

where

$$A(p) = \left[(ma^2 + Jc^2)p^2 + k_1 + k_0 a_1^2\right]\left[(mb^2 + Jc^2)p^2 + k_2 + k_0 b_1^2\right] - \left[(Jc^2 - mab)p^2 - k_0 a_1 b_1\right] \tag{17}$$

is the frequency characteristic equation of the system.

The numerator of the transfer functions in expressions (15), (16) determines the modes of dynamic vibration damping, which can be detailed from the equations obtained by "zeroing" numerators (15), (16):

$$\omega_{1\text{дин}}^2 = \frac{\left(k_1 + k_0 a_1\right)\left(k_2 + k_0 b_1^2\right) - \alpha\left(k_2 + k_0 b_1\right)k_0 a_1 b_1}{\left(k_1 + k_0 a_1\right)\left(mb^2 + Jc^2\right) + \alpha\left(k_2 + k_0 b_1\right)\left(Jc^2 - mab\right)}, \tag{18}$$

$$\omega_{2\text{дин}}^2 = \frac{\left(k_2 + k_0 b_1\right)\left(k_1 + k_0 a_1^2\right) - \alpha\left(k_1 + k_0 a_1\right)k_0 a_1 b_1}{\alpha\left(k_1 k_2 + k_0 b_1\right)\left(ma^2 + Jc^2\right) + \left(k_1 k_2 + k_0 a_1\right)\left(Jc^2 - mab\right)}. \tag{19}$$

It follows from expressions (18), (19) that in a system with two degrees of freedom, in the presence of two interconnected disturbing factors, dynamic vibration damping modes at two frequencies may occur, whose parameters depend on the values of connectivity coefficient α. This coefficient can take negative, positive and zero values.

The analysis of the structural mathematical model (Fig. 4) also implies the possibility of a special dynamic mode at the frequency:

$$\omega_{\text{спец}}^2 = \frac{k_0 a_1 b_1}{Jc^2 - mab}, \tag{20}$$

when the partial blocks get the possibility of disconnection. In this case, the system (Fig. 3) splits into two autonomous blocks, which do not create situations of interaction of partial structures.

The implementation of this mode can cause a significant difference in the values of deviations at points A_1 and B_1, and a "spread" of values of the dynamic reactions at points A_1, B_1 and D_1. The determination of dynamic reactions at points A, B and D can be implemented according to the methodology described in [14], in which the dynamic reaction is defined as the product of a dynamic displacement (e.g., points A_1, B_1 and D_1) by the value of the reduced dynamic stiffness.

For coordinate $\bar{y}_1$, the dynamic offset is determined from the expression for transfer function (15), and for coordinate $\bar{y}_2$ — from expression (16). The frequency characteristic equation is used to determine the reduced dynamic stiffness (17):

$$k_{\text{пр1}}(p) = k_1 + \frac{k_0 a^2 a_1}{\left(mb^2 + Jc^2\right)p^2 + k_2 + k_0 b_1^2} - \frac{\left[\left(Jc^2 - mab\right)p^2 - k_0 a_1 b_1\right]^2}{\left(mb^2 + Jc^2\right)p^2 + k_2 + k_0 b_1^2}. \tag{21}$$

Similarly, the value of the reduced dynamic stiffness in coordinate $\bar{y}_2$ can be found:

$$k_{\text{пр2}}(p) = k_2 + \frac{k_0 b^2 b_1}{\left(ma^2 + Jc^2\right)p^2 + k_1 + k_0 a_1^2} - \frac{\left[\left(Jc^2 - mab\right)p^2 - k_0 a_1 b_1\right]^2}{\left(ma^2 + Jc^2\right)p^2 + k_1 + k_0 a_1^2}. \tag{22}$$

To determine the specific values $\bar{k}_{\text{пр1}}(p)$ and $\bar{k}_{\text{пр2}}(p)$, it is necessary to find the value of frequency ω^2, which is determined from the condition that $\bar{y}_2 / \bar{y}_1 = 1$. More generally, it is assumed that:

$$\frac{\bar{y}_2}{\bar{y}_1} = \gamma, \tag{23}$$

where γ — coefficient of connectivity of the movement of elements by coordinates $\bar{y}_1$ and $\bar{y}_2$. Thus, this coefficient (for the case γ=1) can be written as:

$$\gamma = \frac{\bar{y}_2}{\bar{y}_1} = \frac{\alpha\left(k_2 + k_0 b_1\right)\left[\left(ma^2 + Jc^2\right)p^2 + k_1 + k_0 a_1^2\right] + \left(k_1 + k_0 a_1\right)\left[\left(Jc^2 - mab\right)p^2 - k_0 a_1 b_1\right]}{\left(k_1 + k_0 a_1\right)\left[\left(mb^2 + Jc^2\right)p^2 + k_2 + k_0 b_1^2\right] + \alpha\left(k_2 + k_0 b_1\right)\left[\left(Jc^2 - mab\right)p^2 - k_0 a_1 b_1\right]}. \tag{24}$$

Taking specific values γ, it is possible to find the oscillation frequencies for the motion of the object in question in coordinates $\bar{y}_1$ and $\bar{y}_2$. Specifically, at $\gamma = 1$, the frequency of translational vertical vibrations of a solid is determined from the expression:

Mechanics

$$\omega^2 = \frac{\overline{y}_2}{\overline{y}_1} = \frac{\alpha\left(k_2 + k_0 b_1\right)\left(k_1 + k_0 a_1^2\right) - \left(k_1 + k_0 a_1\right)k_0 a_1 b_1 + \left(k_1 + k_0 a_1\right)k_0 a_1 b_1 -}{\alpha\left(k_2 + k_0 b_1\right)\left(ma^2 + Jc^2\right) + \left(k_1 + k_0 a_1\right)\left(Jc^2 - mab\right) -} \cdots$$

$$\cdots \frac{-\left(k_1 + k_0 a_1\right)\left(k_2 + k_0 b_1^2\right) - \left(k_2 + k_0 b_1\right)\left(k_1 + k_0 a_1^2\right) + \alpha\left(k_2 + k_0 b_1\right)k_0 a_1 b_1}{-\left(k_1 + k_0 a_1\right)\left(mb^2 + Jc^2\right) - \alpha\left(k_2 + k_0 b_1\right)\left(Jc^2 - mab\right)}.$$

(25)

Frequency ω of in-phase harmonic disturbances $z_1(t)$, $z_2(t)$ and $z_0(t)$ provides the motion of a solid body at $\varphi = 0$, i.e., $\overline{y}_1 = \overline{y}_2 = \overline{y}_D$. For other values γ ($\gamma \neq 1$), $\overline{y}_1$ and $\overline{y}_2$ are determined, and on their basis, for geometric reasons, value $\overline{y}_D$ is determined. For a solid body with known $\overline{y}_1$ and $\overline{y}_2$, the position of the center of rotation (or oscillations) can be easily found [12].

The dynamic constraint reactions $\overline{R}_{A1}$, $\overline{R}_{B1}$ and $\overline{R}_{D1}$ can be found in the first approximation by the formulas:

$$\overline{R}_{A1} = k_1 \overline{y}_1, \ \overline{R}_{B1} = k_2 \overline{y}_2, \ \overline{R}_{D1} = k_0 \overline{y}_D.$$

In general, dynamic reactions are determined using dynamic displacements $\overline{y}_1, \overline{y}_2, \overline{y}_D$, that are defined by expressions (15), (16). As for the dynamic displacement at point D, expression $\overline{y}_D = a_1 \overline{y}_1 + b_1 \overline{y}_2$ is used, whose parameters are determined by the above values. In expressions (15), (16), data on the connectivity of force factors of influence (parameter α) can be entered. To obtain specific data on the values of dynamic reactions, frequency parameters are introduced at which the ratio of oscillation amplitudes $\overline{y}_2$ and $\overline{y}_1$ is implemented through the coefficient of coupling of oscillation amplitudes γ.

The overall restraint force at points A, B and D is determined by the sum of two components: static and dynamic. The static component can be found from the expression for the transfer functions of dynamic reactions at $p = 0$ and setting the parameters of the static load (weight of the wagon and the cargo being transported). With the intensive development of oscillatory processes, when fluctuations in coordinates $\overline{y}_1, \overline{y}_2, \overline{y}_D$ increase, the overall reaction can vary significantly and differ from the static restraint force. In the presence of a dynamic component, the overall reaction can take on various values, in particular, zero or negative.

The mathematical model formed within the framework of the proposed method is indicated by expression (25). It provides assessing the dynamic state of railway vehicles when additional connections are introduced into their structure to form a set of recommendations for obtaining stable modes of operation. The investigation of the features of the system using approaches typical of structural mathematical modeling allows us to consider in detail the connections between the elements. With regard to the technical object in question, this makes it possible to adjust the dynamic state of the technical object, based on varying the parameters of the set of additionally introduced elements, to reduce the load on the main parts of the suspension, as well as to establish the presence of natural frequencies and frequencies of dynamic vibration damping in the system.

In the future, it is planned to conduct research on the introduction of dampers and motion conversion devices into the structure of the vehicle to assess the possibilities of structural mathematical modeling. Another interesting area is the assessment of the possibilities of changing dynamic reactions depending on external actions, which will allow us to assess the efforts exerted on various elements of the vehicle suspension.

References

1. Kossov VS, Knyazev DA, Krasyukov NF, Makhutov NA, Gadenin MM. Regulatory Framework for Ensuring the Safe Operation of Railway Equipment Based on the Service Life of Load-Bearing Structures. *World of Transport and Transportation*. 2023;21(3):106–114. https://doi.org/10.30932/1992-3252-2023-21-3-10

2. Makhutov NA, Lapidus BM, Gadenin MM, Titov EYu. Tasks and Prospects for the Development of Scientific Research within the Framework of Cooperation between JSC "Russian Railways" and the Russian Academy of Sciences. *Zheleznodorozhnyi transport*. 2023;(7):6–11. (In Russ.).

3. Lapidus BM. Tasks of Advanced Development of Russian Railways. *Zheleznodorozhnyi transport.* 2023;(2):4–14. (In Russ.).

4. Kolesnikov VI, Migal YuF, Kolesnikov IV, Sitrev AP, Voropaev AP. Increasing the Wear Resistance of Heavily Loaded Tribosystems by Forming the Structure and Properties of Their Contact Surfaces. *Nauka Yuga Rossii (Science in the South Russia)*. 2022;18(4):59–65. (In Russ.).

5. Eliseev SV, Eliseev AV, Bolshakov RS, Khomenko AP. *Methodology of System Analysis in Problems of Assessment, Formation and Control of the Dynamic State of Technological and Transport Machines*. Moscow: "Nauka" Publ. House; 2021. 679 p. (In Russ.).

6. Romen YuS, Belgorodtseva TM, Dediaev MV. Condition of Wagon Wheels and Axles and Interaction Forces in the "Crew – Track" System. *Transport of Russian Federation*. 2021;95(4):36–40.

7. Savoskin AN, Romen YuS, Akashev MG. A Useful Random Process of Acting Lateral Forces between a Wheel and Rail and Its Probabilistic Characteristics. *Vestnik Mashinostroeniya*. 2022;(4):14–19. https://doi.org/10.36652/0042-4633-2022-4-14-19

8. Ermolenko IYu, Morozov DV, Astashkov NP. Influence of Longitudinal Loads on Traffic Safety When Operating on Mountain Passway Sections. *Vestnik RGUPS, Rostov State Transport University*. 2021;82(2):104–111. https://doi.org/10.46973/0201-727X_2021_2_104

9. Buldaev AS, Khishektueva IKhD, Anakhin VD, Dambaev ZhG. On One Method for Solving the Problem of Identifying Dynamic Systems. *Bulletin of Buryat State University. Mathematics, Informatics*. 2020;(4):14–25. https://doi.org/10.18101/2304-5728-2020-4-14-25

10. Buldaev AS. Projection Perturbation Methods in Optimization Problems of Controlled Systems. *Bulletin of Irkutsk State University. Series: Mathematics*. 2014;(8):29–43.

11. Mizhidon AD, Khamkhanov AK. A Hybrid System of Differential Equations Describing a Rigid Body Attached to Two Elastic Rods. *Bulletin of Buryat State University. Mathematics, Informatics*. 2022;(4):38–47. https://doi.org/10.18101/2304-5728-2022-4-38-47

12. Eliseev AV, Mironov AS, Eliseev SV. Formation of Mathematical Models of Vibration Interactions of Elements of Technical Means of Transport and Technological Purposes. *Proceedings of Voronezh State University. Series: Systems Analysis and Information Technologies*. 2022;(1):32–42. https://doi.org/10.17308/sait.2022.1/9199

13. Eliseev AV, Kuznetsov NK, Eliseev SV. New Approaches to the Estimation of Dynamic Properties of Vibrational Structures: Frequency Functions and Connectivity of Movements. *Trudy MAI*. 2021;(120):08. https://doi.org/10.34759/trd-2021-120-08

14. Eliseev AV, Kuznetsov NK. The Concept of a Generalized Lever in Assessing the Dynamic States of Mechanical Oscillatory Systems under Conditions of Connected Vibration Loads. *Systems. Methods. Technologies*. 2023;59(3):7–12. https://doi.org/10.18324/2077-5415-2023-3-7-12

15. Kashuba VB, Bolshakov RS, Mozalevskaya AK, Nguyen Huynh Duc. Identification of Ties Responses between Vibroprotection Systems Elements on Base of Structural Transformation Method. In: *Proc. XV All-Russian Sci.-Tech. Conference with International Participation "Mechanical Engineers to XXI Century".* Bratsk: BrSU; 2016. P. 295-300.

About the Authors:

Roman S. Bolshakov, Cand.Sci. (Eng.), Associate Professor of the Operational Work Management Department, Irkutsk State Transport University (15, Chernyshevskogo Str., Irkutsk, 664074, Russian Federation), SPIN-code: 6214–3569, ORCID, ScopusID, bolshakov_rs@mail.ru

Valery E. Gozbenko, Dr.Sci. (Eng.), Professor of the Mathematics Department, Irkutsk State Transport University (15, Chernyshevskogo Str., Irkutsk, 664074, Russian Federation), SPIN-code: 4307–8922, ORCID, ScopusID, vgozbenko@yandex.ru

Mechanics

Vuong Quang Truc, postgraduate of the Department of Physics, Mechanics and Instrumentation, Irkutsk State Transport University (15, Chernyshevskogo St., Irkutsk, 664074, Russian Federation), SPIN-code: [6214–3569](#), [ORCID](#), [ScopusID](#), [trucvq1990@gmail.com](#)

Об авторах:

Роман Сергеевич Большаков, кандидат технических наук, доцент кафедры управления эксплуатационной работой Иркутского государственного университета путей сообщения (664074, Российская Федерация, г. Иркутск, ул. Чернышевского, 15), SPIN-код: [2025–4049](#), [ORCID](#), [ScopusID](#), [bolshakov_rs@mail.ru](#)

Валерий Ерофеевич Гозбенко, доктор технических наук, профессор кафедры математики Иркутского государственного университета путей сообщения (664074, Российская Федерация, г. Иркутск, ул. Чернышевского, 15), SPIN-код: [4307–8922](#), [ORCID](#), [ScopusID](#), [vgozbenko@yandex.ru](#)

Выонг Куанг Чык, соискатель кафедры физики, механики и приборостроения Иркутского государственного университета путей сообщения (664074, Российская Федерация, г. Иркутск, ул. Чернышевского, 15), SPIN-код: [6214–3569](#), [ORCID](#), [ScopusID](#), [trucvq1990@gmail.com](#)

Claimed Contributorship:

RS Bolshakov: research objective formulation, building a system of equations and block diagrams, analysis of the research results, formulation of the conclusion.

EV Gozbenko: correction of the research objective, revision of the text, correction of the conclusion.

Vuong Quang Truc: calculation analysis, creation of graphic images, text analysis and addition.

Заявленный вклад авторов:

Р.С. Большаков: формирование цели исследования, построение системы уравнений и структурных схем, анализ результатов исследования, формулирование заключения.

В.Е. Гозбенко: корректировка цели исследования, доработка текста, корректировка заключения.

Выонг Куанг Чык: проведение расчетов, создание графических изображений, анализ и дополнение текста.

Conflict of Interest Statement: **the authors declare no conflict of interest.**

Конфликт интересов: **авторы заявляют об отсутствии конфликта интересов.**

All authors have read and approved the final manuscript.

Все авторы прочитали и одобрили окончательный вариант рукописи.

MECHANICS
МЕХАНИКА

Check for updates

Original Theoretical Research

Analysis of the Drag-Reduction Ability of the Layout and Cross-Sectional Shapes of Subsea Structures in the Critical Flow Mode

Henry F. Annapeh [ID], Victoria A. Kurushina [ID] ✉
Industrial University of Tyumen, Tyumen, Russian Federation
✉ v.kurushina@outlook.com

EDN: TDJYXD

Abstract

Introduction. Slender structures of subsea energy production systems are under constant influence of currents and waves. Hydrodynamic loads result from the interaction of subsea pipelines, umbilicals, equipment supports with fluid flows, and lead to the vortex formation in the area behind the structures. Vortex-induced forces are the sources of the cyclic loading. They accelerate gradually the fatigue damage, which may result in a failure. One of the ways to reduce the loads on subsea structures is to alter the shape of a cross-section, taking into account the flow regime. Dependence of the resulting hydrodynamic loads on the cross-sectional shape and relative position of structures has not been studied in details for the uniform flow in the critical mode. The current work is aimed at filling this gap. The research objective is to consider the impact of the distance between the structures, and also, the presence of a D-shaped structure, placed upstream relative to the group of three cylinders of different cross-sectional shapes.

Materials and Methods. The computational fluid dynamics approach was used in this work for numerical simulations of vortex-induced forces in the ANSYS Fluent software for cylinder with D = 0.3 m. Modelling was conducted with the Detached Eddy Simulation (DES) method, which combined advantages of the Reynolds-averaged Navier-Stokes equation (RANS) method and the Large Eddy Simulation (LES) method. The object of the research was the system of four structures in the 2D computational domain, which included the upstream D-shaped cylinder and the main group of three cylinders with the circular, squared and diamond shapes of the cross-section. The transient process was considered, where structures were under the influence of the uniform flow in the critical regime at Re = $2.5{\times}10^5$.

Results. Five sets of data were obtained in simulations for the time-dependent coefficients of the lift and drag forces: for the main system — of the D-shaped, circular, square and diamond structures, and also for the four systems — of only D-shaped, only circular, only square and only diamond shaped structures. Additional analysis was conducted for the effect of the distance between the structures on the amplitude of fluctuating hydrodynamic force coefficients. The obtained results are presented as time histories of coefficients of the lift and drag forces, frequency analysis and contours of velocity, pressure and vorticity fields. The results indicate a positive effect of the upstream D-shaped structure on reducing the drag force, acting on the central structure in the group of three cylinders located downstream.

Discussion and Conclusion. The results of the performed studies facilitate the informed decisions regarding the arrangement of subsea structures in a group of four objects, depending on the cross-sectional shape and the distance between the structures. The upstream D-shaped structure provides reducing the hydrodynamic drag force acting on the central structure in the downstream group of three structures, thereby slowing the fatigue accumulation and increasing the time of safe operation.

Keywords: vortex-induced forces, drag coefficient, lift coefficient, uniform flow

Mechanics

Оригинальное теоретическое исследование

Анализ возможности снижения лобового сопротивления за счёт расположения и поперечных сечений подводных конструкций в потоке критического режима

Г.Ф. Аннапе ![ORCID], В.А. Курушина ![ORCID] ✉

✉ v.kurushina@outlook.com

Аннотация

Введение. Длинные и узкие в поперечнике конструкции морских энергодобывающих систем находятся под постоянным воздействием течений и волн. Гидродинамические нагрузки являются результатом взаимодействия подводных трубопроводов, шлангокабелей, опор оборудования с потоком жидкости и приводят к образованию вихрей в зоне за конструкциями. Вихреобразовательные силы служат источником циклического нагружения и постепенно ускоряют усталостное разрушение, что может привести к авариям. Одним из способов снижения нагрузок на подводные конструкции является изменение формы их поперечного сечения с учетом режима потока. Недостаточно изучено, каким образом итоговые гидродинамические нагрузки зависят от формы поперечного сечения и взаимного расположения названных выше элементов систем, находящихся в равномерном критическом потоке. Представленная научная работа призвана восполнить этот пробел. Цель исследования — рассмотреть в данном контексте значение расстояния между конструкциями, а также наличие полукруглой D-образной конструкции, размещённой перед группой из трёх цилиндров с разными поперечными сечениями.

Материалы и методы. Для численного моделирования вихреобразовательных сил использовался метод вычислительной динамики флюидов в программе ANSYS Fluent для цилиндров диаметром D = 0,3 м. Моделирование выполнено методом неприсоединённых вихрей DES, который сочетает в себе преимущества метода усреднённого по Рейнольдсу уравнения Навье-Стокса RANS и метода крупных вихрей LES. В качестве объекта исследования рассматривалась система, состоящая из четырёх конструкций в вычислительном домене в 2D, включая стоящий выше по течению полукруглый цилиндр и основную группу из трёх цилиндров круглой, квадратной и ромбовидной формы поперечного сечения. Эти конструкции в условиях неустановившегося процесса находятся под действием равномерного потока критического режима при Re = $2,5 \times 10^5$.

Результаты исследования. В результате моделирования получены пять наборов данных для изменяющихся во времени коэффициентов вихреобразовательных подъёмной силы и силы сопротивления: для основной системы из полукруглой, круглой, квадратной и ромбовидной конструкции, а также для четырёх систем из только полукруглых, только круглых, только квадратных и только ромбовидных конструкций. Дополнительно проведён анализ влияния расстояния между конструкциями на амплитуду колебаний коэффициентов гидродинамических сил. Полученные результаты представлены в виде коэффициентов подъёмной силы и силы сопротивления в динамике, анализа частот и контуров полей скорости, давления, завихрённости. Результаты позволяют установить положительное влияние стоящей выше по течению полукруглой конструкции на снижение силы сопротивления на центральную конструкцию в группе из трёх цилиндров ниже по течению.

Обсуждение и заключение. Результаты проведённых исследований позволяют принимать обоснованные решения для расстановки морских конструкций в группе из четырёх объектов в зависимости от формы поперечного сечения и расстояния между ними. Установка полукруглой конструкции выше по течению позволяет снизить гидродинамическую силу сопротивления на центральную конструкцию в группе из трёх конструкций ниже по течению, что замедляет её усталостное разрушение и увеличивает срок эксплуатации.

Ключевые слова: вихреобразовательные силы, коэффициент лобового сопротивления, коэффициент подъемной силы, равномерный поток

Introduction. Operation and construction of modern offshore systems, specializing on the energy production, extraction of resources or carbon capture and storage, require evaluation of the impact of environmental flows on equipment and structures. An increased fatigue failure in subsea structures, such as pipelines, risers, cables, piles, equipment supports, may come from the vortex shedding phenomenon. The problem is particularly important when slender structures are designed to reach deep waters to connect subsystems together. The layout of subsea systems comes with the arrangement of structures with different geometry, hydrodynamic properties, and their position in proximity to each other. The interference of wakes from these structures and vortex formation patterns is sometimes challenging to predict at very high Reynolds numbers due to the turbulent nature of the flow.

Differences in the flow over a standalone cylinder and two cylinders in tandem are discussed in [1], and three vortex shedding regimes are identified for tandem structures. These vortex formation modes include the extended-body regime at $1.0 < L/D < 1.8$, where L/D is spacing ratio, commonly used to quantify the distance between centres of neighbour structures. So that, L corresponds to the distance, and D is the diameter of the structure. In [1], increase of the spacing ratio to $1.8 < L/D < 3.8$ leads to the reattachment regime, where shear layers detach from the upstream structure and reattach to the front side of the downstream structure, so that vortices are formed behind this downstream object. Further growth of the spacing ratio, above $L/D > 3.8$, introduces the co-shedding regime, where a separate vortex is formed from the upstream structure and from the downstream structure. Another fundamental research investigated vortex dynamics in details through experimental research [2]. One of the following fundamental studies [3] experimentally investigated the vortex shedding frequencies of two staggered identical circular cylinders with the Reynolds number Re varying from $3.2×10^4$ to $7.4×10^4$, and two fixed side-by-side cylinders at the Reynolds number of $2.5×10^4$ were earlier considered in [4]. These investigations provide an important foundation for modern studies in terms of the known effects in fluid forcing and vortex shedding patterns.

Significantly more recent investigations are performed numerically [5] to study the effect of spacing on loads and vibrations for two tandem cylinders at subcritical Reynolds numbers, and for specific cases, like a group of mixed large and smaller structures [6]. The latter work [6] numerically investigates fluid force coefficients and observes the vortex formation pattern on three identical rigid circular cylinders in proximity to a square cylinder. A parametric study is conducted in [7] for three identical stationary circular and D-shaped cylinders placed close to a square cylinder at Reynolds number 3900 in both linearly and parabolic sheared flows.

Considering the impact of cross-sectional shapes further, a numerical study is conducted by [8] for a flow over six identical stationary cylinders having different cross-sectional shapes at Reynolds number of $2.5×10^5$ in the uniform and linearly sheared flow. Rectangular cylinders are investigated in details in [9, 10, 11], where one of the most impactful factors for hydrodynamic loads is the aspect ratio of rectangle sides. The works [9, 10] provide new experimental data and attempt to develop semi-empirical methods of predicting the response of structures. Further steps in improving the modelling approaches for the structural vibration of rectangle-shaped objects under the hydrodynamic excitation are performed in [11]. Another branch of studies considers a flow over a sphere [12, 13, 14], while still leaving issues of the impact of the cross-sectional shape of subsea structures open.

Further research on diverse cross-sectional shapes is performed in [15, 16, 17], where triangular and diamond cross-sections are studied in comparison. Research [15] is focused on the sensitivity to the corner sharpness for the diamond (rhomb) cross-section. Work [16] investigates effects from diverse cross-sections for the system with a rotational degree of freedom, when subjected to flow-induced vibration, and study [17] uses cross-sectional shapes for the energy harvesting with fluid-structure interaction.

Following published results, the current work aims to investigate the drag reduction when three structures of different cross-sectional shapes are located around a circular cylinder to observe the wake interference and the vortex formation pattern between these structures for the spacing ratio L/D varying from 1.67 to 2.83 in the uniform flow at the Reynolds number of $2.5×10^5$ with the computational fluid dynamics approach. Specifically, the drag reducing ability of the upstream structure is of the research interest. The considered layout is a combination of cylinders placed in tandem, side-by-side and staggered position, with a mixture of cross-sectional shapes.

Materials and Methods. A system of four cylinders with a diameter (characteristic size) of 0.3 m with different cross-sectional types is considered in this study. The selected cross-sectional shapes and positions of structures are shown in Figure 1. Fluid forces and the flow interference are studied for the spacing ratio of L/D varying from 1.67 to 2.83 in the uniform current at the Reynolds number of $2.5×10^5$ and the corresponding velocity of 0.837 m/s. The study focuses on the specific layout, where structures are positioned relative to each other in a mixed tandem (cylinders 1 and 3), side-by-side (cylinders 2 and 3, and cylinders 3 and 4) and staggered (cylinders 1 and 2, and cylinders 1 and 4) configuration. Cross-sectional shapes considered include half-circle, square, circle, and diamond.

Mechanics
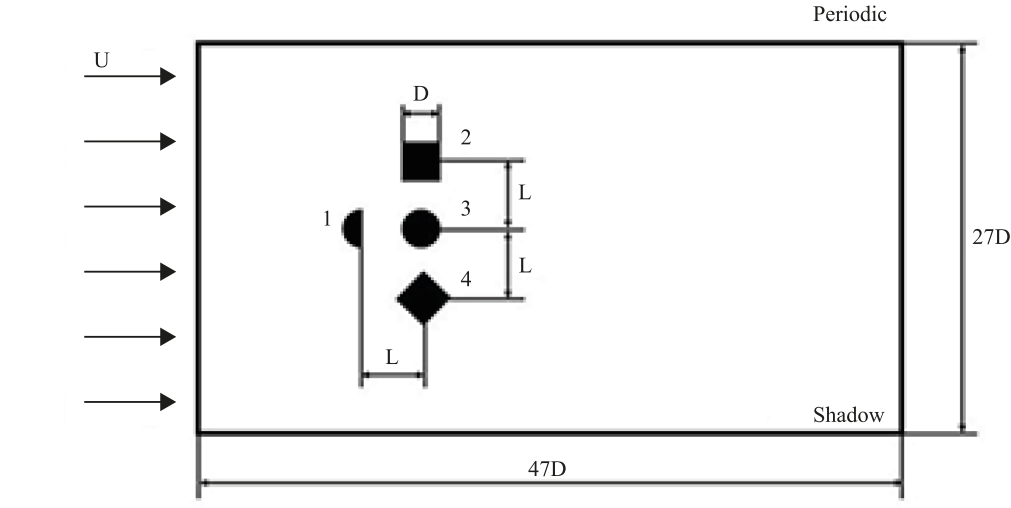
Fig. 1. Considered structures in the computational fluid domain

Computational fluid dynamic simulations are performed in the domain with a size of 47D x 27D. The top and bottom boundaries are located at a distance of 13.5D away from the center of the circular cylinder, periodic and shadow properties are assigned to these boundaries. The left boundary serves as a velocity-inlet, which is located at the distance of 20D from the centre of the circular structure 3 in the domain. The value of gauge pressure is set to zero at the pressure-outlet set at the right boundary. No-slip conditions are applied to the cylinders.

The flow around cylinders is simulated using the computational fluid dynamics software ANSYS Fluent, where the finite volume method is implemented to solve the Navier-Stokes system. The incompressible flow is considered, and the 2D DES transient simulations are conducted with the k–ω SST turbulence model. Time integration is performed using the second-order implicit transient formulation with a time step of 0.01 s, and the PISO algorithm is used as the solver.

The DES approach connects capabilities of the Reynolds-Averaged Navier-Stokes (RANS) and Large Eddy Simulation (LES) methods [8]. The RANS governing equations for the incompressible flow are as follows:

$$\frac{\partial\left(\rho\overline{u_i}\right)}{\partial x_i} = 0, \tag{1}$$

$$\frac{\partial\left(\rho\overline{u_i}\right)}{\partial t} + \frac{\partial}{\partial x_i}\left(\rho\overline{u_i u_j} + \rho\overline{u_i' u_j'}\right) = \frac{\partial\overline{\rho}}{\partial x_i} + \frac{\partial\overline{\tau_{ij}}}{\partial x_j}, \tag{2}$$

where p is mean pressure, $\overline{u_i}$ is average Cartesian components of the velocity vector, $\rho\overline{u_i' u_j'}$ are Reynolds stresses, ρ is density of the fluid, and $\overline{\tau_{ij}}$ is mean viscous stress vector components, which could be expressed as:

$$\partial\overline{\tau_{ij}} = \mu\left(\frac{\partial\overline{u_i}}{\partial x_j} + \frac{\partial\overline{u_j}}{\partial x_i}\right), \tag{3}$$

where μ is dynamic viscosity.

The Large Eddy Simulation (LES) system of equations for the incompressible flow can be written in the following way:

$$\frac{\partial\overline{u_i}}{\partial x_i} = 0, \tag{4}$$

$$\frac{\partial\overline{u_i}}{\partial t} + \frac{\partial}{\partial x_j}\left(u_i u_j\right) = -\frac{1}{\rho}\frac{\partial\overline{\rho}}{\partial x_i} + v\frac{\partial^2\overline{u_i}}{\partial x_j\partial x_j} - \frac{\partial\overline{\tau_{ij}}}{\partial x_j}, \tag{5}$$

where $\overline{u_i}$ and $\overline{\rho}$ represent the resolved filtered velocity and pressure, respectively.

The diffusion term of the DES model is given by

$$Y_k = \rho\beta^* k\omega F_{DES}, \tag{6}$$

where β^* is a constant, k stands for fluctuation of the turbulent kinetic energy, ω is specific energy dissipation rate, and F_{DES} is as follows:

$$F_{DES} = max\left(\frac{L_t}{C_{des}\Delta_{max}}, 1\right), \tag{7}$$

where C_{des} is a constant, Δ_{max} is local maximum grid map $\Delta = (\Delta_1, \Delta_2, \Delta_3)^{1/3}$. Further, L_t is turbulent length scale:

$$L_t = \frac{\sqrt{k}}{\beta^* \omega}. \tag{8}$$

The DES-SST model uses the following zonal formulation:

$$F_{DES} = max\left(\frac{L_t}{C_{des}\Delta_{max}}(1 - F_{SST}), 1 \right), \tag{9}$$

where $F_{SST} = 0$, F_1, F_2, and F_1, F_2 are mixed functions of the SST model.

Table 1 below provides results of the mesh independence test for the uniform flow of Re = 2.5×10⁵. The mesh settings are adopted from [7], and the accuracy of the grid is demonstrated by comparisons in Table 1. All subsequent analysis in this paper is performed with Mesh 2, and the results include signals and frequencies of the fluid force coefficients and an indication of the vortex shedding pattern. The drag force fluctuations are presented in this work in terms of the drag force coefficient C_D which comprises the mean drag coefficient C_{D0} and the fluctuating drag coefficient C_D^{fl}, as follows:

$$C_D = C_{D0} + C_D^{fl}. \tag{10}$$

The lift force fluctuations are presented using the lift coefficient C_L.

Table 1

Mesh independence test results

Cases	C_{D0}	Number of cells	Strouhal number
Re = 2.5×10⁵			
Current study			
Mesh 1	0.98	63,345	0.24
Mesh 2	1.08	86,478	0.24
Mesh 3	1.08	131,041	0.24
Published data			
Lehmkuhl, et al. (2014) (LES) [18]	0.833	–	0.238
Achenbach&Heinecke (1981) (Experiment) [19]	1.135	–	0.230
Re = 3,900			
Current study, Mesh 2	0.93	86,478	0.18
Wornom, et al. (2011) (VMS-LES) [20]	0.99	–	–
Re = 3.6×10⁶			
Current study, Mesh 2	0.4100	86,478	–
Porteous, et al. (2015) (URANS) [21]	0.4206	–	–
Nazvanova, et al. (2022) (URANS) [22]	0.4657	74,496	–

Results. In this study, simulations are performed in two series. The first series is focused on recognising the overall effect of various cross-sectional shapes, placed at $L/D = 2.00$ from each other. Cylinder numbers here correspond to the ones used in Figure 1, according to the cylinders position. The calculation results for this set are reported in Table 2, in comparison to the case of structures with mixed cross-sections. The second series provides an insight into the impact of L/D ratio on hydrodynamic loads observed for the mixed cross-section case only, as in Figure 1. These results are summarised in Table 3 and allow defining the drag reducing effect of the D-shape upstream structure on loads when cross-sections are different.

Mechanics

Table 2

Simulation results for the same arrangement with different cross-sectional shapes for $L/D = 2.00$

$L/D = 2.0$	Basic case of structures with alternate cross-sections in Fig. 1	All circular structures	All square structures	All D-shaped structures	All diamond-shaped structures
Cylinder 1					
C_{D0}	0.45	0.28	0.49	0.48	0.46
C_D^{fl}	0.19	0.14	0.43	0.28	0.17
C_L	0.18	0.04	0.07	0.13	0.28
Cylinder 2					
C_{D0}	0.87	0.39	0.89	0.64	0.70
C_D^{fl}	1.03	0.38	1.38	0.49	0.60
C_L	1.38	0.53	0.07	0.11	0.07
Cylinder 3					
C_{D0}	0.3	0.24	0.26	0.35	0.70
C_D^{fl}	0.45	0.37	0.91	0.68	0.63
C_L	1.03	0.73	1.26	0.30	0.73
Cylinder 4					
C_{D0}	0.98	0.39	0.83	0.61	0.99
C_D^{fl}	0.90	0.27	0.96	0.44	1.05
C_L	1.22	0.81	1.63	0.37	1.11

Table 3

Simulation results for the mixed cross-sections at various L/D ratio

L/D	Cylinder 1			Cylinder 2			Cylinder 3			Cylinder 4		
	C_{D0}	C_D^{fl}	C_L	C_{D0}	C_D^{fl}	C_L	C_{D0}	C_D^{fl}	C_L	C_{D0}	C_D^{fl}	C_L
1.67	0.14	0.18	0.15	0.98	1.17	1.44	0.48	0.57	0.66	0.93	0.75	1.13
1.83	0.33	0.21	0.18	0.93	1.54	1.40	0.33	0.50	0.86	1.01	1.36	1.15
2.00	0.45	0.19	0.18	0.87	1.03	1.38	0.30	0.45	1.03	0.98	0.90	1.22
2.17	0.49	0.05	0.19	0.81	0.14	1.11	0.25	0.06	0.83	0.96	0.38	1.10
2.33	0.37	0.12	0.00	0.78	0.34	1.03	0.25	0.06	0.28	1.00	0.07	0.79
2.50	0.57	0.16	0.20	0.76	0.89	1.18	0.26	0.47	0.77	1.01	0.64	1.06
2.67	0.57	0.02	0.27	0.78	0.16	1.37	0.28	0.08	0.82	1.02	0.03	0.96
2.83	0.58	0.21	0.21	0.84	0.91	1.70	0.20	0.52	1.16	0.93	0.68	1.03

Comparison of all circular, all square, mixed (as in Fig. 1), all diamond and all D-shapes with each other in Table 2 reveals relatively lower hydrodynamic loads for all four structures observed for the circular shapes at the $L/D = 2.00$. The largest mean drag coefficient here is experienced by the fourth structure in both mixed-shaped and all diamond-shaped arrangement. The highest maximum fluctuating drag coefficient of 1.38 is observed for cylinder 2 in the all square-shaped arrangement. The largest maximum amplitude of the lift coefficient of 1.63 also belongs to the all square-shaped arrangement, but corresponds to cylinder 4. Mixed-shaped arrangement (or basic case of structures with alternate cross-sections, as in Fig. 1) at $L/D = 2.00$ demonstrates a relative consistency in large amplitudes of the lift coefficient for cylinders 2, 3, 4, which makes estimations of hydrodynamic loads for this arrangement more important, due to higher expected loads.
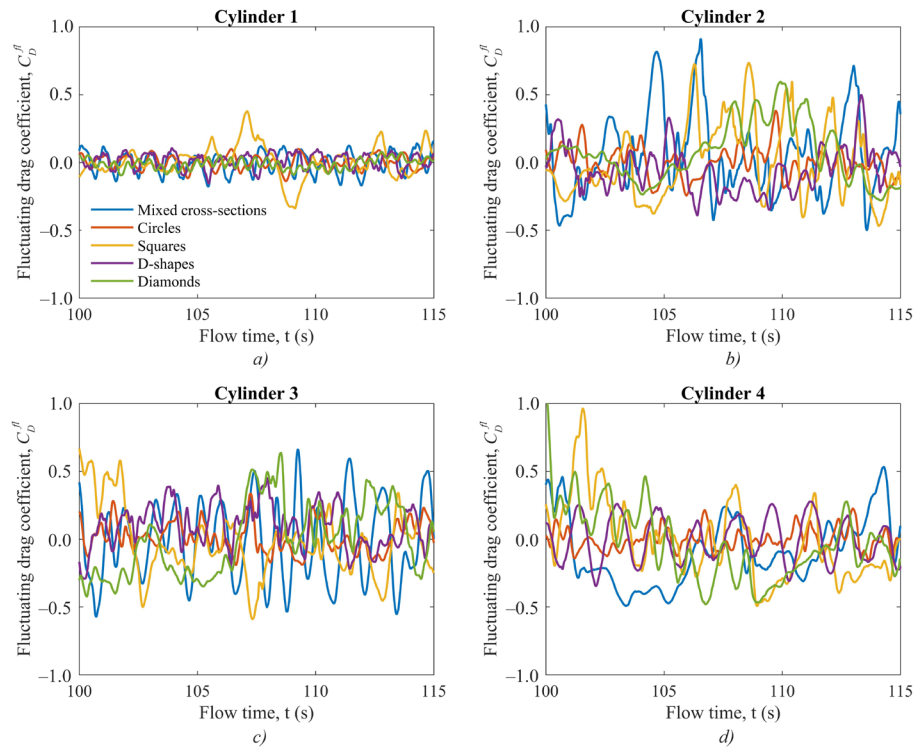
Fig. 2. Time histories of fluctuating drag coefficients for four cylinders of a different cross-sectional shape with *L/D* = 2.0:
a — cylinder 1; *b* — cylinder 2; *c* — cylinder 3; *d* — cylinder 4
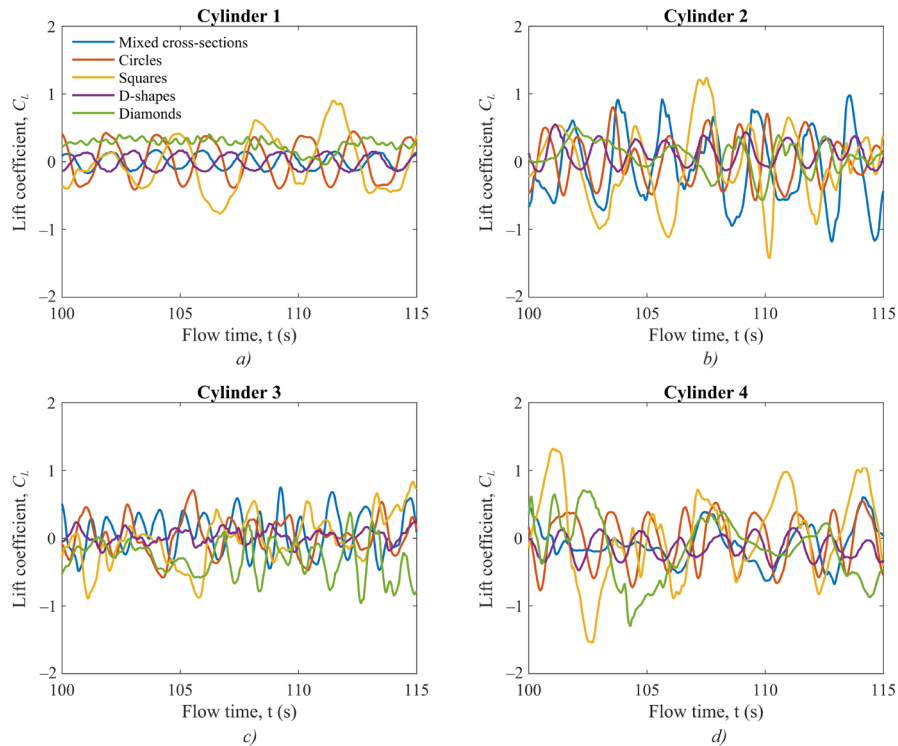
Fig. 3. Time histories of lift coefficients for four cylinders of a different cross-sectional shape with *L/D* = 2.0:
a — cylinder 1; *b* — cylinder 2; *c* — cylinder 3; *d* — cylinder 4

Further observation of signals of the fluctuating drag and lift coefficient in Figures 2 and 3 reveals meaningful instabilities in forces experienced by all structures with square shapes, and for structures 2, 3, 4 with diamond and mixed shapes. The comparison shows that circular and D-shaped structures would experience lower and more stable fluid loads in this arrangement. Table 2 and Figures 2 and 3 confirm that cylinder 1 in the shape of a circle or D-shape provides reducing fluid loads for the three downstream cylinders. This substantiates the common interest in further exploration of the effect of the D-shaped structure on reducing the drag force in the arrangement with all alternative cross-sectional shapes.

Mechanics

141

This effect is studied in details in the next (second) simulation series, presented for each cylinder in Figures 4–7 in terms of the fluid forces and in Figures 8, 9 — in terms of the fluid flow characteristics for the considered computational domain. Figure 4 illustrates fluid loads on the upstream structure, where the most unstable signal (at $L/D = 2.17$) belongs to fluctuations of the drag force. Figure 4 *c* also indicates presence of multiple frequencies in signals of the fluctuating drag coefficient, while a single dominating frequency can be identified for the lift force coefficient in Figure 4 *d*. Figures 4 *c* and 4 *d* demonstrate that the frequency of both lift and drag forces generally increases with the growing L/D ratio, and the maximum frequency is indicated by signals at $L/D = 2.67$ and 2.83.
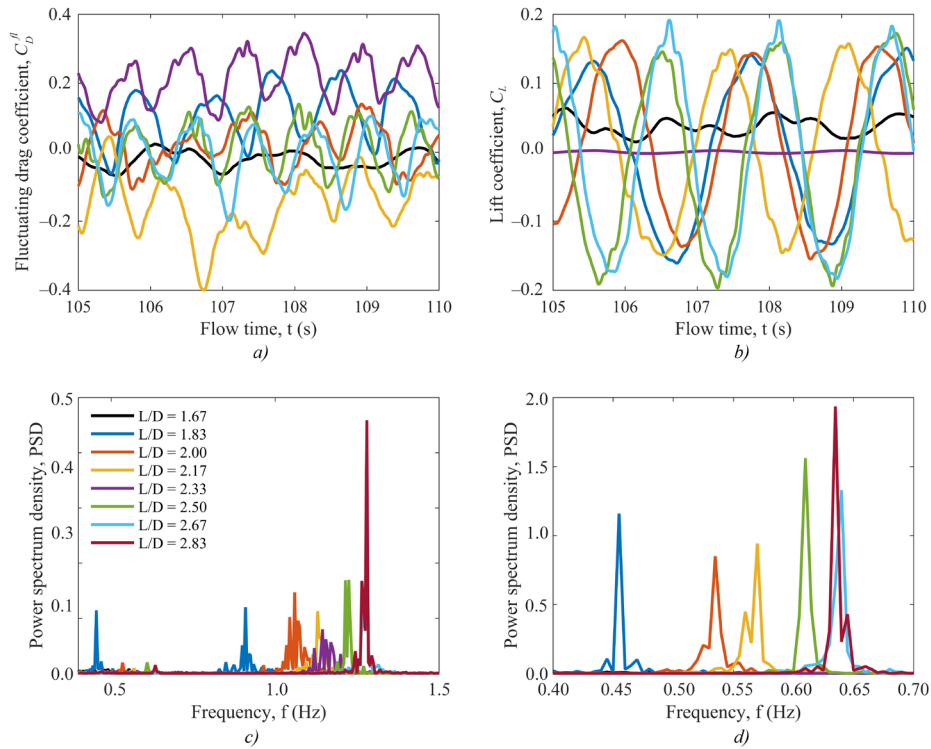
Fig. 4. Time histories of fluid force coefficients for cylinder 1 in the uniform flow:
a — fluctuating drag coefficient; *b* — lift coefficient; *c* — fluctuating drag coefficient FFT; *d* — lift coefficient FFT

Relatively similar complexity of frequencies of the lift force is observed in Figure 6 *d* for cylinder 3, where one to two dominant frequencies could be clearly identified. At the same time, more than two frequencies are observed in Figure 6 *c* for each signal of the fluctuating drag force. The pattern of growth in the overall dominant frequency with the increasing L/D is still recognisable for cylinder 3, similar to cylinder 1. Combination of frequencies is even more complex for cylinders 2 and 4, as comes from Figures 5 *c–d* and 7 *c–d*, this is not possible to indicate clear dependences in the frequencies of the fluctuating drag force. Some resemblance of the found growth trend could be still observed in Figure 5 *d* for the lift force coefficient for cylinder 2. This provides evidence for the generally unstable nature of hydrodynamic loads acting on the square cross-section shown in Figure 5.

Impact of the L/D ratio on the mean drag coefficient for cylinder 1, based on Table 3, is partially confirmed: apart from a couple of deviations, the mean drag force increases with the growth of L/D. Data for cylinders 2 and 4 do not indicate a specific pattern, as the values fluctuate back and forth within 10% from the initial mean drag coefficient at the smallest L/D. Cylinder 3, on the contrary, indicates a stable pattern of the reduced mean drag coefficient with the increased L/D, so that the reducing ability of the upstream D-shaped structure is evident, but for the central cylinder only. The largest mean drag coefficient of 1.02 is linked to cylinder 4 at $L/D = 2.67$. The considered range of L/D allows observing an important transition from the strong to minor interference in the wake of the three paired structures.

The highest fluctuating drag coefficients of 1.54 and 1.36 are linked to cylinders 2 and 4, respectively, both observed at $L/D = 1.83$. The feature of the maximum amplitude of the fluctuating drag coefficient, indicated in Table 2, is in absence of a specific dependence from the L/D, the values rapidly change from near zero to relatively high with a small increment of change in the ratio. The fluctuating drag coefficient has generally the lowest amplitudes for cylinder 1, average amplitudes — for cylinder 3, and the largest amplitudes — for cylinders 2 and 4.

The largest maximum amplitude of the lift coefficient occurs at $L/D = 2.83$ for cylinder 2. The lift coefficient generally resembles the distribution, similar to the maximum amplitude found for the fluctuating drag coefficient: the lift force appears to be the smallest for cylinder 1, relatively intermediate — for cylinder 3, and the highest — for cylinders 2 and 4, with no specific pattern linked to the L/D increase and reduction. This allows us to conclude that the ability to

reduce hydrodynamic forces by placing the upstream D-shaped structure in front of the array is limited. The force reduction is observed mainly for the structure placed in tandem downstream, and the effect is most pronounced for the mean drag coefficient, with some reduced effects also seen for the fluctuating drag and lift coefficients.
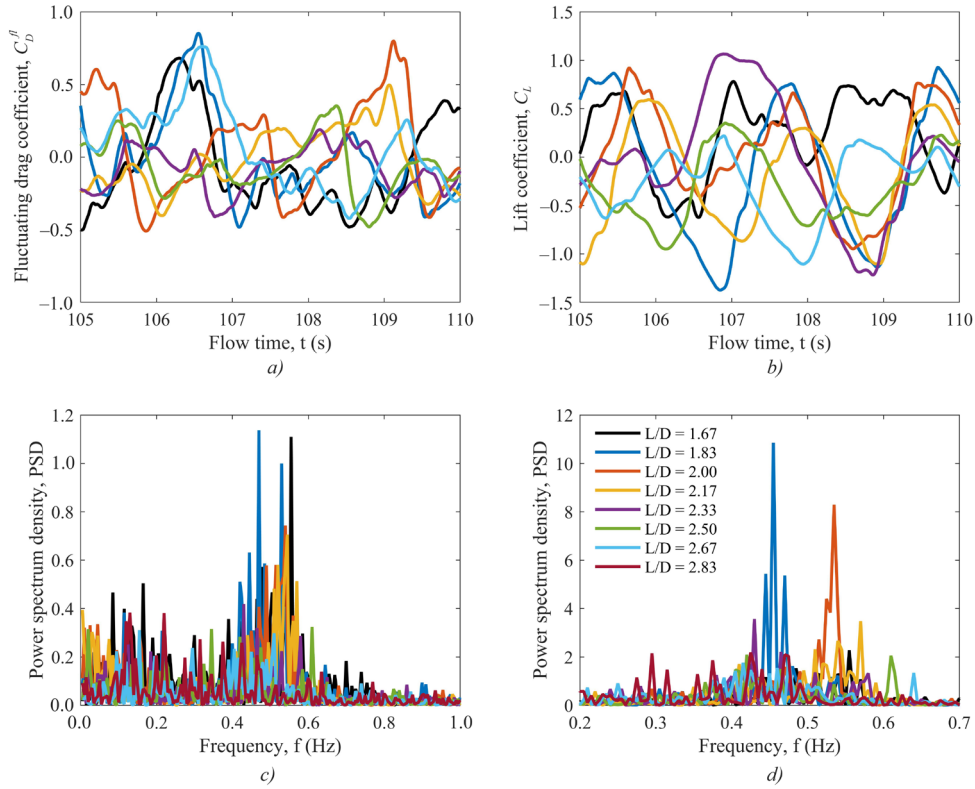
Fig. 5. Time histories of fluid force coefficients for cylinder 2 in the uniform flow:
a — fluctuating drag coefficient; *b* — lift coefficient; *c* — fluctuating drag coefficient FFT; *d* — lift coefficient FFT
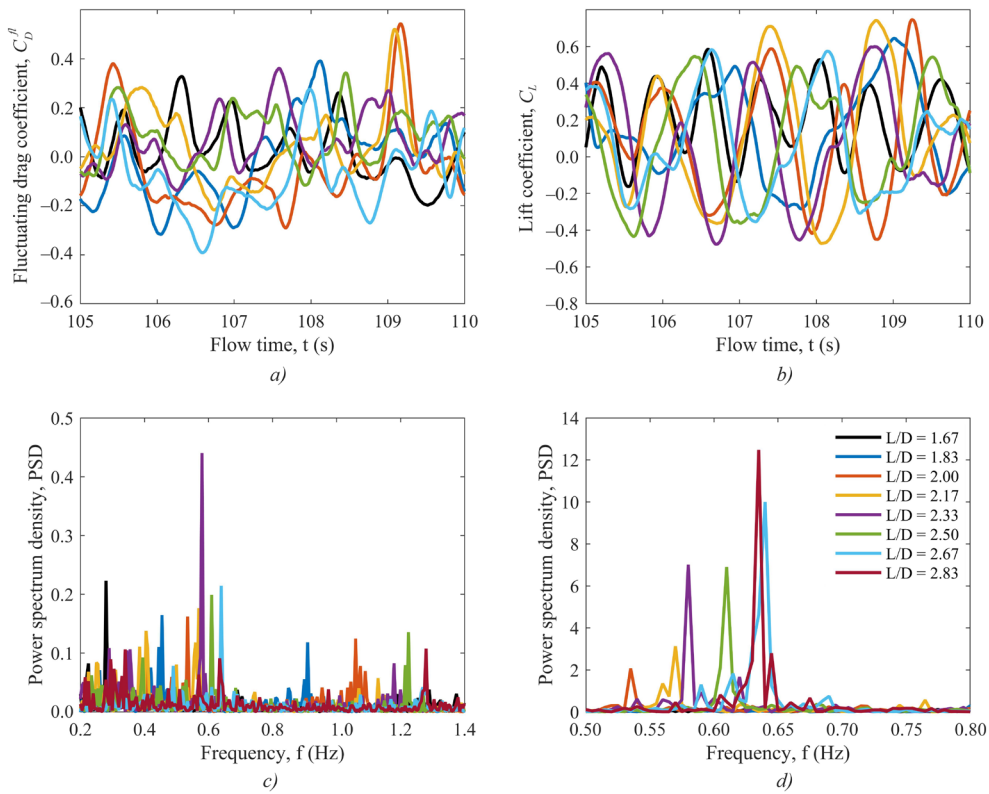
Fig. 6. Time histories of fluid force coefficients for cylinder 3 in the uniform flow:
a — fluctuating drag coefficient; *b* — lift coefficient; *c* — fluctuating drag coefficient FFT; *d* — lift coefficient FF

Mechanics
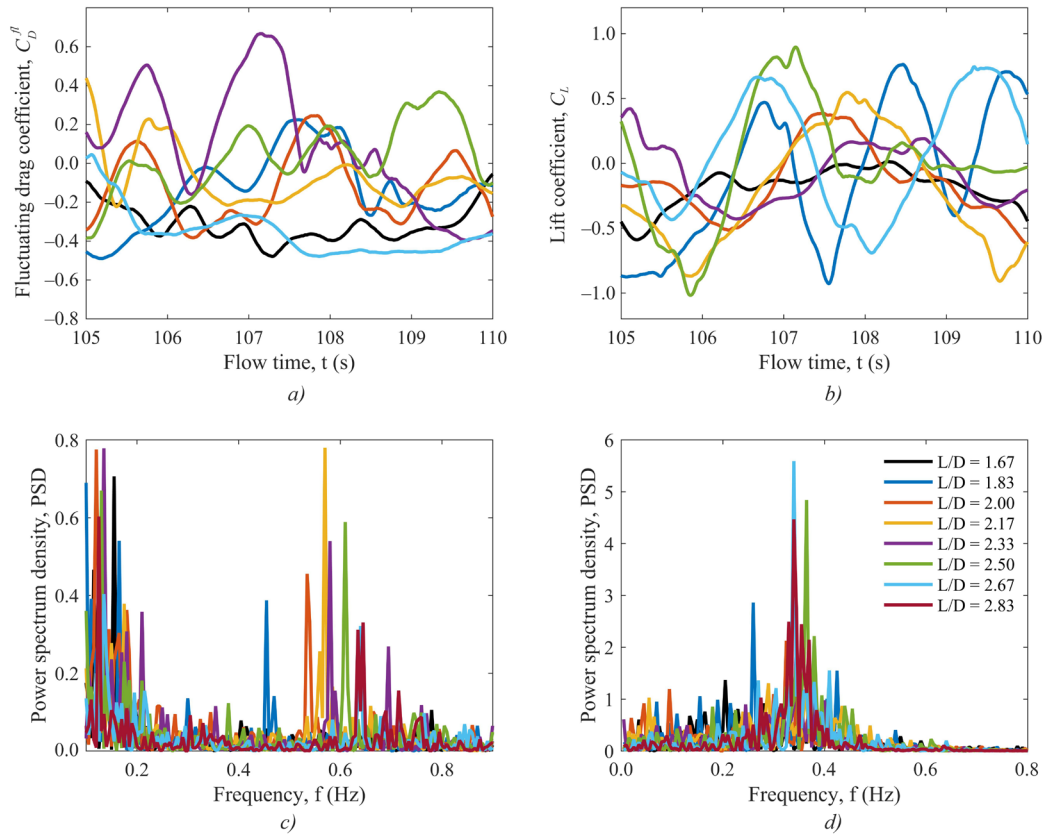
Fig. 7. Time histories of fluid force coefficients for cylinder 4 in the uniform flow:
a — fluctuating drag coefficient; *b* — lift coefficient; *c* — fluctuating drag coefficient FFT; *d* — lift coefficient FFT
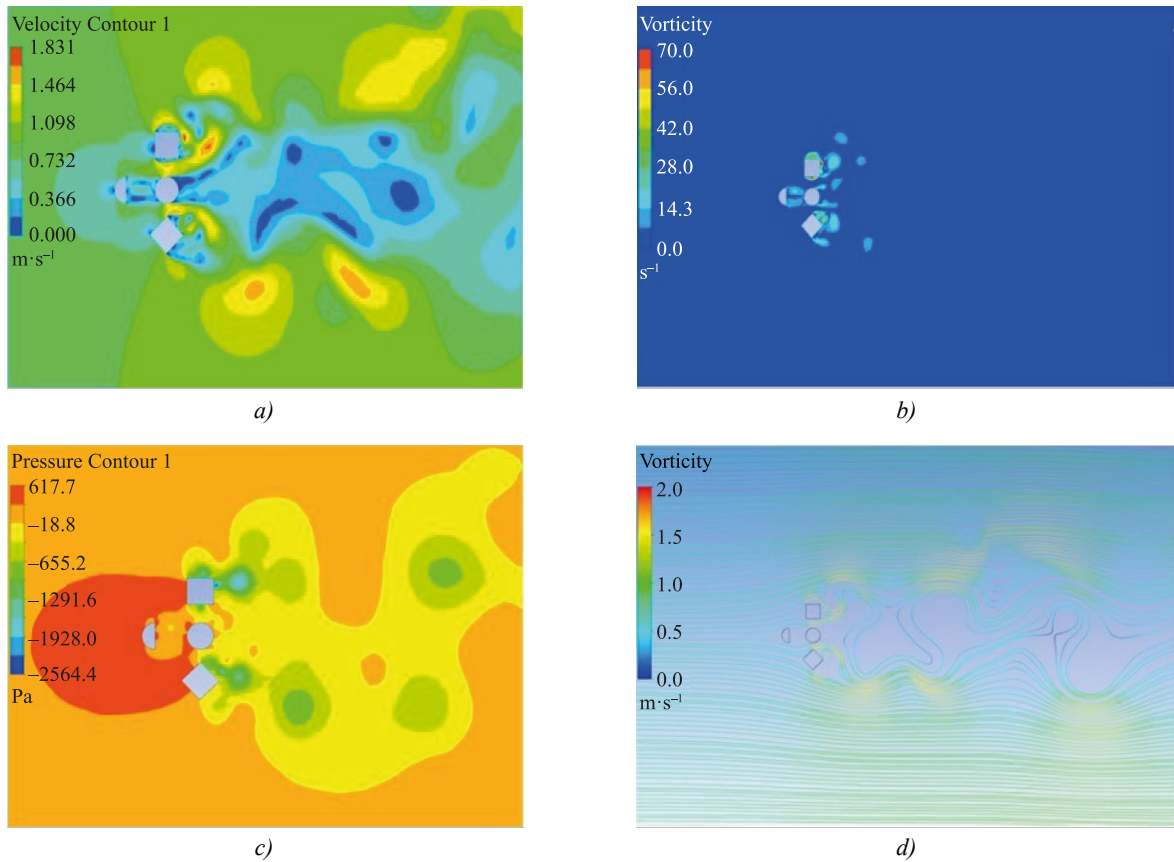
Fig. 8. Contours of the flow characteristics for *L/D* = 1.67 at 200 seconds:
a — velocity contour; *b* — vorticity contour; *c* — pressure contour; *d* — streamline
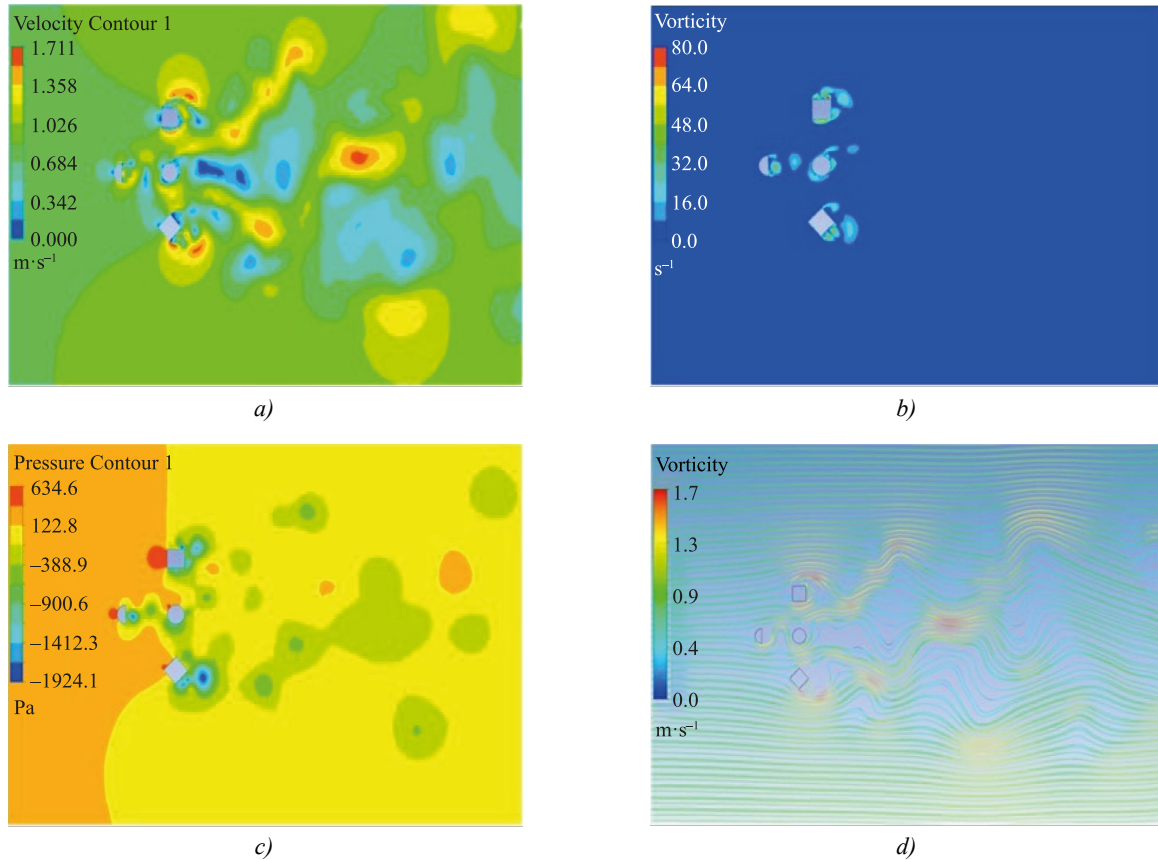
Fig. 9. Contours of the flow characteristics for *L/D* = 2.83 at 200 seconds:
a — velocity contour; *b* — vorticity contour; *c* — pressure contour; *d* — streamline

Figures 8–9 show the velocity, vorticity, pressure and streamlines of the flow around cylinders for some selected *L/D*, where both proximity and wake interference among the cylinders are presented for the time step of 200 s. The flow around cylinders is complex, and vortex formation patterns are highly affected, as the distance between the cylinders increases. The proximity interference is observed for cylinders 2, 3, and 4, alternate single vortices are shed on the downstream side of these structures. For the wake interference at *L/D* = 1.67, free shear layers separate from the upstream cylinder 1 and reattach themselves to the upstream side of cylinder 3, and a vortex street is only formed at the downstream side of cylinder 3. At this distance, a broad region of wake is created at the downstream side of cylinders 2, 3, and 4. As the *L/D* increases above 2.00, there are vortices formed at the upstream side of cylinder 3, in the wake of cylinder 1. A vortex street is also formed at the downstream side of cylinder 3, with formation of 2S vortices. Figures 8 *a*, 9 *c* demonstrate a group of minor vortices formed following the diamond-shaped cylinder 4 and a vortex pair formed in a similar to S+P vortex cycle past cylinder 2.

Discussion and Conclusion. The 2D numerical simulations are performed in this work for cylinders with different cross-sectional shapes at the Reynolds number of 2.5×10^5 using the DES approach. The considered cylinders are studied in a complex position of an upstream D-shaped structure in front of three paired structures, with the aim to investigate the drag-reducing ability of this specific layout, observe the flow complexity, the wake interference from each structure, and vortex formation patterns.

The following conclusions could be made from this study:

1. The ability to reduce hydrodynamic forces by placing the upstream D-shaped structure is mainly limited to the structure placed in tandem downstream, and the effect is most pronounced for the mean drag coefficient.

2. Overall, the mean drag coefficient of cylinders is observed to be affected by varying *L/D*, with the main effect on the mean drag coefficient of cylinder 1, which grows with increasing *L/D*, and of cylinder 3, which reduces with increasing *L/D*.

3. Competition of frequencies is observed for the fluctuating drag coefficient for all structures and lift coefficient signal of cylinders 2 and 4. This competition is due to the joint effects of both the uniform current and wake interference, which intensifies at a lower *L/D* in terms of changes to the resulting vortex street.

4. Both proximity and wake interference among the cylinders are observed. The flow around cylinders is complex, and vortex formation patterns are highly affected as the distance between the cylinders increased with 2S being the major vortex type formed and shedding the additional vortices from the square and diamond structures.

Mechanics

The study generally contributes to the field of knowledge by advancing our understanding of fluid-structure interactions, drag reduction strategies, and vortex dynamics, with potential applications in offshore energy systems. The current work contributes to the development of the drag reduction strategies through analyzing the impact of the upstream D-shaped structure on downstream cylinders. Understanding how different structural configurations affect drag can inform the design of more efficient systems in various engineering applications, such as subsea transportation of fluids. By observing flow complexity, wake interference, and vortex formation patterns, this study contributes to the understanding of fluid dynamics around complex geometries. This knowledge is crucial for optimizing the performance of structures in environments where fluid flow plays a significant role, such as subsea engineering. The results of the present research highlight the effect of varying the aspect ratio L/D on drag coefficients to inform engineering designs of similar arrangements. This study reveals the intricate vortex dynamics and shedding patterns, particularly concerning the proximity and wake interference among cylinders. Understanding these phenomena can aid in predicting and controlling flow behavior around complex configurations, leading to more efficient designs and better performance in practical applications in offshore systems.

References

1. Zdravkovich MM. Review of Flow Interference between Two Circular Cylinders in Various Arrangements. *Journal of Fluids Engineering.* 1977;99(4):618–633. https://doi.org/10.1115/1.3448871

2. Williamson CHK. Vortex Dynamics in the Cylinder Wake. *Annual Review of Fluid Mechanics.* 1996;28(1):477–539. https://doi.org/10.1146/annurev.fl.28.010196.002401

3. Wanhai Xu, Haokai Wu, Kun Jia, Enhao Wang. Numerical Investigation into the Effect of Spacing on the Flow-Induced Vibrations of Two Tandem Circular Cylinders at Subcritical Reynolds Numbers. *Ocean Engineering.* 2021;236:109521. https://doi.org/10.1016/j.oceaneng.2021.109521

4. Sumner D, Richards MD, Akosile OO. Two Staggered Circular Cylinders of Equal Diameter in Cross-Flow. *Journal of Fluids and Structures.* 2005;20(2):255–276. https://doi.org/10.1016/j.jfluidstructs.2004.10.006

5. Bearman PW, Wadcock AJ. The Interaction between a Pair of Circular Cylinders Normal to a Stream. *Journal of Fluid Mechanics.* 1973;61(3):499–511. https://doi.org/10.1017/S0022112073000832

6. Annapeh HF, Kurushina V. Numerical Simulation of Flow-Induced Forces on Subsea Structures in a Group Under Uniform and Sheared Flow. In book: Dimitrovová Z, Biswas P, Gonçalves R, Silva T. (eds). *Recent Trends in Wave Mechanics and Vibrations.* Cham: Springer; 2022. P. 512–522. https://doi.org/10.1007/978-3-031-15758-5_52

7. Annapeh HF, Kurushina V. Flow-Induced Forces for a Group of One Large and Several Small Structures in the Sheared Turbulent Flow. *Fluids.* 2023;8(5):158. https://doi.org/10.3390/fluids8050158

8. Annapeh HF, Kurushina V. Hydrodynamic Loads on a Group of Six Structures of Different Cross-Sections in Uniform and Sheared Flow. *Journal of Marine Science and Engineering.* 2023;11(2):383. https://doi.org/10.3390/jmse11020383

9. Mannini C, Marra AM, Massai T, Bartoli G. Interference of Vortex-Induced Vibration and Transverse Galloping for a Rectangular Cylinder. *Journal of Fluids and Structures.* 2016;66:403–423. https://doi.org/10.1016/j.jfluidstructs.2016.08.002

10. Marra AM, Mannini C, Bartoli G. Measurements and Improved Model of Vortex-Induced Vibration for an Elongated Rectangular Cylinder. *Journal of Wind Engineering and Industrial Aerodynamics.* 2015;147:358–367. https://doi.org/10.1016/j.jweia.2015.08.007

11. Bin Liu, Renjie Jiang. Vortex-Induced Vibrations of a Rectangular Cylinder. *Ocean Engineering.* 2022;266:112883. https://doi.org/10.1016/j.oceaneng.2022.112883

12. Jauvtis N, Govardhan R, Williamson CHK. Multiple Modes of Vortex-Induced Vibration of a Sphere. *Journal of Fluids and Structures.* 2001;15(3–4):555–563. https://doi.org/10.1006/jfls.2000.0348

13. Govardhan RN, Williamson CHK. Vortex-Induced Vibrations of a Sphere. *Journal of Fluid Mechanics.* 2005;531:11–47. https://doi.org/10.1017/S0022112005003757

14. Gabyshev DN, Szakáll M, Shcherbakov DV, Fedorets AA, Dyachkov SM. Oscillatory Signatures in the Raindrop Motion Relative to the Air Medium with Terminal Velocity. *Atmosphere.* 2022;13(7):1137. https://doi.org/10.3390/atmos13071137

15. Leontini JS, Thompson MC. Vortex-Induced Vibrations of a Diamond Cross-Section: Sensitivity to Corner Sharpness. *Journal of Fluids and Structures.* 2013;39:371–390. https://doi.org/10.1016/j.jfluidstructs.2013.01.002

16. Arionfard H, Mohammadi S. Numerical Investigation of the Geometrical Effect on Flow-Induced Vibration Performance of Pivoted Bodies. *Energies.* 2021;14(4):1128. https://doi.org/10.3390/en14041128

17. Mehdipour I, Madaro F, Rizzi F, De Vittorio M. Comprehensive Experimental Study on Bluff Body Shapes for Vortex-Induced Vibration Piezoelectric Energy Harvesting Mechanisms. *Energy Conversion and Management: X.* 2022;13:100174. https://doi.org/10.1016/j.ecmx.2021.100174

18. Lehmkuhl O, Rodríguez I, Borrell R, Chiva J, Oliva A. Unsteady Forces on a Circular Cylinder at Critical Reynolds Numbers. *Physics of Fluids.* 2014;26(12):125110. https://doi.org/10.1063/1.4904415

19. Achenbach E, Heinecke E. On Vortex Shedding from Smooth and Rough Cylinders in the Range of Reynolds Numbers 6×10^3 to 5×10^6. *Journal of Fluid Mechanics*. 2006;109:239–251. https://doi.org/10.1017/S002211208100102X

20. Wornom S, Ouvrard H, Salvetti MV, Koobus B, Dervieux A. Variational Multiscale Large-Eddy Simulations of the Flow past a Circular Cylinder: Reynolds Number Effects. *Computers & Fluids*. 2011;47(1):44–50. https://doi.org/10.1016/j.compfluid.2011.02.011

21. Porteous A, Habbit R, Colmenares J, Poroseva S, Murman SM. Simulations of Incompressible Separated Turbulent Flows around Two-Dimensional Bodies with URANS Models in OpenFOAM. In: *Proc. 22nd AIAA Computational Fluid Dynamics Conference.* Reston, VA: AIAA; 2015. P. 2609. https://doi.org/10.2514/6.2015-2609

22. Nazvanova A, Guang Yin, Muk Chen Ong. Numerical Investigation of Flow around Two Tandem Cylinders in the Upper Transition Reynolds Number Regime Using Modal Analysis. *Journal of Marine Science and Engineering*. 2022;10(10):1501. https://doi.org/10.3390/jmse10101501

About the Authors:

Henry Francis Annapeh, Research Assistant, Laboratory of Vibration and Hydrodynamics Modelling, Industrial University of Tyumen (38, Volodarskogo Str., Tyumen, 625000, Russian Federation), ORCID, ScopusID, kinghenry939@gmail.com

Victoria A. Kurushina, Head of the Laboratory of Vibration and Hydrodynamics Modelling, Industrial University of Tyumen (38, Volodarskogo Str., Tyumen, 625000, Russian Federation), SPIN-code: 7681–7930, ORCID, ScopusID, ResearcherID, v.kurushina@outlook.com

Об авторах:

Генри Франсис Аннапе, лаборант лаборатории вибрационного и гидродинамического моделирования Тюменского индустриального университета (625000, Российская Федерация, г. Тюмень, ул. Володарского, 38), ORCID, ScopusID, kinghenry939@gmail.com

Виктория Александровна Курушина, заведующий лаборатории вибрационного и гидродинамического моделирования Тюменского индустриального университета (625000, Российская Федерация, г. Тюмень, ул. Володарского, 38), SPIN-код: 7681–7930, ORCID, ScopusID, ResearcherID, v.kurushina@outlook.com

Claimed Contributorship:

HF Annapeh: conceptualization, literature review, methodology, investigation, computation, processing the results, original draft preparation, editing.

VA Kurushina: methodology, research management, investigation, computation, processing the results, financial backing, review and editing.

Заявленный вклад авторов:

Г.Ф. Аннапе: концептуализация, обзор литературы, методология, исследование, расчёты, обработка результатов, подготовка первого черновика статьи, редактирование.

В.А. Курушина: методология, руководство исследованием, расчёты, обработка результатов, финансирование, редактирование статьи.

Conflict of Interest Statement: **the authors declare no conflict of interest.**

Конфликт интересов: **авторы заявляют об отсутствии конфликта интересов.**

All authors have read and approved the final manuscript.

Все авторы прочитали и одобрили окончательный вариант рукописи.

Mechanics

MECHANICS
МЕХАНИКА

Check for updates

Original Theoretical Research

On a Method for Calculating Bending and Shear Vibrations of a Porous Piezoelement in the Low-Frequency Region

Arkadiy N. Soloviev[1,2,3] (ID) ✉, **Valery A. Chebanenko**[2,3,4] (ID), **Pavel A. Oganesyan** [2] (ID),

Elizaveta I. Fomenko[2] (ID)

[1] Crimean Engineering and Pedagogical University named after Fevzi Yakubov, Simferopol, Republic of Crime

[2] Southern Federal University, Rostov-on-Don, Russian Federation

[3] Don State Technical University, Rostov-on-Don, Russian Federation

[4] Southern Research Center, Russian Academy of Sciences, Rostov-on-Don, Russian Federation

✉ solovievarc@gmail.com

EDN: VPUERG

Abstract

Introduction. Devices for collecting and storing energy from the external environment are low-power sources of electric energy that are actively used. The autonomous devices for monitoring the damaged condition of various structures include them as well. The working element of these devices is a piezoelectric generator (PEG) — a converter of mechanical energy into electrical energy. The design of PEG is associated with the preliminary construction of their mathematical and computer models, with the help of which the calculation and optimization of structures is carried out. One of the ways to model and calculate PEG is to develop approximate calculation methods based on applied theories. The applied theories for calculating bending vibrations of multilayer piezoactive plates are known and previously developed in the literature. However, in the scientific literature there is not enough information about bending and shear vibrations as a tool for improving the efficiency of engineering calculations of the described structures. The objective of this work was to develop an applied method for calculating bending and shear vibrations of piezoceramic plates, including porous ones.

Materials and Methods. Piezoceramics PZT-4, including porous ones, were used as the piezoactive material of the plate. When using porous ceramics, the rigidity of the structure decreased to a greater extent than the piezoelectric modules, which made it possible to obtain a more effective PEG under mechanical action. The mathematical formulation was carried out within the framework of the linear theory of electroelasticity with plate polarization in thickness. The sides of the plate were electrodated, the right side was fixed, and a smooth contact in the vertical wall was set on the left side. Steady-state vibrations of the plate were caused by pressure on the front surfaces of the plate or the difference in electrical potentials at the electrodes. To calculate the characteristics of PEG, the authors proposed an applied theory based on hypotheses about the distribution of characteristics of the stress-strain state and the electric field.

Results. Transverse vibrations of a piezoceramic plate in the low-frequency region (below the first bending-shear resonance) were studied. Due to the fact that the mathematical formulation was considered within the framework of the linear theory of elasticity, the problem was divided into the sum of two. The first one took into account the mechanical effect: a distributed load and a transverse force at the left end acted on the front surfaces of the plate, and the potentials at the electrodes were zero. In the second task, there were no mechanical loads, but the potential difference was set at the electrodes. Based on hypotheses about the distribution of deformations, mechanical stresses and electric potential, both problems were reduced to a system of ordinary differential equations and boundary conditions. Comparison with the results of calculations by the finite element method in the ACELAN package showed the adequacy of the proposed applied theory in the low-frequency region.

Discussion and Conclusion. Since the formulation of the problem was considered in the linear theory of electroelasticity, and the low-frequency region was studied, the work succeeded in dividing the problem of bending-shear vibrations of a porous piezoceramic plate into two: bending — with mechanical action at zero potentials, and shear — when setting the potential difference and zero mechanical action. The corresponding hypotheses about bending and shear were used. Two systems of ordinary differential equations and boundary conditions, which were solved analytically without the use

of "heavy" finite element packages, were constructed. To compare the results and confirm the adequacy of the proposed method, the finite element modeling of such tasks was carried out in a specialized ACELAN package. The comparison showed that the error in determining displacements and electric potential when using this approach, in the case of setting mechanical loads and potential differences, did not exceed 6%. The method developed in the paper can be applied in the design of piezoelectric generators for energy storage in the low-frequency region.

Оригинальное теоретическое исследование

Об одном методе расчета изгибных и сдвиговых колебаний пористого пьезоэлемента в низкочастотной области

А.Н. Соловьев [1,2,3] iD ✉**, В.А. Чебаненко**[2,3,4] iD**, П.А. Оганесян**[2] iD**, Е.И. Фоменко**[2] iD

[1] Крымский инженерно-педагогический университет имени Февзи Якубова, г. Симферополь, Республика Крым, Российская Федерация

[2] Южный Федеральный Университет, г. Ростов-на-Дону, Российская Федерация

[3] Донской государственный технический университет, г. Ростов-на-Дону, Российская Федерация

[4] Южный Научный центр РАН, г. Ростов-на-Дону, Российская Федерация

✉ solovievarc@gmail.com

Аннотация

Введение. Устройства сбора и накопления энергии из внешней среды представляют собой маломощные источники электрической энергии, которые активно используются, в том числе в автономных приборах мониторинга поврежденного состояния различных конструкций. Рабочим элементом этих устройств является пьезоэлектрический генератор (ПЭГ) — преобразователь механической энергии в электрическую. Конструирование ПЭГ связано с предварительным построением их математических и компьютерных моделей, с помощью которых производится расчет и оптимизация конструкций. Одним из способов моделирования и расчета ПЭГ является разработка приближенных методов расчета на основе прикладных теорий. В литературе известны и ранее разработаны прикладные теории расчета изгибных колебаний многослойных пьезоактивных пластин. Однако информации об изгибно-сдвиговых колебаниях, как инструменте повышения эффективности инженерных расчетов описанных конструкций, в научной литературе недостаточно. Целью настоящей работы являлась разработка прикладного метода расчета изгибных и сдвиговых колебаний пьезокерамических пластин, в том числе пористых.

Материалы и методы. В качестве пьезоактивного материала пластины используется пьезокерамика PZT-4, в том числе пористая. При использовании пористой керамики жесткость конструкции уменьшается в большей степени, чем пьезомодули, что позволяет получить более эффективный ПЭГ при механическом воздействии. Математическая постановка осуществлена в рамках линейной теории электроупругости при поляризации пластины по толщине. Боковые стороны пластины электродированы, правая сторона закреплена, а на левой задан гладкий контакт в вертикальной стенке. Установившиеся колебания пластины вызываются давлением на лицевые поверхности пластины или разностью электрических потенциалов на электродах. Для расчета характеристик ПЭГ в работе предлагается прикладная теория, основанная на гипотезах о распределении характеристик напряженно-деформированного состояния и электрического поля.

Результаты исследования. Рассмотрены поперечные колебания пьезокерамической пластины в низкочастотной области (ниже первого изгибно-сдвигового резонанса). В силу того, что математическая постановка рассмотрена в рамках линейной теории упругости, задача разделилась на сумму двух. В первой учитывалось механическое воздействие: на лицевые поверхности пластины действует распределенная нагрузка и поперечная сила на левом конце, а потенциалы на электродах равны нулю. Во второй задаче механические нагрузки отсутствовали, но задавалась разность потенциалов на электродах. На основе гипотез о распределении деформаций, механических

напряжений и электрического потенциала обе задачи были сведены к системе обыкновенных дифференциальных уравнений и граничных условий. Сравнение с результатами расчетов методом конечных элементов в пакете ACELAN показали адекватность предложенной прикладной теории в низкочастотной области.

Обсуждение и заключение. Поскольку постановка задачи рассматривалась в линейной теории электроупругости и изучалась низкочастотная область, в работе удалось задачу об изгибных и сдвиговых колебаниях пластины из пористой пьезокерамики разделить на две: изгибную — с механическим воздействием при нулевых потенциалах и сдвиговую — при задании разности потенциалов и нулевом механическом воздействии. Использованы соответствующие гипотезы об изгибе и сдвиге, построены две системы обыкновенных дифференциальных уравнений и граничных условий, которые решаются аналитически без использования «тяжелых» конечно-элементных пакетов. Для сравнения результатов и подтверждения адекватности предложенного метода проведено конечно-элементное моделирование таких задач в специализированном пакете ACELAN. Это сравнение показало, что ошибка в определении смещений и электрического потенциала при использовании этого подхода, в случае задания механических нагрузок и разности потенциалов, не превышает 6 %. Разработанный в статье метод может быть применен при проектировании пьезоэлектрических генераторов накопления энергии в низкочастотной области.

Ключевые слова: устройство сбора энергии, пьезоэлектрический генератор, пористая керамика, изгиб пластины, сдвиг пластины, прикладная теория

Introduction. Piezoelectric generators (PEG) are used to convert mechanical energy into electrical energy, followed by its accumulation. One of the application areas of PEG is the creation of low-power autonomous renewable sources of electric energy. The working element of the PEG is a piezoceramic element of a certain shape. The shape and type of deformation of this element determine the piezomodule, which characterizes the conversion of mechanical deformation energy into electrical energy. Thus, piezomodule d_{33} is associated with tension-and-compression along the axis of polarization, d_{31} — with the same deformation in the transverse direction to this axis, d_{15} — with shear. The use of porous ceramics makes it possible to create more efficient PEG. This is due to the fact that the elastic modules of porous ceramics decrease significantly stronger with increasing porosity than piezomodules. Thus, under the same mechanical load, the deformation amplitude of porous ceramics is greater; therefore, the output electric potential is also greater.

PEG calculation can be performed by the finite element method implemented in ANSYS, ACELAN, COMSOL, and others packages. For piezoelectric elements, one or two sizes of which are significantly smaller than others (plates, rods), applied calculation theories can be constructed based on hypotheses about the distribution of mechanical and electric fields. Without the use of "heavy" finite element packages, applied theories make it possible to model various devices based on piezoactive materials. Piezoelectric, piezomagnetic and composite piezomagnetoelectric materials are considered as such materials. The construction of these theories is based on the acceptance of hypotheses about the distribution of mechanical, electric and magnetic fields. These hypotheses are related to the vibration mode of elastic and piezoactive elements of PEG. The most common designs are active and semipassive bimorphs based on multilayer plates, polarized in thickness with electrodes on the front faces, performing transverse bending vibrations. A number of papers are devoted to the study of devices with shear deformation of piezoelectric elements. An electric model with piezoelectric defining equations of mode d_{15} and a single-degree-of-freedom model were combined to describe the energy collection characteristics of a piezoelectric cantilever in a shear mode in operation [1]. The proposed model is used to simulate the frequency dependence of the output peak voltage and power. The results show a good agreement with the experiment and the finite element calculation in ANSYS. In [2], a piezoelectric shear mode energy converter was developed to use the energy of a pressurized water flow. It converts the energy of the flow into electrical energy through piezoelectric conversion with vibration of the piezoelectric film. A finite element model has been developed to estimate the generated voltage of a piezoelectric film, which is in good agreement with the conducted field experiment. A one-dimensional fully coupled beam vibration model based on Timoshenko-type hypotheses, which provides a single common basis for energy analysis in shear and bending modes, is presented in [3]. In [4], the effect of the inhomogeneity of the properties of the plate under shear and torsional vibrations of its central part was studied. In experimental work [5], a multilayer cylindrical piezoelectric shear actuator (MCPSA) operating in shear mode d_{15}, was presented for precision actuation under high

mechanical load. The actuator was made of piezoelectric ceramic rings Pb(Zr,Ti)O$_3$ (PZT-51), which were concentrically assembled together in an electrically parallel connection with alternately positive and negative polarization in the axial direction. In [6], metamaterial of identical elementary cells was created, an artificial prototype of a device with characteristic patterned electrodes and piezoceramic subunits arranged in a row was designed and manufactured, which, as proven, ideally generated the synthetic shear deformation of the face. At the same excitation voltage, there was an increase in the displacement of the shear type by more than an order of magnitude, compared to the previous volumetric elements in mode d_{15}. In the static formulation in [7], the field of electromechanical coupling in the shear-bending mode for an annular piezoelectric plate was theoretically established. In accordance with the classical theory of elastic plates of small bending and piezoelectric defining equations, an analytical solution of the bending deformation of the piezoactuator under the action of an electric field and a concentrated or evenly distributed mechanical load was achieved. The mechanism of generating bending deformation was explained by axisymmetric shear deformation, which additionally caused bending deformation of one piezoelectric plate in the form of a ring. This mechanism differs significantly from the mechanism of piezoelectric bimorphic or unimorphic drives, which were previously reported. The design of the annular piezoactuator has been optimized. In [8], a one-dimensional model was used to construct a sensor response function based on shear resonators (quartz cuts) of a bulk acoustic wave, which are promising for in-line measurements of fluid viscosity, e.g., in industrial processes. In [9], using the finite element method, a piezoelectric flying height control converter was investigated using a shear model deformation. In [10], the theory of a functionally graded plate with four-unknown shear deformations was used to express the displacement component. The distribution of the electric potential was a linear function of thickness. The plate was under mechanical load and electrical voltage. The basic equations and boundary conditions were derived using the virtual work principle. The analysis of stresses and deformations from the design parameters was performed. The electromechanical analysis of the stability loss of a piezoelectric nanoplate under shear using a modified theory of paired stresses with different boundary conditions was studied in [11]. To take into account the electrical effects, an external electrical voltage was applied to the piezoelectric nanoplate. A simplified theory of the first-order shear deformation was used. The basic differential equations were obtained using the Hamilton principle and nonlinear Von Karman deformations. Finally, the results showed that the effect of external electrical voltage on the critical shear load arising on the piezoelectric nanoplate was insignificant. In [12], using a combination of two classical approaches to modeling the nonlinear behavior of piezoelectric materials, a piezoelectric shear drive for an atomic-force microscope was investigated. Specifically, the novelty of the proposed method was in the fact that it combined two sources of nonlinearity of the field-dependent model from Müller and Zhang with the frequency-dependent model from Damjanović. The numerical results obtained using the finite element method (FEM) were compared to the experiment.

Vibrations in which there is shear in addition to bending are less studied in the scientific literature, i.e., piezomodule d_{15}, is the "working" one, whose value decreases with increasing porosity, but to a lesser extent than elastic modules. The latter circumstance makes it possible to build an efficient energy conversion device. Therefore, the development of an applied theory of PEG calculation using porous piezoceramics based on simplified models without "heavy" finite element packages seems to be a highly relevant task. The objective of this work was to construct an applied calculation method for steady-state transverse vibrations in the low-frequency region of a porous piezoceramic plate characterized by both shear and bending.

Materials and Methods. The PEG under study was a piezoceramic plate (length l, thickness h), polarized in thickness, cantilevered on the right side, the left side was attached to an inertial mass that performed vertical vibrations and was fixed in the horizontal direction. The electrodes were located on the sides of the plate; therefore, with a potential difference on them and no mechanical load, the principal deformation in the low-frequency region was shear. Vibrations whose frequency was less than the frequency of the first resonance were considered.

Mathematical formulation of the problem

The mathematical formulation of the problem is described by a system of differential equations [13] and the corresponding boundary conditions.

$$
\begin{aligned}
&\rho_{pk}\ddot{\mathbf{u}} + \alpha_{dj}\rho_j\dot{\mathbf{u}} - \nabla\cdot\boldsymbol{\sigma} = \mathbf{f}_j && \nabla\cdot\mathbf{D} = 0 \\
&\boldsymbol{\sigma} = \mathbf{c}_j^E\cdot\cdot\left(\boldsymbol{\varepsilon} + \beta_{dj}\dot{\boldsymbol{\varepsilon}}\right) - \mathbf{e}_j^T\cdot\mathbf{E} && \mathbf{E} = -\nabla\varphi \\
&\mathbf{D} + \varsigma_d\dot{\mathbf{D}} = \mathbf{e}_j\cdot\cdot\left(\boldsymbol{\varepsilon} + \varsigma_d\dot{\boldsymbol{\varepsilon}}\right) + \mathfrak{z}_j^S\cdot\mathbf{E} && \boldsymbol{\varepsilon} = \left(\nabla\mathbf{u} + \nabla\mathbf{u}^T\right)/2
\end{aligned}
\tag{1}
$$

When considering porous ceramics of connectivity 3–0, equations (1) use effective physical constants determined through the ACELAN-COMPOS package [14]. These effective properties based on representative volumes (Fig. 1) were obtained in [15]. They are presented in Table 1.

Mechanics
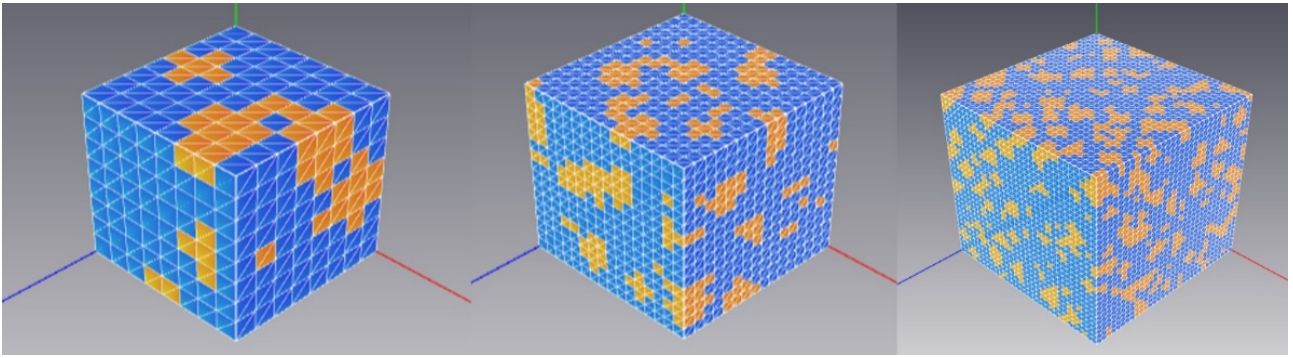
Fig. 1. Representative volumes in ACELAN-COMPOS package [14]

Table 1

Effective properties of porous ceramics

% of porosity	0	10	20	30	40	50	60	70	80
ρ , kg/m³	7,500	6,750	6,000	5,250	4,500	3,750	3,000	2,250	1,500
$c_{11}^{E\,\mathrm{eff}}$, 10^{10} , N/m²	13.90	11.56	9.25	6.85	5.05	3.34	2.07	1.26	0.68
$c_{12}^{E\,\mathrm{eff}}$, 10^{10} , N/m²	7.78	6.15	4.66	3.14	2.10	1.16	0.62	0.28	0.13
$c_{13}^{E\,\mathrm{eff}}$, 10^{10} , N/m²	7.43	5.82	4.25	2.82	1.70	1.06	0.52	0.24	0.10
$c_{33}^{E\,\mathrm{eff}}$, 10^{10} , N/m²	11.50	9.53	7.23	5.42	3.91	2.72	1.63	0.91	0.47
$c_{44}^{E\,\mathrm{eff}}$, 10^{10} , N/m²	2.56	2.23	1.83	1.44	1.10	0.74	0.44	0.23	0.10
e_{33}^{eff} , C/m²	15.10	13.38	11.37	9.59	7.68	5.93	3.93	2.30	1.25
e_{31}^{eff} , C/m²	−5.20	−4.23	−3.14	−2.07	−1.32	−0.75	−0.43	−0.21	−0.10
e_{31}^{eff} , C/m²	12.70	10.96	8.96	6.91	5.00	3.30	1.95	1.00	0.44
$\kappa_{11}^{S\,\mathrm{eff}} / \varepsilon_0$	730	663	582	509	439	349	263	191	122
$\kappa_{33}^{S\,\mathrm{eff}} / \varepsilon_0$	635	567	492	413	345	270	199	130	75

According to Table 1, the dependences of effective elastic modules and piezomodules on the percentage of porosity [15] are plotted. They are shown in Figure 2.
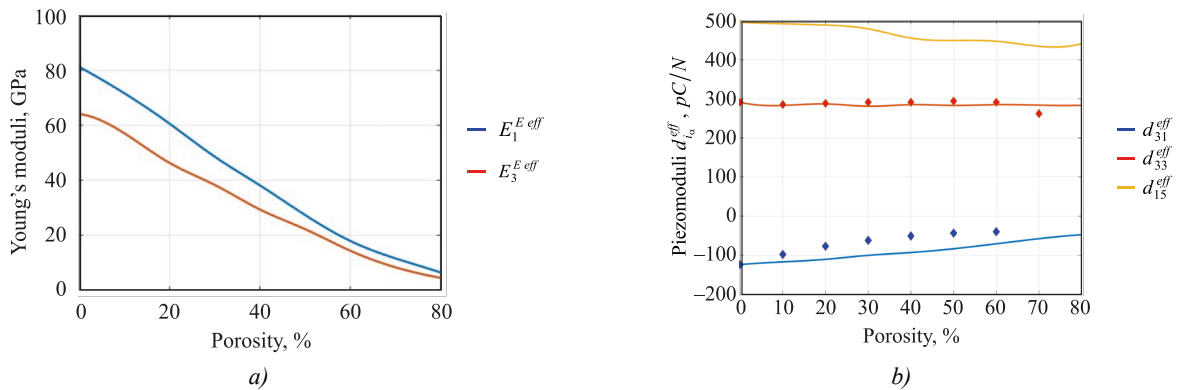
Fig. 2. Dependences of values on percentage of porosity [15]: *a* — elastic models; *b* — piezomodules [15]

In accordance with the results shown in Figure 2, elastic modulus E_1 decreases significantly faster than piezomodule d_{15}.

Building an applied theory

The developed calculation method consists of solving two problems: in the first, bending under the effect of a mechanical load with zero potential difference is considered; in the second, the shear caused by a potential difference in the absence of a mechanical load is modeled. In both cases, the absence of charges on the front faces of the plate is taken into account. Under the action of a mechanical load and an electrical potential difference, the results of the two tasks add up due to the linearity of the task.

The action of the mechanical load, the potentials on the electrodes are zero. Hypotheses of the Kirchhoff-Love type are accepted regarding the equality of normal stresses to zero, and for displacements:

$$u_3 = UZ_2(x), \; u_1 = -\left(\frac{d}{dx}UZ_2(x)\right)z. \tag{2}$$

The distribution of electric potential over the thickness is assumed to be quadratic and symmetrical:

$$\phi = \Phi_1(x)z\left(2,\frac{z}{h}-1\right)h^{-1} + \Phi_1(x)z\left(1+2\frac{z}{h}\right)h^{-1} + \Phi_2(x)\left(1-4\frac{z^2}{h^2}\right). \tag{3}$$

To take into account the boundary conditions at the ends of the plate ($x = 0, l$), an expression for the transverse force is obtained:

$$Q_1 = \left(-\frac{1}{12}\left(-\frac{c_{13}e_{33}\left(\frac{8c_{33}g_{33}+8e_{33}^2}{\left(c_{33}g_{33}+e_{33}^2\right)}-\frac{8}{h^2}\right)}{c_{33}}+e_{31}\left(\frac{8c_{33}g_{33}+8e_{33}^2}{\left(c_{33}g_{33}+e_{33}^2\right)h^2}-\frac{8}{h^2}\right)\right)h^3 \right.$$

$$\left. -\frac{1}{12}e_{15}\left(\frac{1}{2}\frac{8c_{33}g_{33}+8e_{33}^2}{\left(c_{33}g_{33}+e_{33}^2\right)h^2}-\frac{4}{h^2}\right)h^3 - e_{15}h\right)\left(\frac{d}{dx}\Phi_2(x)\right) +$$

$$+\left(-\frac{1}{12}\left(-c_{11}-\frac{c_{13}\left(\frac{e_{33}\left(c_{13}e_{33}h^2-c_{33}e_{31}h^2\right)}{\left(c_{33}g_{33}+e_{33}^2\right)h^2}-c_{13}\right)}{c_{33}}+\frac{e_{31}\left(c_{13}e_{33}h^2-c_{33}e_{31}h^2\right)}{\left(c_{33}g_{33}+e_{33}^2\right)h^2}\right)h^3 \right.$$

$$\left. -\frac{1}{24}\frac{e_{15}\left(c_{13}e_{33}h^2-c_{33}e_{31}h^2\right)h}{c_{33}g_{33}+e_{33}^2}\right)\left(\frac{d^3}{dx^3}UZ_2(x)\right). \tag{4}$$

Taking into account the equality of the normal component of the electric induction vector on the front faces ($z = \pm h$) to zero, the equations for the unknown deflection $UZ_2(x)$ and distribution of the electric potential $\Phi_2(x)$ have the form:

$$\left(-\frac{1}{2}\left(-\frac{c_{13}e_{33}\left(\frac{8c_{33}g_{33}+8e_{33}^2}{\left(c_{33}g_{33}+e_{33}^2\right)}-\frac{8}{h^2}\right)}{c_{33}}+e_{31}\left(\frac{8c_{33}g_{33}+8e_{33}^2}{\left(c_{33}g_{33}+e_{33}^2\right)h^2}-\frac{8}{h^2}\right)\right)h^3 \right.$$

$$\left. -\frac{1}{2}e_{15}\left(\frac{1}{2}\frac{8c_{33}g_{33}+8e_{33}^2}{\left(c_{33}g_{33}+e_{33}^2\right)h^2}-\frac{4}{h^2}\right)h^3 - e_{15}h\right)\left(\frac{d^2}{dx^2}\Phi_2(x)\right) +$$

$$+\left(-\frac{1}{2}\left(-c_{11}-\frac{c_{13}\left(\frac{e_{33}\left(c_{13}e_{33}h^2-c_{33}e_{31}h^2\right)}{\left(c_{33}g_{33}+e_{33}^2\right)h^2}-c_{13}\right)}{c_{33}}+\frac{e_{31}\left(c_{13}e_{33}h^2-c_{33}e_{31}h^2\right)}{\left(c_{33}g_{33}+e_{33}^2\right)h^2}\right)h^3 \right.$$

$$\left. -\frac{1}{24}\frac{e_{15}\left(c_{13}e_{33}h^2-c_{33}e_{31}h^2\right)h}{c_{33}g_{33}+e_{33}^2}\right)\left(\frac{d^4}{dx^4}UZ_2(x)\right) - W^2\rho h UZ_2(x) - p(x) = 0, \tag{5}$$

Mechanics

$$\left[\begin{array}{l} -\dfrac{e_{33}^2\left(\dfrac{8c_{33}g_{33}+8e_{33}^2}{\left(c_{33}g_{33}+e_{33}^2\right)h^2}-\dfrac{8}{h^2}\right)}{c_{33}}-g_{33}\left(\dfrac{8c_{33}g_{33}+8e_{33}^2}{\left(c_{33}g_{33}+e_{33}^2\right)h^2}-\dfrac{8}{h^2}\right) \end{array}\right]\varPhi_2(x)+$$

$$+\left(-g_{11}-\frac{1}{2}g_{11}\left(\frac{1}{2}\frac{8c_{33}g_{33}+8e_{33}^2}{\left(c_{33}g_{33}+e_{33}^2\right)h^2}-\frac{4}{h^2}\right)h^2\right)\left(\frac{d^2}{dx^2}\varPhi_2(x)\right)+$$

$$+\left[-\frac{g_{33}\left(c_{13}e_{33}h^2-c_{33}e_{31}h^2\right)}{\left(c_{33}g_{33}+e_{33}^2\right)h^2}-e_{31}-\frac{e_{33}\left(\dfrac{\left(c_{13}e_{33}h^2-c_{33}e_{31}h^2\right)}{\left(c_{33}g_{33}+e_{33}^2\right)h^2}-c_{13}\right)}{c_{33}}\right]\left(\frac{d^2}{dx^2}UZ_2(x)\right)-$$

$$-\frac{1}{24}\frac{g_{11}\left(c_{13}e_{33}h^2-c_{33}e_{31}h^2\right)\left(\dfrac{d^4}{dx^4}UZ_2(x)\right)}{c_{33}g_{33}+e_{33}^2}=0.\tag{6}$$

The potential difference is set, the mechanical load is zero. Independence of lateral displacement from thickness, equality of the longitudinal displacement to zero, and the quadratic distribution of the electric potential over the thickness are assumed (3):

$$u_3=UZ_2(x),\, u_1=0.\tag{7}$$

Expression for the transverse force:

$$Q_1=-c_{44}\left(\frac{d}{dx}UZ_2(x)\right)h-e_{15}\left(\frac{d}{dx}\varPhi_2(x)\right)h.\tag{8}$$

Taking into account the equality of the normal component of the electric induction vector on the front faces ($z=\pm h$) to zero, the equations for the unknown deflection $UZ_2(x)$ and distribution of the electric potential $\varPhi_2(x)$ have the form:

$$-c_{44}\left(\frac{d^2}{dx^2}UZ_2(x)\right)h-e_{15}\left(\frac{d^2}{dx^2}\varPhi_2(x)\right)h-p(x)-W^2\rho h UZ_2(x)=0,\tag{9}$$

$$e_{15}\frac{d^2}{dx^2}UZ_2(x)-g_{11}\frac{d^2}{dx^2}\varPhi_2(x)=0.\tag{10}$$

Research Results. The results of calculations based on the proposed applied theories were compared to the calculations of piezoelectric element vibrations ($l=0.1$ m, $h=0.01$ m) at a frequency equal to 100 s^{-1} by the finite element method in ACELAN [16].

In the first problem, defined by equations (5) and (6), when specifying a uniformly distributed load $p(x)=1000$ Pa·m and with boundary conditions:

$$\frac{d}{dx}UZ_2(0)=0,\, Q_1\mid_{x=0}=0,\, \varPhi_2(0)=\varPhi_2(l)=0,\, UZ_2(l)=0,\, \frac{d}{dx}UZ_2(l)=0,\tag{11}$$

the following results were obtained, shown in Figures 3, 4.

The calculations showed that the error in determining the vertical displacement was 5.8%, and for the horizontal displacement, it was 1.2%.
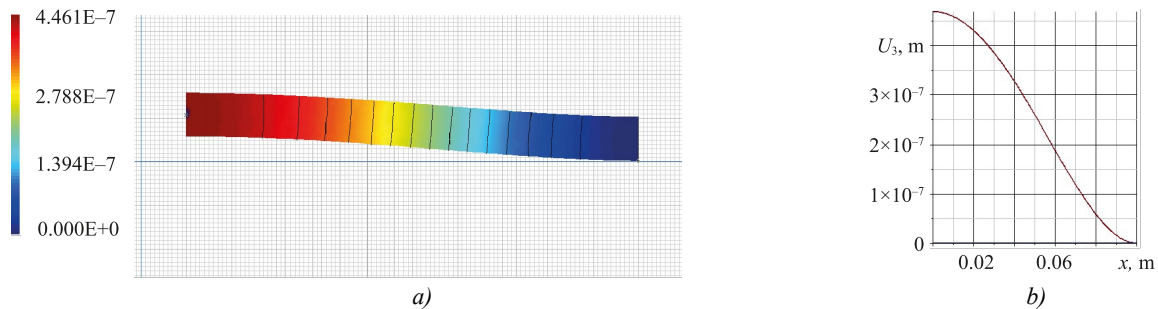
Fig. 3. Vertical displacement in ACELAN in the first problem: *a* — distribution; *b* — graph on the upper boundary

3.268E–8

8.141E–9

–8.151E–9

–3.259E–8

a)

U_1, m

3×10^{-8}

2×10^{-8}

1×10^{-8}

0

0.02 0.04 0.06 0.08 *x*, m

b)
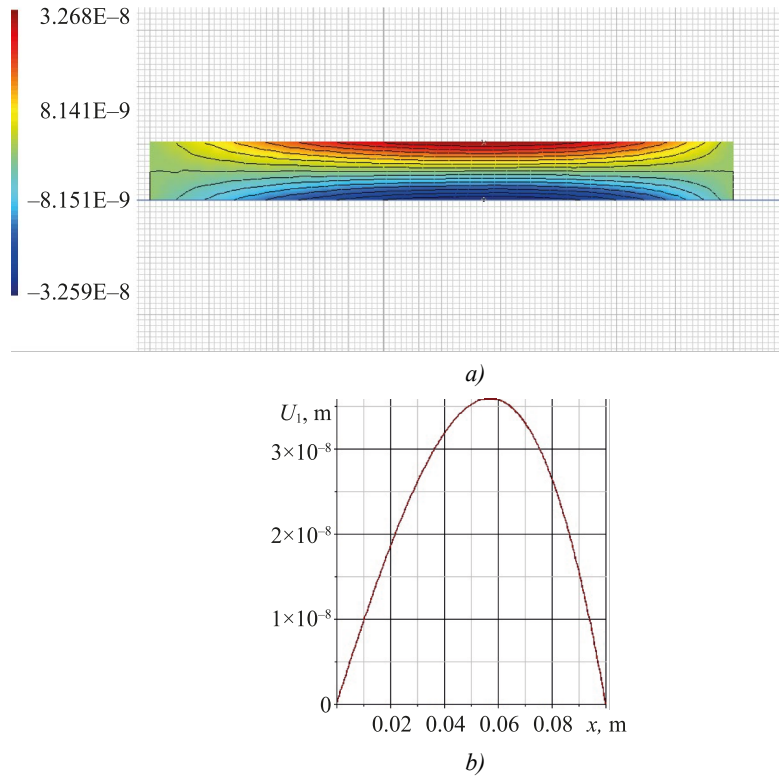
Fig. 4. Horizontal displacement in ACELAN in the first problem: *a* — distribution; *b* — graph on the upper boundary

In the second problem, defined by equations (8) and (9), when setting zero load $p(x) \equiv 0$, potential difference $V_0 = 100$ W and with boundary conditions:

$$Q_1 \mid_{x=0} = 0,\ \Phi_2(0) = 0,\ \Phi_2(l) = V_0,\ UZ_2(l) = 0, \tag{12}$$

the following results were obtained, shown in Figures 5, 6.

5.006E–8

3.129E–8

1.877E–8

0.000E–0

a)

U_3, m

4×10^{-8}

3×10^{-8}

3×10^{-8}

2×10^{-8}

0

0.02 0.04 0.06 0.08 *x*, m

b)
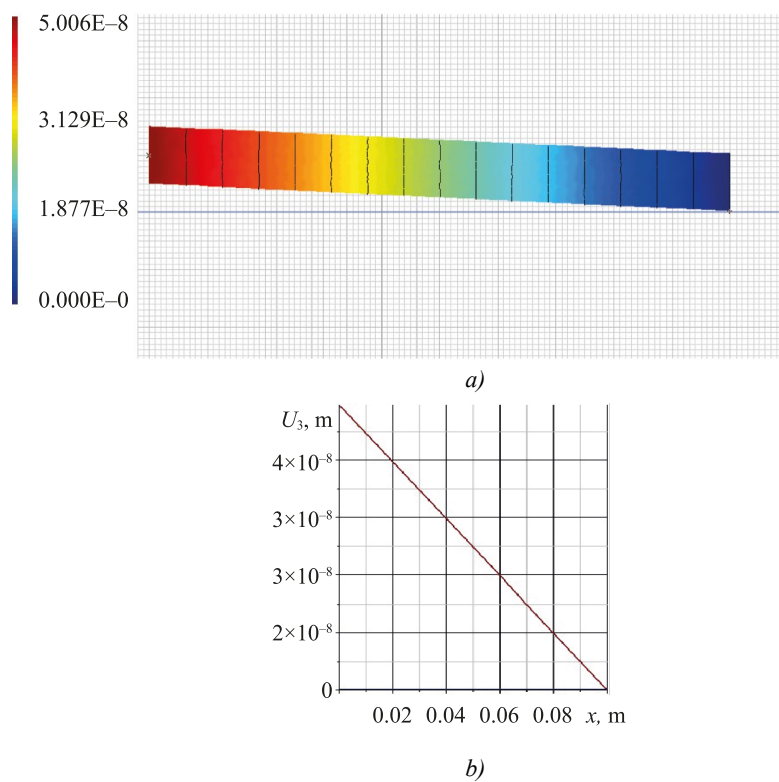
Fig. 5. Vertical displacement in ACELAN in the second problem: *a* — distribution; *b* — graph on the upper boundary

Mechanics

155

a)

b)
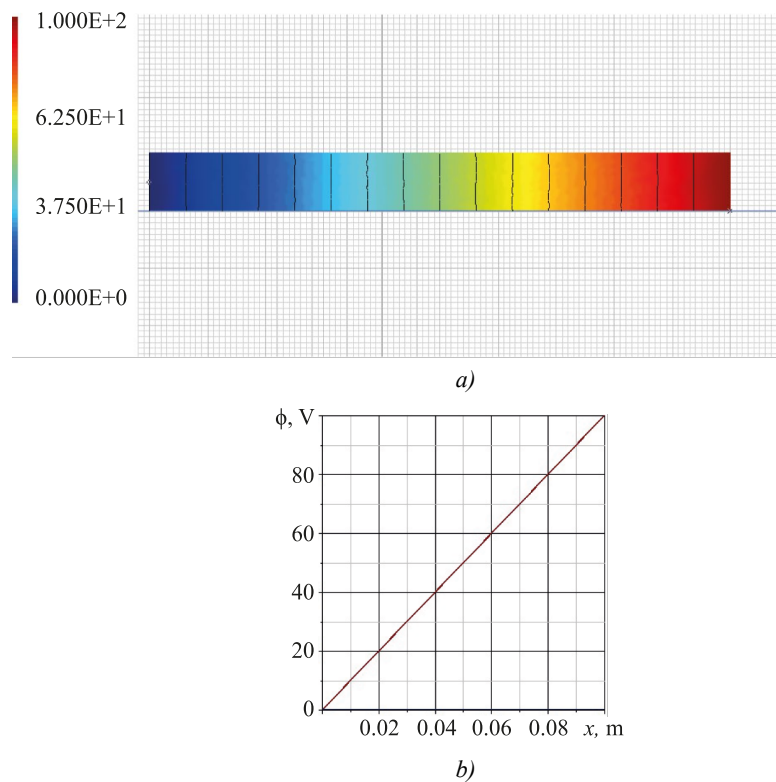
Fig. 6. Electric potential in ACELAN in the second problem: *a* — distribution;
b — dependence on the longitudinal coordinate in the middle of the thickness

The calculations showed that the error in determining the vertical displacement was 0.8%, and for the electric potential, it was less than 1%. It should be noted that the values of the horizontal displacement calculated in ACELAN turned out to be three orders of magnitude less than the maximum vertical displacement, which indicated the adequacy of the hypothesis (7).

When setting mechanical loads and potential differences, the error of the proposed method turned out to be about 6 % for the displacement and electrical potential components.

Discussion and Conclusion. As noted in the cited literature, the simultaneous use of bending and shear of a piezoelectric element can significantly increase its efficiency. In addition, the use of porous ceramics, due to different dependences of elastic modules and piezomodules on the percentage of porosity, also improves the output characteristics of PEG.

In this paper, due to the linear formulation in the theory of electroelasticity, it was possible to develop an applied theory for calculating bending-shear vibrations of a piezoelectric element in the low-frequency region, which consisted of solving two problems: in the first, mechanical loads operated at zero potentials, and in the second, on the contrary, there were zero mechanical loads, and a potential difference was set. Based on various hypotheses about the distribution of mechanical and electric fields, two boundary value problems for systems of ordinary differential equations were obtained, which were solved analytically. The results of the calculation of displacements and electric potential were compared using the proposed method and the FEM implemented in the ACELAN package. These calculations validated the applicability of the proposed method, the error for which in calculating the above characteristics was 6%. This accuracy is sufficient for engineering calculations; therefore, the proposed method can be applied in the design of piezoelectric devices, including the collection and storage of energy. Further development of this applied theory will be aimed at covering a wider frequency range, including the first flexural shear resonance.

References

1. Liang Zhou, Jing Sun, Xuejun Zheng, Shuifeng Deng, Jihe Zhao, Jihe Zhao, et al. A Model for the Energy Harvesting Performance of Shear Mode Piezoelectric Cantilever. *Sensors and Actuators A: Physical.* 2012;179:185–192. http://doi.org/10.1016/j.sna.2012.02.041

2. Dung-An Wang, Nine-Zeng Liu. A Shear Mode Piezoelectric Energy Harvester Based on a Pressurized Water Fow. *Sensors and Actuators A: Physical.* 2011;167(2):449–458. https://doi.org/10.1016/j.sna.2011.03.003

3. Shreya Banerjee, Sitikantha Roy. A Timoshenko like Model for Piezoelectric Energy Harvester with Shear Mode. *Composite Structures.* 2018;204:677–688. https://doi.org/10.1016/j.compstruct.2018.07.117

4. Yanping Kong, Jinxi Liu. Vibration Confinement of Thickness-Shear and Thickness-Twist Modes in a Functionally Graded Piezoelectric Plate. *Acta Mechanica Solida Sinica.* 2011;24(4):299–307. https://doi.org/10.1016/S0894-9166(11)60031-1

5. Xiangyu Gao, Xudong Xin, Jingen Wu, Zhaoqiang Chu, Shuxiang Dong. A Multilayered-Cylindrical Piezoelectric Shear Actuator Operating in Shear (d_{15}) Mode. *Applied Physics Letters.* 2018;112:152902. http://doi.org/10.1063/1.5022726

6. Jikun Yang, Qiang Huan, Yang Yu, Jingen Wu, Zhaoqiang Chu, Mohammadjavad Pourhosseiniasl, et al. Tailoring Artificial Mode to Enable Cofired Integration of Shear-type Piezoelectric Devices. *Advanced Science.* 2020;7(17):2001368. https://doi.org/10.1002/advs.202001368

7. Zejun Yu, Shuxiang Dong, Daining Fang. Theoretical Analysis on Shear-Bending Deflection of a Ring-Shape Piezoelectric Plate. *AIP Advances.* 2016;6(2):025124. https://doi.org/10.1063/1.4943219

8. Ewald Benesa, Helmut Nowotny, Stefan Braun, Stefan Radel, Martin Greöschl. Analytical Sensor Response Function of Viscosity Sensors Based on Layered Piezoelectric Thickness Shear Resonators. *Physics Procedia*. 2015;70:236–240. http://doi.org/10.1016/j.phpro.2015.08.144

9. Hui Lia, Shengnan Shenb, Kensuke Amemiya, Bo Liu, Hejun Du. Simulation of Piezoelectric Flying Height Control Slider Using Shear-Mode Deformation. *Physics Procedia.* 2011;16:101–110. https://doi.org/10.1016/j.phpro.2011.06.115

10. Zenkour AM, Alghanmi RA. Stress Analysis of a Functionally Graded Plate Integrated with Piezoelectric Faces via a Four-Unknown Shear Deformation Theory. *Results in Physics.* 2019;12:268–277. https://doi.org/10.1016/j.rinp.2018.11.045

11. Mohammad Malikan. Electro-Mechanical Shear Buckling of Piezoelectric Nanoplate Using Modified Couple Stress Theory Based on Simplified First Order Shear Deformation Theory. *Applied Mathematical Modelling.* 2017;48:196–207. https://doi.org/10.1016/j.apm.2017.03.065

12. Bo Xue, Emmanuel Brousseau, Chris Bowen. Modelling of a Shear-type Piezoelectric Actuator for AFM-based Vibration-assisted Nanomachining. *International Journal of Mechanical Sciences.* 2023;243:108048. https://doi.org/10.1016/j.ijmecsci.2022.108048

13. Belokon' AV, Eremeev VA, Nasedkin AV, Solov'ev AN. Partitioned Schemes of the Finite-Element Method for Dynamic Problems of Acoustoelectroelasticity. *Journal of Applied Mathematics and Mechanics.* 2000;64(3):381–393.

14. Kudimova AB, Nadolin DK, Nasedkin AV, Nasedkina AA, Oganesyan PA, Soloviev AN. Finite Element Homogenization of Piezocomposites with Isolated Inclusions Using Improved 3-0 Algorithm for Generating Representative Volumes in ACELAN-COMPOS Package. *Materials Physics and Mechanics.* 2020;44(3):392–403. https://doi.org/10.18720/MPM.4432020_10

15. Nasedkin AV, Oganesyan PA, Soloviev AN. Analysis of Rosen Type Energy Harvesting Devices from Porous Piezoceramics with Great Longitudinal Piezomodulus. *Zeitschrift für Angewandte Mathematik und Mechanik.* 2021;101(3):e202000129. https://doi.org/10.1002/zamm.202000129

16. Nasedkin AV, Skaliukh AS, Soloviev AN. ACELAN Package and Finite Element Modeling of Hydroacoustic Piezoelectric Transducers. *Bulletin of Higher Education Institutes. North-Caucasian Region. Natural Sciences.* 2001;S1:122–125. (In Russ.).

About the Authors:

Arkadiy N. Soloviev, Dr.Sci. (Phys.-Math.), Professor of the Mathematics and Physics Department, Crimean Engineering and Pedagogical University named after Fevzi Yakubov (8, Uchebnyi Lane, Simferopol), Professor of the Theoretical and Applied Mechanics Department, Don State Technical University (1, Gagarin sq., Rostov-on-Don, 344003, Russian Federation), Chief Researcher, Southern Federal University (105/42, Bolshaya Sadovaya Str., Rostov-on-Don, 344006, Russian Federation), SPIN-code: 8087-8998, ORCID, ResearcherID, ScopusID, solovievarc@gmail.com

Valery A. Chebanenko, Cand.Sci. (Phys.-Math.), Senior Researcher, Laboratory of Transport, Composite Materials and Structures, Southern Research Center, Russian Academy of Sciences (41, Chekhova Av., Rostov-on-Don, 344006, RF), SPIN-code: 6487-3095, ORCID, ResearcherID, ScopusID, valera.chebanenko@yandex.ru

Pavel A. Oganesyan, Cand.Sci. (Phys.-Math.), Associate Professor of the Mathematical Modeling Department, Institute of Mathematics, Mechanics and Computer Science, Southern Federal University (8a, Milchakova Str., Rostov-on-Don, 344058, Russian Federation), SPIN-code: 3870-0861, ORCID, ResearcherID, ScopusID, oganesyan@hey.com

Mechanics

Elizaveta I. Fomenko, graduate student of the Mathematical Modeling Department, Institute of Mathematics, Mechanics and Computer Science, Southern Federal University (8a, Milchakova Str., Rostov-on-Don, 344058, Russian Federation), SPIN-code: 6176-3556, ORCID, ScopusID, elfomenko@sfedu.ru

Об авторах:

Аркадий Николаевич Соловьев, доктор физико-математических наук, профессор кафедры математики и физики Крымского инженерно-педагогического университета им. Февзи Якубова (г. Симферополь, пер. Учебный, д. 8), профессор кафедры теоретической и прикладной механики Донского государственного технического университета (344003, Российская Федерация, г. Ростов-на-Дону, пл. Гагарина, 1), главный научный сотрудник Южного федерального университета (344006, Российская Федерация, г. Ростов-на-Дону, ул. Большая Садовая, 105/42). SPIN-код: 8087-8998, ORCID, ResearcherID, ScopusID, solovievarc@gmail.com

Валерий Александрович Чебаненко, кандидат физико-математических наук, старший научный сотрудник лаборатории транспорта, композиционных материалов и конструкций федерального исследовательского центра «Южный научный центр Российской академии наук» (344006, Российская Федерация, г. Ростов-на-Дону, пр. Чехова, 41), SPIN-код: 6487-3095, ORCID, ResearcherID, ScopusID, valera.chebanenko@yandex.ru

Павел Артурович Оганесян, кандидат физико-математических наук, доцент кафедры математического моделирования института математики, механики и компьютерных наук им. И.И. Воровича Южного Федерального университета (344058, Российская Федерация, г. Ростов-на-Дону, ул. Мильчакова, 8 а), SPIN-код: 3870-0861, ORCID, ResearcherID, ScopusID, oganesyan@hey.com

Елизавета Ивановна Фоменко, магистрант кафедры математического моделирования института математики, механики и компьютерных наук им. И.И. Воровича Южного Федерального университета (344058, Российская Федерация, Ростов-на-Дону, ул. Мильчакова, 8 а), SPIN-код: 6176-3556, ORCID, ScopusID, elfomenko@sfedu.ru

Claimed Contributorship:

AN Soloviev: task setting, literature review, research objectives and tasks.

VA Chebanenko: derivation of equations of the applied theory and performing the calculations using them, formulation of conclusions.

PA Oganesyan: building a finite element model, formulation of conclusions.

EI Fomenko: computational analysis in the ACELAN package, revision of the text.

Заявленный вклад авторов:

А.Н. Соловьев: постановка задачи, обзор литературы, цели и задачи исследования.

В.А. Чебаненко: вывод уравнений прикладной теории и проведение расчетов с их использованием, формирование выводов.

П.А. Оганесян: построение конечно элементной модели, формирование выводов.

Е.И. Фоменко: проведение расчетов в пакете ACELAN, доработка текста.

Conflict of Interest Statement: **the authors declare no conflict of interest.**

Конфликт интересов: **авторы заявляют об отсутствии конфликта интересов.**

All authors have read and approved the final manuscript.

Все авторы прочитали и одобрили окончательный вариант рукописи.

MECHANICS
МЕХАНИКА

Simplified Calculation of the Inertia Moment of the Cross Section of the Console under Loading

Evgeny E. Deryugin [ORCID]

Institute of Strength Physics and Materials Science, Siberian Branch of Russian Academy of Sciences, Tomsk, Russian Federation

✉ dee@ispms.ru

EDN: YAIWEZ

Abstract

Introduction. Published studies on the rigidity of consoles under load focus on the issues of their deformation and destruction. Calculations of the inertia moment, fundamentally important characteristic of the strength of the rod, are described. However, the problem of significant time consumption for such calculations has not been solved. The presented study meets the lack. The objective of the work is to describe a new rapid method for analytical calculation of the shear stress distribution in the section of the console corresponding to the action of an external applied force. For the first time, tangential stresses are considered, and examples of calculating the inertia moment for two non-standard sections of the console are given in this context.

Materials and Methods. To develop a new method, the console was presented as a pack of plates oriented parallel to the vector of external force. The source calculations were based on the scheme of a console beam with a dedicated plate. The deformation of the rod elements was modeled taking into account the effect of a uniform shear stress field in the plate section. To validate the simplified calculation of the inertia moment of the sections, schemes of a square, ellipse, triangle, hexagon, six-pointed star, and a figured cross were used. Analytical and mathematical research methods were applied, specifically, the Huygens–Steiner theorem.

Results. A rapid valid method for calculating the inertia moment of the cross section of the console under loading has been developed. Its difference is the rejection of calculations for each section, taking into account the shape and other features. For any shape of the section, the beam is represented as a bundle of infinitely thin plates, their inertia moments are integrated, and a well-known solution for deflection of a thin plate is used. The method allows us to unambiguously show the distribution of tangential stresses at the end of the console, providing a given deflection, and tangential stresses are used for such solutions for the first time. Their profiles are obtained depending on the direction of the external applied force. Formulas for the inertia moments of complex sections — a six-pointed star and a figured cross — are derived for the first time. Each section is correlated with the stress distribution curve and its maximum value. This data is visualized in the form of diagrams. It is found that the inertia moment and the rigidity of the console do not change when the external applied force is rotated by 30° for a star-shaped section and by 45° for a square and a figured cross. In general, the tangent field depends on the geometry and on the orientation of the section relative to the external applied force.

Discussion and Conclusion. The proposed simplified approach to calculating the inertia moment of the cross sections of the consoles makes it possible to uniquely determine the field of tangential stresses at the end, which provides the appropriate value of the external applied force for the given deflection. Engineers and mechanics can use the results of the presented work in the calculations and modeling of deformation of rod structural elements.

Keywords: rod deformation, inertia moment of a flat figure, inertia moment of complex sections, elastic deflection of the console, shear stress distribution

Mechanics

Original Theoretical Research

Упрощенный расчет момента инерции поперечного сечения консоли под нагрузкой

Е.Е. Дерюгин 🆔

Институт физики прочности и материаловедения Сибирского отделения Российской академии наук, г. Томск, Российская Федерация

✉ dee@ispms.ru

Аннотация

Введение. Опубликованные исследования жесткости консолей под нагрузкой фокусируются на вопросах их деформации и разрушения. Описаны расчеты момента инерции — принципиально важной характеристики прочности стержня. Однако не решена проблема значительных затрат времени для таких вычислений. Представленное исследование восполняет данный пробел. Цель работы — описание нового быстрого метода аналитического расчета распределения напряжения сдвига в сечении консоли, соответствующего действию внешней приложенной силы. Впервые в таком контексте рассматриваются касательные напряжения и приводятся примеры расчета момента инерции для двух нестандартных сечений консоли.

Материалы и методы. Для создания нового метода консоль представили как пачку пластинок, ориентированных параллельно вектору внешней силы. Исходные расчеты строили по схеме консольной балки с выделенной пластинкой. Деформацию стержневых элементов моделировали с учетом действия однородного поля напряжения сдвига в сечении пластинки. Для обоснования упрощенного расчета момента инерции сечений задействовали схемы квадрата, эллипса, треугольника, шестиугольника, шестиконечной звезды и фигурного креста. Использовали аналитические и математические методы исследования, в частности теорему Гюйгенса–Штейнера.

Результаты исследования. Создан быстрый универсальный метод вычислений момента инерции поперечного сечения консоли под нагрузкой. Его отличие — отказ от расчетов для каждого сечения с учетом формы и других особенностей. При любой форме сечения балка представляется как пачка бесконечно тонких пластинок, моменты их инерции интегрируются, и используется известное решение для прогиба тонкой пластинки. Метод позволяет однозначно показать распределение касательных напряжений на торце консоли, обеспечивающих заданный прогиб, причем впервые для таких решений используются касательные напряжения. Получены их профили в зависимости от направления внешней приложенной силы. Впервые выведены формулы для моментов инерции сложных сечений — шестиконечной звезды и фигурного креста. Каждое сечение соотнесено с кривой распределения напряжения и его максимальным значением. Эти данные визуализированы в виде диаграмм. Установлено, что момент инерции и жесткость консоли не меняются при повороте внешней приложенной силы на 30° для сечения в виде звезды и на 45° — для квадрата и фигурного креста. В общем случае поле касательных зависит от геометрической формы и от ориентации сечения относительно внешней приложенной силы.

Обсуждение и заключение. Предложенный упрощенный подход к расчету момента инерции поперечных сечений консолей дает возможность однозначно определить поле касательных напряжений на торце, обеспечивающее при заданном прогибе соответствующее значение внешней приложенной силы. Инженеры и механики могут использовать результаты представленной работы при расчетах и моделировании деформации стержневых элементов конструкций.

Ключевые слова: деформация стержня, момент инерции плоской фигуры, момент инерции сложных сечений, упругий прогиб консоли, распределение касательных напряжений

Introduction. Numerous building structures contain elements in the form of rods, which undergo elastic deformations during manufacture or operation [1]. The bending strength of a rod or beam determines the bearing capacity of the structure [2]. The ability of a beam to elastic deformation is characterized by stiffness, defined as the ratio of load P to the elastic deflection of the beam λ_e : $m_x = P / \lambda_e$ [3]. As a rule, under laboratory conditions, stiffness is checked on a console beam. One end of it is embedded in a rigid base, and an external force, directed perpendicular to the axis of the beam, acts on the other one [4]. Modeling and calculations of deformation and fracture characteristics of rods, as a rule, are associated with solving the problem of deflection of a console beam, or console, under the action of an external applied force [5]. At the same time, there are no publications on simple and valid methods for determining the inertia moments of complex sections relative to the action of an external applied force. The solution to this problem is described in the presented article.

This work is aimed at the creation of a valid, rapid method for calculating the inertia moments of complex console sections under the action of an external applied force. The new approach provides analytical determination of the shear stress distribution in the section corresponding to the action of an external applied force. It should be noted that earlier, tangential stresses were not taken into account in such calculations. In addition, for the first time, examples of calculating the moment of inertia for complex figured sections are given.

Materials and Methods. In a number of works on the resistance of materials, e.g., in [6], a universal formula is given for calculating the elastic deflection of console λ_e. According to this formula, the rigidity of the console is:

$$P/\lambda_e = 3EI_x/L^3 , \tag{1}$$

where E — Young's modulus; L — length of the console; I_x — inertia moment of the cross-section of the beam relative to x-axis, passing through the center of gravity of the section perpendicular to the applied force P.

It follows from equation (1) that a fundamentally important characteristic of the console is the inertia moment of section I_x, whose value depends on the geometry of the cross-section of the beam and the direction of x-axis [7]. It should be emphasized that in equation (1), inertia moment I_x refers to x-axis, which is perpendicular to the direction of the external applied force P. Specifically, the inertia moment of rectangular section $a \times b$ relative to the axis of symmetry x is equal to [8]:

$$I_x = ab^3 / 12. \tag{2}$$

Here, a — thickness of the console, b — its width. Force P is directed parallel to side b of the rectangle.

Substituting (2) into (1), we obtain the well-known equation for the deflection of a rectangular console [9]:

$$\lambda_e = \frac{4P}{Ea}\left(\frac{L}{b}\right)^3 .$$

The cross sections of console beams, or consoles, are different. Figure 1 shows a simple example of a square section console under the action of external force P, directed along the diagonal of a square.
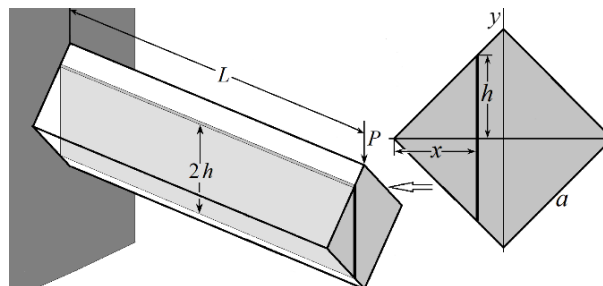
Fig. 1. Diagram of a console beam with a dedicated plate

The inertia moment of the section relative to x-axis is called the sum, or integral, of the products of elemental areas $ds = dxdy$ by the squares of distances y of the areas to x-axis: $I_x = \iint y^2 dxdy$. [10]. The integrand function is virtually the inertia moment of the elemental area $dxdy$ relative to x-axis.

The console can be represented as a pack of extremely thin plates with thickness dx and length L, oriented parallel to the force vector P. Under the action of P, all plates bend by the same amount λ_e. With a given orientation of the console section, a separate plate is not affected by deformation of the rest of the volume. Then, the inertia moment of the section of the console as a whole will be determined by the integral sum of the inertia moments of the sections of all the plates in the pack.

The projection of the plate onto the plane of the console cross section is a rectangular strip with thickness dx and half-length h (Fig. 1). The inertia moment of the section of a separate plate can be considered as the inertia moment of the

Mechanics

console of rectangular section $2h \times dx$. By definition, the equation of type (2) is applicable to each plate in a pack, where $a = dx$ and $b = 2h$. According to this expression, the inertia moment of the strip is $dI_x = 2h^3(x)dx/3$. Thus, the inertia moment of the console section can be determined through integrating the inertia moments of elementary strips rather than elemental areas:

$$I_c = \frac{2}{3}\int_A^B h(x)^3\, dx, \tag{3}$$

where x varies from A to B.

The condition for the orientation of the plane of the plates parallel to the vector of the external applied force is important, since it provides a unique association of the elastic deflection of console λ_e with the distribution of tangential stresses in the cross section of the console. All the plates in the pack bend by the same value λ_e. according to (1), $dI_x = 2h^3(x)dx/3$. This means that elementary force $dP = 3l_e EdI_x/L^3 = 2l_e Eh^3(x)dx/L^3$ is required for a plate with thickness dx. This force corresponds to the action of a uniform shear stress field in the plate section $ds(x) = 2h(x)dx$:

$$\tau = dP/ds = \lambda_e Eh^2(x)/L^3. \tag{4}$$

It can be seen from (4) that the value of voltage λ_e in the coordinate system xy does not depend on coordinate y.

Equation (4) is convenient to be used when modeling the deformation of rod structural elements.

Integral (3) determines the inertia moment of section I_c relative to x-axis, passing through the center of gravity of the section. In the case of asymmetric and complex sections, it is convenient to first find the inertia moment of the section or part of the section relative to the axis that does not pass through the center of gravity of the section. Then, you need to move on to the inertia moment of section I_c relative to the axis that passes through the center of gravity of the section. It is known that the inertia moment of the section repeats the properties of the inertia moment of a solid and obeys the Huygens–Steiner theorem [11]. The inertia moment of section I_x relative to arbitrary x-axis is equal to the sum of the inertia moment of this section I_c relative to the axis passing through the center of gravity of the section parallel to x-axis, and the product of the cross-sectional area S by the square of distance a between the axes: $I_x = I_c + a^2 S$. Therefore, in the general case, we can write:

$$I_x = \frac{2}{3}\int_A^B h(x)^3\, dx + a^2 S = I_c + a^2 S. \tag{5}$$

If x-axis passes through the center of gravity of the section, then distance $a = 0$ and equation (5) turns into (3).

Research Results. To create a simple, fast, valid calculation method, we abandon calculations for each section, taking into account its shape and other features. This approach was implemented for the first time in the framework of this research. No matter how complex the cross-section is, it is quite sufficient to use a well-known solution for deflecting a thin plate, present the beam as a pack of infinitely thin plates, and integrate their inertia moments. In addition, the method allows us to unambiguously show the distribution of tangential stresses at the end of the console, providing a given deflection. It should be emphasized that tangential stresses are considered in this context for the first time.

Short-Cut Calculation of the Inertia Moment of Simple Sections. To validate the proposed method, we consider the known sections of simple geometry. Next, instead of the expression "inertia moment of the cross section of the console", we use the term "inertia moment". We assume that the external applied force is always directed perpendicular to x-axis, relative to which the inertia moment of the section is determined.

Square. Equation (2) is obtained under the condition that the vector of force applied to the end of the console is perpendicular to side a of the rectangle. For $b = a$, we obtain the inertia moment of the square section $I_c = a^4/12$.

Using the proposed method, we find the inertia moment of the square relative to x-axis, which is parallel not to the side, but to the diagonal of the square (Fig. 2 a).
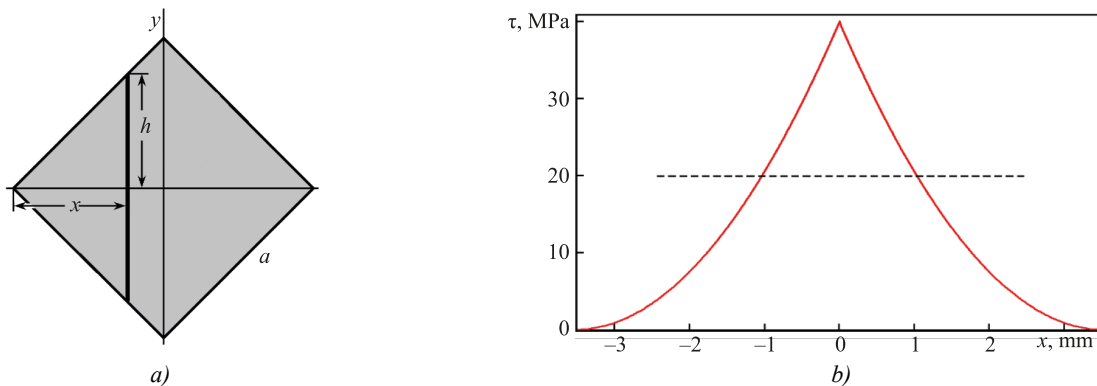
Fig. 2. Cross-section diagram in the form of a square:
a — cross-section; b — voltage distribution τ along x-axis

The half-length of the strip in Figure 1 is equal to $h = x$. From equation (3), we find:

$$I_c = \frac{2}{3}\int_{-a/\sqrt{3}}^{a/\sqrt{3}} x^3 dx = \frac{a^4}{12}.$$

It can be seen that turning x-axis by 45° does not change the inertia moment of the square section. Consequently, when the external applied force is rotated by 45°, the rigidity of the console does not change either (1).

Substituting x in place of h (4), we obtain a shear stress distribution in the section of the square console corresponding to deflection λ_e:

$$\tau(x) = \lambda_e x^2 E / L^3.$$

Figure 2 *b* shows distribution $\tau(x)$ along the diagonal of the square at $\lambda_e = 2$ mm and $a = 5$ mm. According to (1), the action of the shear stress $\tau(x)$ on the end of the steel console ($E = 200$ GPa) with length $L = 50$ mm corresponds to the action of an external applied force $P = 0.25 E \lambda_e a^4 / L^3 = 500$ N. Maximum voltage $\tau_{max} = 40$ MPa is observed on the vertical diagonal of the square. Under the deviating from the diagonal, voltage τ decreases sharply to zero. As a result, a sharp peak is formed in the system $\tau(x)$.

Voltage τ depends only on variable x; therefore, according to the graph in Figure 2 *b*, it is possible to determine value τ at any point of the square.

Obviously, when the force is oriented perpendicular to the sides of the square, $\tau = P/a^2 = 20$ MPa (Fig. 2 *b*, dotted line). As can be seen, stress distribution $\tau(x)$ in the cross section corresponding to external force P significantly depends on its direction.

Ellipse. Figure 3 *a* shows a diagram of an ellipse with semi-axes a and b. The origin of coordinates is in the center of the ellipse.
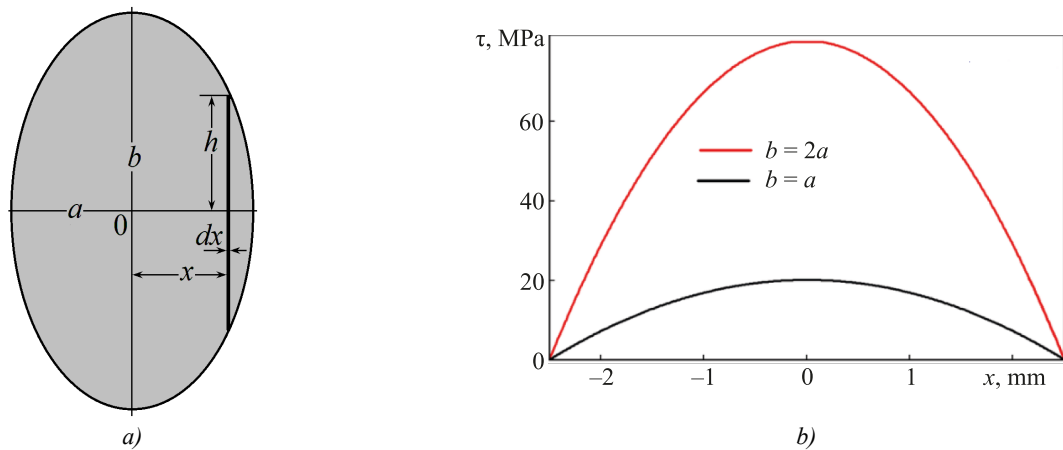
Fig. 3. Section diagram in the form of ellipse with semi-axes a and b:
a — ellipse; *b* — distribution τ along semi-axis a. 1 — a = b, 2 — b = 2a, a = 2.5 mm

It follows from the canonical equation of ellipse [12] that the strip highlighted in Figure 3 has half-length $h = b(a^2 - x^2)^{1/2}/a$. Substituting this value in (3) and integrating from $-a$ to $+a$, we obtain the inertia moment of the elliptical section:

$$I_c = \frac{2}{3}\int_{-a}^{a} h^3 dx = \frac{2b^3}{3a^3}\int_{-a}^{a}\left[a^2 - x^2\right]^{3/2} dx = \frac{\pi a b^3}{4}. \tag{6}$$

At $a = b = r$, we derive the inertia moment of the circular section: $\pi r^4/4$, where r — radius of the circle.

Substituting value h corresponding to the ellipse in (4), we obtain the following distribution of shear stress in the section of the elliptical console:

$$\tau(x) = \lambda_e b^2 (1 - x^2 / a^2) E / L^3.$$

Figure 3 *b* shows distribution $\tau(x)$ along semi-axis $a = 2.5$ mm at $\lambda_e = 2$ mm, $E = 200$ GPa and $L = 50$ mm. When comparing it to distribution $\tau(x)$ in Figure 2 *b*, for a square, a significant influence of the geometry of the console section on the stress distribution is obvious. In the case of the elliptical section, there is no sharp peak on curve $\tau(x)$. Maximum voltage τ_{max} is observed along semi-axis b. Taking into account the requirement $\lambda_e = $ const, it can be said about a rapid growth of voltage τ_{max} with an increase in ratio b/a. When half-axis b is doubled, τ_{max} increases by 4 times (Fig. 3 *b*).

Mechanics

Triangle. Consider the section in the form of an isosceles triangle (Fig. 4). x-axis is directed along the altitude of the triangle (Fig. 4 a). At distance x from the base of the triangle, the half-length of the strip is equal to $h = b\,(a-x)/2a$.
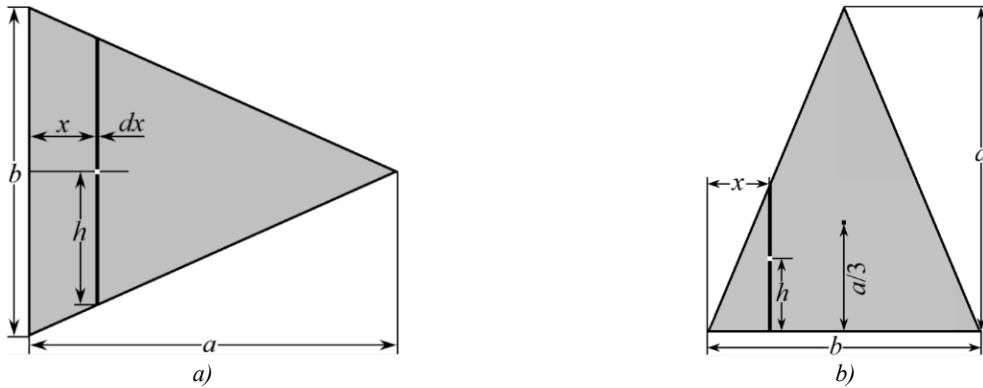
Fig. 4. Section diagram in the form of isosceles triangle:
a — x-axis, force is directed parallel to the base;
b — force is directed perpendicular to the base

Integrating expression (4) over x from 0 to a determines the following value of the inertia moment:

$$I_c = \frac{b^3}{12a^3}\int_0^a (a-x)^3 dx = \frac{b^3 a}{48}. \tag{7}$$

Consider the case when x-axis passes through the center of gravity and is parallel to the base of the triangle (Fig. 4 b).

The strip at distance x from the left corner of the triangle has half-length $h = x\sqrt{4a^2/b^2 - 1}/2$ (Fig. 4 b). The center of gravity of the strip is located at distance h from the base of the triangle (Fig. 4 b). Therefore, according to the Huygens–Steiner theorem for the cross section, the inertia moment of the strip relative to the base of the triangle is:

$$dI_c = \frac{2}{3}h^3 dx + 2h^3 dx = \frac{8}{3}\frac{a^3}{b^3}x^3 dx.$$

Integrating the resulting expression over variable x from $-b/2$ to $b/2$ determines the inertia moment of the triangle relative to the base:

$$I_x = a^3 b / 12. \tag{8}$$

The center of gravity of the triangle is located at distance $a/3$ from the base. According to the Huygens–Steiner theorem [13], the inertia moment of a triangle relative to its own center of gravity is less than (8) by:

$$I' = \left(\frac{a}{3}\right)^2 S = \frac{a^3 b}{18},$$

where $S = ab/2$ — area of triangle.

In this manner, the inertia moment of the triangle relative to its own center of gravity is equal to:

$$I_c = \frac{a^3 b}{12} - \frac{a^3 b}{18} = \frac{a^3 b}{36}. \tag{9}$$

The result obtained corresponds exactly to the tabular value of the inertia moment of the section relative to the axis through the center of gravity parallel to the base of the triangle.

Figure 5 shows the shear stress distributions in the triangular section at $\lambda_e = 2$ mm for cases where the deflection force is directed along the base (a) and along the altitude of the triangle (b).
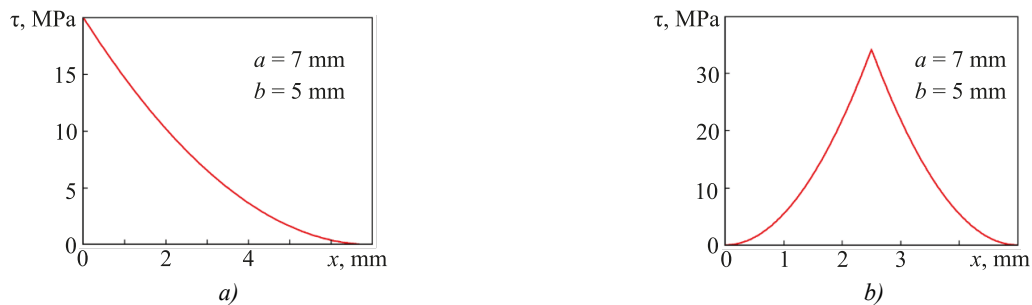
Fig. 5. Distributions τ in the triangular section:
a — force is directed along the base; b — force is directed along the altitude of the triangle

When the triangle is oriented as in Figure 4 *a*, voltage $\tau(x)$ decreases gradually from τ_{max} at the base to 0 at the apex (Fig. 5 *a*). With the orientation of the triangle as in Figure 4 *b*, distribution $\tau(x)$ (Fig. 5 *b*) is similar to the distribution for a square section when the force is oriented along the diagonal (Fig. 2 *b*).

Regular hexagon. Figure 6 shows two orientation of the hexagon relative to *x*-axis: parallel (*a*) and perpendicular (*b*) to its diagonal.

Fig. 6. Regular hexagon:
a — diagonal is perpendicular to the force vector;
b — diagonal is parallel to the force vector

The section of the hexagon in Figure 6 *a* consists of the following:
− rectangle with width *a* and height $a\sqrt{3}$,
− two isosceles triangles with apex *a*/2 and base $a\sqrt{3}$.

Let us find the inertia moments of the specified parts of the section by (2) for the rectangle and by (7) for triangles. For the rectangle in equation (2), $b = a\sqrt{3}$; therefore, its inertia moment is $I_{x1} = \sqrt{3}a^4/4$. For triangular parts in equation (7), the base is $b = a\sqrt{3}$, and the altitude is *a*/2. Consequently, the inertia moment of the hexagon is:

$$I_x = I_{x1} + I_{x2} = \sqrt{3}a^4\left(1/14 + 1/16\right) = 5\sqrt{3}a^4/16. \tag{10}$$

If the applied force is directed along the diagonal of the hexagon (Fig. 6 *b*), then the half-length of the strip is equal to $a/2 - x/\sqrt{3}$. Having made the appropriate substitutions in (4), we obtain:

$$I_c = \frac{2}{3}\int_{-a\sqrt{3}/2}^{a\sqrt{3}/2} (a - x/\sqrt{3})^3 dx = \frac{5\sqrt{3}a^4}{16}. \tag{11}$$

Comparing (10) and (11), we make sure that the rotation of the hexagon by 30° does not affect its inertia moment relative to *x*-axis.

Consider the case of the hexagon orientation as in Figure 6 *a*. At $\lambda = 2$ mm and $E = 200$ GPa in the range from $-a/2$ to $+a/2$, voltage $\tau(x)$ is constant and equal to $\tau_{max} = 15$ MPa (Fig. 7 *a*). Under the same conditions and orientation of the hexagon as in Figure 6 *b*, distribution $\tau(x)$ is similar to the distribution for a square section (Fig. 2 *b*). However, here, $\tau_{max} = 20$ MPa and $\tau_{min} = 5$ MPa (Fig. 7 *b*).
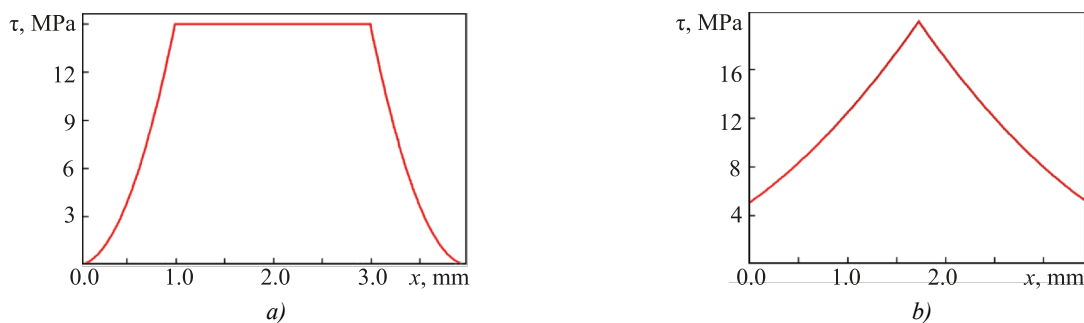
Fig. 7. Distribution $\tau(x)$ in the section of the regular hexagon:
a — diagonal is perpendicular to the force vector;
b — diagonal is parallel to the force vector

Examples of Simplified Calculation of the Inertia Moment of Complex Sections

Six-pointed star. Using the proposed method, we calculate the inertia moment of a non-standard section in the form of a regular 6-pointed star with side *a*. To determine the inertia moment relative to the minor diagonal of the star, we use the diagram in Figure 8 *a*. Let us highlight three zones in the diagram: zone I with width *a*/2, zone II for the rest of the half-figure, and the adjacent auxiliary zone III in the form of a triangle.

Mechanics

165
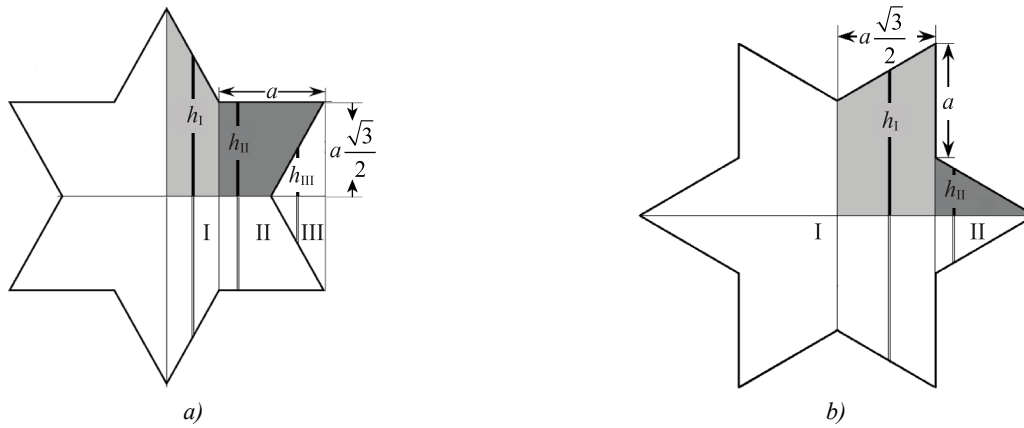
Fig. 8. On calculating the inertia moment of the six-pointed star relative to a — minor diagonal;
b — major diagonal

Half-length of the strip in zone I at distance x from the diagonal is $h_I = \sqrt{3}(a - x)$. Using expression (3), for two zones I in Figure 6 a, we obtain the inertia moment:

$$I_{xI} = 2\sqrt{3} \int_{a/2}^{a/2} (a - x)^3 dx = \frac{15 \cdot \sqrt{3}}{16} a^4.$$

The inertia moment of zone II is equal to the inertia moment of a rectangle with height $a\sqrt{3}$ and width a without the inertia moment of triangle III. The half-length of the strip in the rectangle is equal to $h_{II} = a\sqrt{3}/2$. From equation (3), we find the inertia moment of the rectangle:

$$I_{II+III} = \frac{\sqrt{3}}{4} a^4.$$

The half-length of the strip in the triangle is equal to $h_{III} = x\sqrt{3}$. According to (4), the inertia moment of the triangle is:

$$I_{III} = \frac{\sqrt{3}}{32} a^4.$$

Hence, the inertia moment of zone II is equal to:

$$I_{II} = I_{II+III} - I_{III} = \frac{7\sqrt{3}}{32} a^4.$$

The doubled sum of the inertia moments of zones I and II determine the inertia moment of the 6-pointed star:

$$I_{xI} = \frac{11 \cdot \sqrt{3}}{8} a^4. \tag{12}$$

To determine the inertia moment of the star relative to the major diagonal, we use the diagram in Figure 8 b, where two zones are highlighted. The half-length of the strip in zone I is $h_I = a + x/\sqrt{3}$, in zone II — $h_{II} = a/2 - x/\sqrt{3}$. From (3), the inertia moments of zones I ($I_{xI} = a^4 65\sqrt{3}/96$) and II ($I_{xII} = a^4\sqrt{3}/96$) are calculated. It is seen that the doubled sum of the inertia moments of zones I and II corresponds exactly to equation (12). Therefore, the inertia moment of the 6-pointed star relative to the major and minor diagonals is the same.

Figure 9 a shows the shear stress distribution in the section of the 6-pointed star corresponding to $\lambda = 2$ mm and the orientation of the external applied force according to Figure 8 a. Along the vertical axis of the star, the voltage takes on maximum value $\tau_{max} = 37.5$ MPa. With distance from the axis to the right, τ drops quickly to the level $\tau = 9.375$ MPa and remains constant in the range $2 \leq x \leq 4$ mm. Then, τ drops to zero. With distance away from the axis to the left, τ changes similarly.
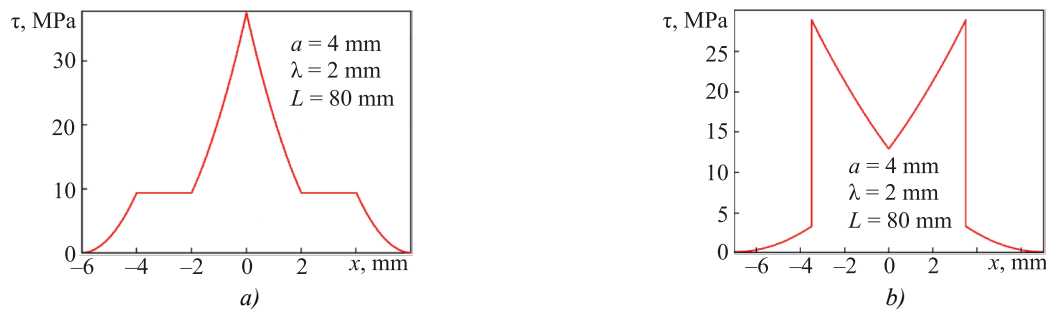
Fig. 9. Distributions τ in the hex-shaped section: a — force is directed along the major diagonal;
b — force is directed along the minor diagonal

When the star rotates by 30°, voltage distribution τ changes significantly, acquiring the outlines of a dovetail (Fig. 9 *b*). Two peaks are observed with value $\tau_{max} = 28.12$ MPa. The distribution pattern is symmetrical. However, with distance from the axis of symmetry, the voltage first increases from 12.5 to 28.12 MPa, and then drops to 3.125 MPa. In this regard, two peaks are observed on dependence τ(*x*). Further on, the voltage decreases rapidly to zero.

Figured cross. Consider a solution for the inertia moment of a non-standard section in the form of a figured cross (Fig. 10), each side of which is the fourth part of the circle of radius *R*. The distance between the apices of the figure is $R\sqrt{2}$. We first find the inertia moment of the cross relative to the major diagonal (Fig. 10 *a*).
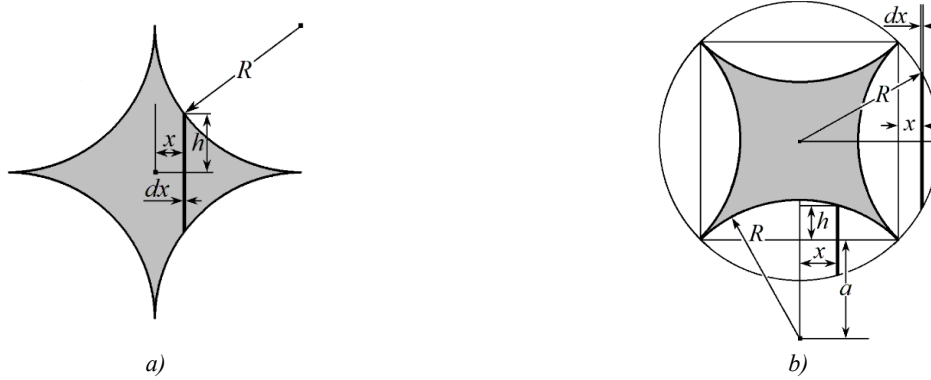
Fig. 10. Figured cross: *a* — force is directed along the diagonal of the cross;
b — force is directed at an angle of 45° to the diagonal of the cross

Half-length of strip *h* in Figure 10 *a* is equal to:

$$h = R - \sqrt{R^2 - (R-x)^2}.$$

Taking into account the symmetry and using equation (3), we obtain the following value of the inertia moment of the section of the figured cross:

$$I_x = \frac{4}{3}\int_0^R \left[R - \sqrt{x(2R-x)} \right]^3 dx = [4 - 5\pi/4]R^4. \tag{13}$$

We determine the inertia moment of the cross when it is rotated by 45° relative to *x*-axis (Fig. 10 *b*).

Figured cross fits into the circle of radius *R*. Figure 10 *b* shows that there are four figures in the form of an oval with sharp corners around the cross. To determine the inertia moment of the cross, it is sufficient to subtract the inertia moments of the four ovals from the inertia moment of the circle.

It follows from (6) that the inertia moment of the circle is equal to:

$$I_{x0} = \pi R^4 / 4.$$

We determine the inertia moments of the ovals relative to the center of gravity of the cross.

The inertia moment of the oval on the right is equal to the inertia moment of the oval on the left. Half-height of the strip at the oval on the left is:

$$h_1 = \sqrt{R^2 - (R-x)^2}.$$

We take into account equation (3), as well as the symmetry of these parts and their location. By integrating from 0 to $R - R/\sqrt{2}$, the following value of the inertia moment of these two parts is obtained:

$$I_{x1} = \frac{8R^3}{3}\int_0^{R(1-1/\sqrt{2})} \left[\sqrt{1-(1-x/R)^2} \right]^3 dx = \frac{R^4}{3}\left[\frac{3\pi}{4} - 2 \right]. \tag{14}$$

The centers of gravity of the ovals above and below the circle are located at distance $a = R/\sqrt{2}$ from the center of gravity of the whole figure. The area of these two parts is equal to $S = R^2(\pi - 2)$.

By (4), we calculate the moment of inertia of this pair:

$$I_{x2} = a^2 S = R^4 [\pi/2 - 1].$$

Value *h* in (3), according to Figure 10 *b*, (oval at the bottom of the circle) is equal to $h = \sqrt{2a^2 - x^2} - a$. Therefore, for a pair of ovals at the top and bottom of the circle, the inertia moment relative to their own centers of gravity can be recorded as:

$$I_{x3} = \frac{8}{3}R^3 \int_0^{R/\sqrt{2}} \left[\sqrt{1-(x/R)^2} - 1/\sqrt{2} \right]^3 dx = R^4[3\pi/4 - 7/3]. \tag{15}$$

Mechanics

We determine the resulting inertia moment of the figured cross. To do this, we subtract the inertia moments of the four ovals from inertia moment (13) of the circle:

$$I_{x0} - I_{x1} - I_{x2} - 2I_{x3} = \left[4 - 5\pi/4\right] R^4.$$

Comparing the result obtained to result (13), we can see that the inertia moment of this cruciform section of the console does not change when *x*-axis is rotated by 45°.

Figure 11 *a* shows the distribution of shear stress in the cross section of the figured cross, corresponding to λ = 2 mm, and the action of an external applied force along the axis of the cross (Fig. 10 *a*). A sharp voltage peak is observed on the vertical axis of the cross, where τ_{max} = 80.0 MPa.

a)   *b)*
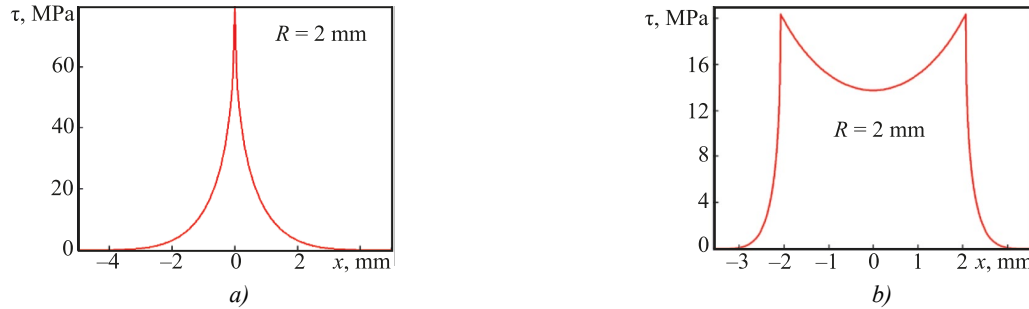
Fig. 11. Distributions τ in the section of the figured cross:
a — force is directed along the diagonal of the cross,
b — force is directed at an angle of 45° to the diagonal of the cross

When the cross is rotated relative to the applied force by 45°, voltage distribution τ changes significantly. As the axis of symmetry deviates, voltage first gradually increases from τ = 13.73 MPa to τ_{max} = 20.32 MPa. Then, voltage τ drops sharply to zero. Therefore, two symmetrical peaks (Fig. 11 *b*) are observed in distribution τ at a distance of 2 mm from the axis of symmetry.

Discussion and Conclusion. The proposed simplified calculation method provides for the rapid determination of the inertia moments of complex cross sections of the console. In this case, the shear stress field in the sample section corresponding to the action of an external applied force is uniquely determined. In addition, it is shown that the stress distribution in the section qualitatively and quantitatively depends on the orientation of the section relative to the direction of the external applied force.

To validate the method, the inertia moments were calculated not only for known sections of simple geometry (which showed the absolute identity of the calculated and published results in the literature), but also for two new complex sections in the form of a regular six-pointed star and a figured cross. It is shown that the rigidity of the console does not change when an external force applied perpendicular to the axis of symmetry is rotated by 30° for a section in the form of a 6-pointed star, and by 45° — for a square and a figured cross. The method and the solutions obtained can be used by engineers and mechanics in modeling and calculating strength and stiffness of rod structural elements.

References

1. Ching Francis DK, Onouye B, Zuberbuhler D. *Building Structures Illustrated: Patterns, Systems, and Design*. 2nd ed. Hoboken, NJ: John Wiley & Sons; 2014. 352 p. URL: https://zlib.pub/book/building-structures-illustrated-1rgfde22jln8 (accessed: 22.02.2024).

2. Hallebrand E, Jakobsson W. *Structural Design of High-Rise Buildings*. Lund: Media-Tryck LU; 2016. 142 p.

3. Amany D, Pasini A. Material and Shape Selection for Stiff Beams under Non-Uniform Flexure. *Materials and Design*. 2009;30(4):1110–1117. http://doi.org/10,1016/j.matdes,2008,06,029

4. Pilkey WD. *Formulas for Stress, Strain, and Structural Matrices*. Hoboken, NJ: John Wiley & Sons; 2005. 1536 p.

5. Gaidzhurov PP, Saveleva NA. Application of the Double Approximation Method for Constructing Stiffness Matrices of Volumetric Finite Elements. *Advanced Engineering Research (Rostov-on-Don)*. 2023;23(4):365–375. https://doi.org/10.23947/2687-1653-2023-23-4-365-375

6. Murakami Y. *Theory of Elasticity and Stress Concentration*. Hoboken, NJ: John Wiley & Sons; 2016. 480 p.

7. Bechtel FK. Estimating Local Compliance in a Beam from Bending Measurements. Part I. Computing "Span function". *Wood and Fiber Science*. 2007;9(2):250–259.

8. Bhattacharjya RK. *Engineering Mechanics*. New Delhi: Oxford University Press; 2009. 832 p.

9. Damkilde L. *Stress and Stiffness Analysis of Beam Sections*. Copenhagen: Technical University of Denmark; 2000. 36 p.

10. Zhernakov VS. *Material Resistance — Mechanics of Materials and Structures*. UFA: Ufa State Aviation Technical University; 2000. 36 p. (In Russ.).

11. Kleppner D, Kolenkow R. *An Introduction to Mechanics*. 2nd ed. Cambridge: Cambridge University Press; 2014. 566 p.

12. Pan'zhenskii VI, Surina OP, Sorokina MV. *Plane Analytic Geometry*. Penza: Penza State University; 2020. 120 p. (In Russ.).

13. Brown RG. *Introductory Physics I. Elementary Mechanics*. Durham: Duke University Physics Department; 2013. 661 p.

About the Author:

Evgeny E. Deryugin, Dr.Sci. (Phys.-Math.), Professor*,* Leading Researcher of the Laboratory of Physical Mesomechanics and Non-Destructive Testing Methods, Institute of Strength Physics and Material Science, Siberian Branch of Russian Academy of Sciences (2/4, Akademicheskii Ave., Tomsk, 634055, Russian Federation), SPIN-code: 6587-3002, ORCID, ScopusID, dee@ispms.tsc.ru

Об авторе:

Евгений Евгеньевич Дерюгин, доктор физико-математических наук, профессор лаборатории физической мезомеханики и неразрушающих методов контроля института физики прочности и материаловедения Сибирского Отделения Российской академии наук, (534055, Российская Федерация, г. Томск, Академический пр., 2/4), SPIN-код: 6587-3002, ORCID, ScopusID, dee@ispms.tsc.ru

Conflict of Interest Statement: **the author declares no conflict of interest.**

Конфликт интересов: **автор заявляет об отсутствии конфликта интересов.**

All author has read and approved the final manuscript.

Автор прочитал и одобрил окончательный вариант рукописи.

Mechanics

MECHANICS
МЕХАНИКА

On the Method for Solving the Problem of Ice Cover Deformation under an Arbitrary Moving Load

Alexander V. Galaburdin (iD)

Don State Technical University, Rostov-on-Don, Russian Federation

✉ 5339850@mail.ru

EDN: ZASIUO

Abstract

Introduction. The development of the polar areas of the World Ocean and the need to solve various problems associated with a large number of freezing inland water bodies issue new challenges for science. These challenges include the problem of studying the behavior of ice cover when exposed to various types of loads. Of great interest is the consideration of problems about the action of a moving load on the ice cover. A moving load simulates the effect of moving vehicles on ice. However, in papers devoted to the above problems, cases of load movement along a straight-line trajectory are considered. The objective of this research is to develop a method for studying the behavior of ice cover under the action of a load moving arbitrarily.

Materials and Methods. The article proposes a method for solving the problem of the action of a force moving along an arbitrary trajectory on the ice cover of a reservoir of finite depth. The problem amounts to solving a system of two differential equations. The first of them models the behavior of the ice cover, and it is the equation of vibrations of a viscoelastic plate. The second equation simulates the behavior of fluid in a state of potential flow, and it is Laplace's equation. To solve the system of differential equations, integral transformations in time, space and variables were used. The resulting solution was expressed through an iterated integral, which was calculated using numerical methods.

Results. The development and implementation of the method resulted in solving the problem of the movement of a concentrated force along an ice cover according to an arbitrary law. At the same time, studies were carried out on the behavior of displacements and stresses in the ice cover depending on the speed and acceleration of the movement of the vertical load, on the depth of the reservoir, and on the viscoelastic properties of ice. In addition, the distribution of the velocity vector of fluid particles along the depth of the reservoir was calculated.

Discussion and Conclusion. The proposed method is very effective for solving problems of moving loads acting on the ice cover of a reservoir of finite depth. It provides solving problems about the action of a load moving along an ice cover along a complex trajectory. The results obtained can be used to calculate the stress and displacement of the ice cover during the laying of ice roads or the construction of airfields on the ice.

Keywords: infinite ice cover, moving load, arbitrary trajectory, variable speed

Разработка метода решения задачи деформации ледяного покрова под действием произвольно движущейся нагрузки

А.В. Галабурдин(iD)

Донской государственный технический университет, г. Ростов-на-Дону, Российская Федерация

✉ 5339850@mail.ru

Аннотация

Введение. Освоение полярных районов Мирового океана, необходимость решения различных задач, связанных с наличием большого числа замерзающих внутренних водоемов, ставят перед наукой новые проблемы. К их числу относится проблема изучения поведения ледяного покрова под воздействием на него различного вида нагрузок. Большой интерес представляет рассмотрение задач о действии на ледяной покров подвижной нагрузки. Подвижная нагрузка моделирует действие на лед движущихся транспортных средств. Однако в работах, посвященных вышеуказанным задачам, рассматриваются случаи движения нагрузки по прямолинейной траектории. Целью данной работы является разработка метода исследования поведения ледяного покрова под действием нагрузки, перемещающейся произвольным образом.

Материалы и методы. В статье предложен метод решения задачи о действии на ледяной покров водоема конечной глубины движущейся по произвольной траектории силы. Задача сводится к решению системы двух дифференциальных уравнений. Первое из них моделирует поведение ледяного покрова и является уравнением колебаний вязкоупругой пластины. Второе — моделирует поведение жидкости, находящейся в состоянии потенциального течения, и является уравнением Лапласа. Для решения системы дифференциальных уравнений применялись интегральные преобразования по временной и пространственным переменным. Полученное в результате решение выражалось через повторный интеграл, для вычисления которого применялись численные методы.

Результаты исследования. В результате реализации предложенного метода получено решение задачи о движении сосредоточенной силы по ледяному покрову по произвольному закону. При этом произведены исследования характера поведения перемещений и напряжений в ледяном покрове в зависимости от скорости и ускорения движения вертикальной нагрузки, глубины водоема и вязкоупругих свойств льда. Кроме того, рассчитано распределение вектора скорости частиц жидкости по глубине водоема.

Обсуждение и заключение. Предложенный метод является весьма эффективным для решения задач о подвижных нагрузках, действующих на ледяной покров водоема конечной глубины. Он позволяет решать задачи о действии нагрузки, движущейся по ледяному покрову по сложной траектории. Полученные результаты могут быть использованы для расчета напряжения и перемещений ледового покрова при прокладке ледовых дорог или строительстве аэродромов на льду.

Ключевые слова: бесконечный ледяной покров, движущаяся нагрузка, произвольная траектория, переменная скорость

Introduction. The development of the polar areas of the World Ocean and a large number of freezing inland reservoirs drive the need to study the fields of displacement and stresses of the ice cover caused by the action of various types of loads. Numerous papers by domestic and foreign scientists are devoted to solving these problems. Previously, it has been found that the mechanical properties of ice depend on its temperature and water salinity. Much attention was paid to the development of numerical ice models that accurately reflected the interaction of ice and ideal incompressible fluid. In [1, 2], the smoothed particle hydrodynamics was used for this purpose, in [3, 4] — the method of discrete elements. In [5], ice was modeled by an elastic plate lying on the surface of a stratified fluid. Models that allow cracks were considered in [6, 7]. Models of ice strengthened with reinforcing elements were presented in [8, 9].

At this, in some papers, an ice cover is considered as an elastic plate lying on the surface of a reservoir [10, 11]. At the same time, in [12], on the basis of the conducted research, it is concluded that in some cases, the properties of ice are best described by the Kelvin-Voigt rheological model with one parameter (damping time). Therefore, numerous researchers use a viscoelastic plate when modeling the ice cover [13]. In [14], nonlinear models were used to describe the properties of ice.

In some articles, the effect of a moving load on the ice cover was considered. In [15], the impact of a mobile load on the ice cover in a frozen channel was studied. In [16], the action of a load with an impulsive movement on the ice cover was described. Paper [17] is devoted to the study of the load moving along a frozen riverbed. Here, the rectilinear motion of the load was investigated [18]. However, in real conditions, it is often needed to deal with a load moving in a more complex way. Therefore, the objective of this work is to develop a method for solving problems about the action of a load moving over an ice cover along a complex trajectory. This will provide for a more accurate investigation of the effect of vehicles moving in a complex way on ice.

This work is a continuation of research related to the problems about the effect of a moving load on various objects, whose results are presented in papers [19, 20].

Materials and Methods. Setting the task. A reservoir of finite depth with an infinite ice cover (an infinite plate), which is subject to the action of a vertical force moving in an arbitrary way — impulsively, is considered. It is assumed that the reservoir fluid is incompressible and executes irrotational motion.

The problem is reduced to a system of differential equations [15]:

$$\left(1+\tau_0\partial_t\right)\Delta_0^2 W + c^{-2}\partial_t^2 W + kW + b\partial_t F\big|_{z=0} = \frac{Q(x,y,t)}{D},$$

$$\Delta F = 0,$$

where $W(x,y,t)$ — ice cover deflection; E and μ — Young's modulus and Poisson's ratio of ice, respectively; $D = Eh^3/12(1-\mu^2)$ — cylindrical bending stiffness; h — ice cover thickness; τ_o — strain relaxation time; $\Delta_o^2 = (\partial_x^2+\partial_y^2)^2$; $\Delta = \partial_x^2+\partial_y^2+\partial_z^2$; $\rho_л$ and $\rho_в$ — density of ice and water, respectively; $c^{-2} = \rho_л h/D$; $k = \rho_в g/D$; $b = \rho_в/D$; $Q(x,y,t)$ — load acting on the ice surface; $F(x,y,z,t)$ — speed potential.

Under boundary conditions at $z = 0$ (ice-water boundary):

$$\partial_t W = \partial_z F.$$

At the bottom of the reservoir at $z = -H$:

$$\partial_z F = 0.$$

In addition, it was assumed that the ice cover and the fluid in the reservoir were resting at the start time. The load was a concentrated unit force (one Newton) $Q(x,y,t)$, which moved arbitrarily along open free-form curve γ. It was assumed that the displacement of the force was given in the form $Q = Q(s(t))$, where s — arc coordinate measured from some fixed point of trajectory γ. The trajectory of movement was set parametrically in the form $\begin{cases} x = x_0(t) \\ y = y_0(t) \end{cases}$, where t — time.

The moving load was approximated by the expression:

$$Q(x,y,t) = \varepsilon^2 \exp\left(-\varepsilon^2\left(\left(x-x_0(t)\right)^2+\left(y-y_0(t)\right)^2\right)\right)\Big/\pi,$$

where ε — numeric parameter.

After applying the integral Fourier transform with respect to variables x and y, the integral Laplace transform with respect to t, formulas for calculating unknown functions W and F were obtained:

$$W(x,y,t) = \frac{1}{2\pi D}\int_0^t\int_0^\infty p^2 e^{-p^2/4\varepsilon^2} J_0\left(pR(t-\tau)\right)\frac{1}{\gamma}\left[e^{-(a-d)\tau}-e^{-(a+d)\tau}\right]dpd\tau,$$

$$F(x,y,z,t) = \frac{1}{2\pi D}\int_0^t\int_0^\infty p^2 e^{-p^2/4\varepsilon^2} J_0\left(pR(t-\tau)\right)\frac{ch\left(p(z+H)\right)}{sh(pH)},$$

$$W(x,y,t) = \frac{1}{2\pi D}\int_0^t\int_0^\infty p^2 e^{-p^2/4\varepsilon^2} J_0\left(pR(t-\tau)\right)\frac{1}{\gamma}\left[e^{-(a-d)\tau}-e^{-(a+d)\tau}\right]dpd\tau,$$

$$\left[(a+d)e^{-(a+d)\tau}-(a-d)e^{-(a-d)\tau}\right]dpd\tau,$$

$$R^2(\tau) = \delta^2 + \beta^2, \delta = x_0(\tau)-x, \beta = y_0(\tau)-y,$$

$$\gamma = \left[\tau_0^2 p^{10} - 4\left(c^{-2}p^2 + bpcth(pH)\right)\left(p^4 + k\right)\right]^{1/2}, \; a = \frac{\tau_0 p^5}{2\left(c^{-2}p + bcth(pH)\right)},$$

$$d = \frac{\gamma}{2\left(c^{-2}p + bcth(pH)\right)}.$$

Using the known relations from the theory of thin plates and the theory of the potential ideal flow, it is possible to obtain relations for calculating displacements and stresses in the ice cover, as well as the velocity vector component of fluid particles.

When calculating the improper integral through numerical methods, the approximate relationship $\int_0^\infty f(p)dp \approx \int_0^A f(p)dp$ was used, in which value A was chosen so large, that the error estimate $\left|\int_A^\infty f(p)dp\right|$ did not exceed the set value.

Thus, for the amount of ice deflection

$$W(x,y,t) = \frac{1}{2\pi D}\int_0^t\int_0^\infty U_0(\tau,p)dpd\tau = \frac{1}{2\pi D}\int_0^t\int_0^A U_0(\tau,p)dpd\tau + \frac{1}{2\pi D}\int_0^t\int_A^\infty U_0(\tau,p)dpd\tau,$$

this estimate has the form:

$$\left|\frac{1}{2\pi D}\int_0^t\int_A^\infty U_0(\tau,p)dpd\tau\right| \le \frac{2A\varepsilon^2}{\pi D\gamma(A)}e^{A^2/4\varepsilon^2},$$

$$\gamma(A) = \left[\tau_0^2 A^{10} - 4\left(c^{-2}A^2 + bActh(AH)\right)\left(A^4 + k\right)\right]^{1/2}.$$

Similar estimates can be obtained for other calculated quantities. These estimates were used to determine value A.

In the calculations carried out, value A was chosen such, that the estimate $\dfrac{2A\varepsilon^2}{\pi D\gamma(A)}e^{A^2/4\varepsilon^2}$ did not exceed

$\left|\dfrac{1}{2\pi D}\int_0^t\int_A^\infty U_0(\tau,p)dpd\tau\right|$ 0.001.

When calculating the repeated integral, Simpson's quadrature formula (for variable τ) and Chebyshev quadrature formula with equal weights for two nodes (for variable *p*) were used. The other values were calculated in the same way.

Research Results. A method has been developed for solving problems on the action of a load moving along the ice cover of a reservoir filled with ideal fluid along a complex trajectory with variable speed. Using this method, calculations were carried out that showed the degree of impact of various parameters on the deformation of the ice cover.

The described method does not impose restrictions on the shape of the trajectory of the concentrated force. In the calculations, a special case of a trajectory consisting of arcs of circles was considered (Fig. 1). The red dot indicates the position of the concentrated force at the time under consideration and the direction of movement of the force.
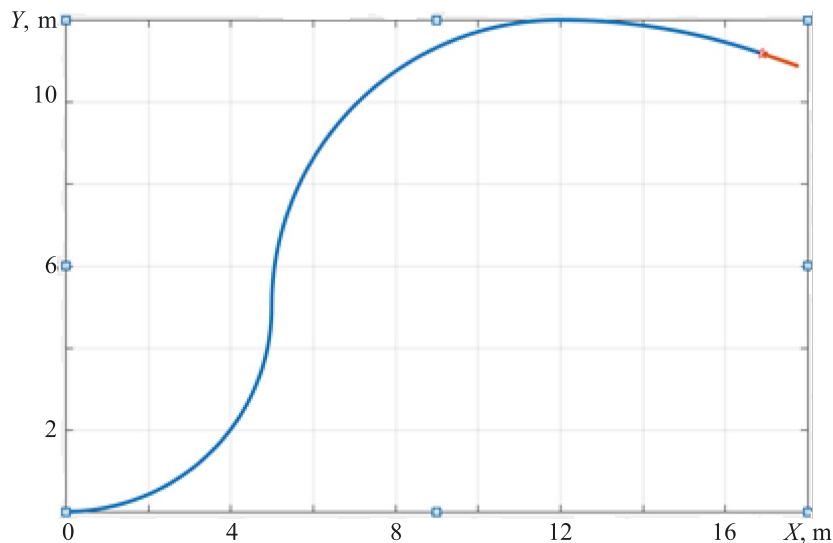
Fig. 1. Trajectory of concentrated force

Mechanics

The following parameter values were taken into account in the calculations: ice cover thickness $h = 0.25$ m, Young's modulus $E = 500,000,000$ H/m^2, Poisson's ratio of ice $\mu = 1/3$, ice density $\rho = 900$ kg/m^3, fluid density $\rho = 1,000$ kg/m^3, $\varepsilon = 5$. The calculation results are presented below.

Figure 2 shows the change in the deflection of the ice cover at speed of force $v = 2.5$ m/s, tangential acceleration $w_t = 1$ m/s^2, reservoir depth $H = 25$ m, and relaxation time $\tau_o = 1$s.

The law of force motion along the trajectory was taken as:

$$s = a_1 t^3 + a_2 t^2 + a_3 t.$$

Coefficients a_1, a_2, a_3 were selected in such a way that the force, being at the same point of the trajectory, had the required speed and tangential acceleration.
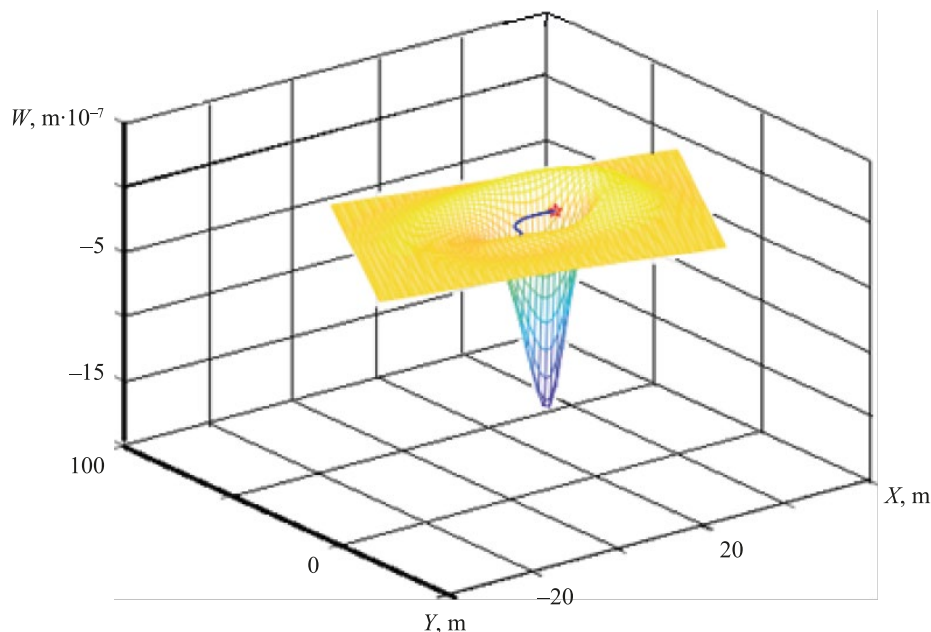
Fig. 2. Change in ice cover deflection

At other values of these parameters, the qualitative nature of the distribution of ice cover deflections remained almost unchanged.
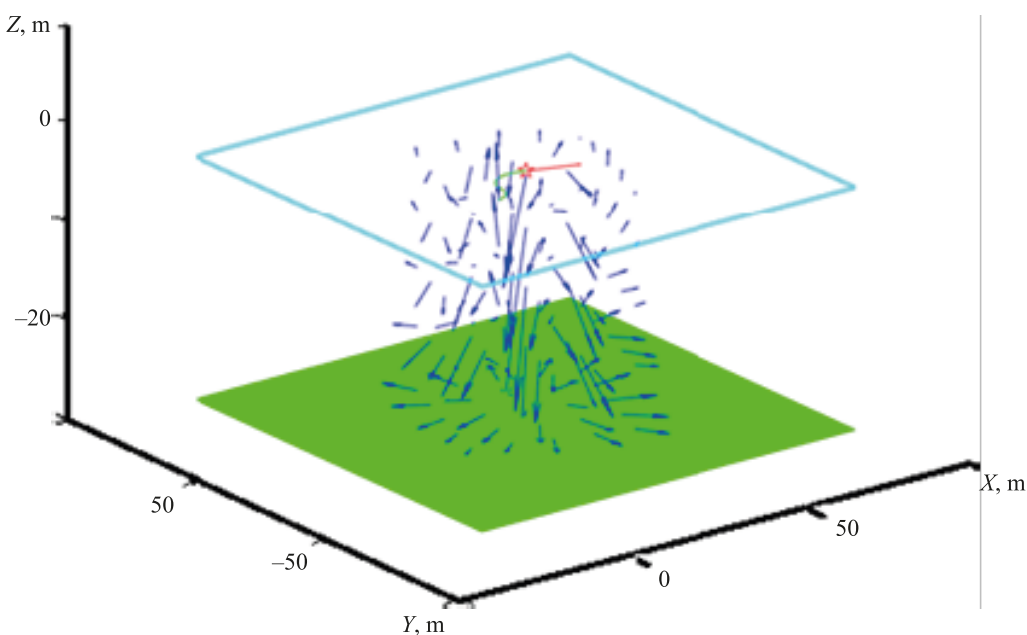
Fig. 3. Fluid motion caused by action of moving load on the ice cover

The fluid motion caused by the action of a moving load at the same values of velocity, tangential acceleration of the load movement, relaxation time, and depth of the reservoir is shown in Figure 3 (the distribution of the velocity vector of fluid particles is shown).
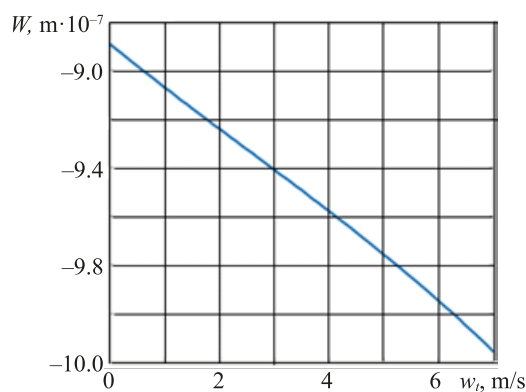
a)
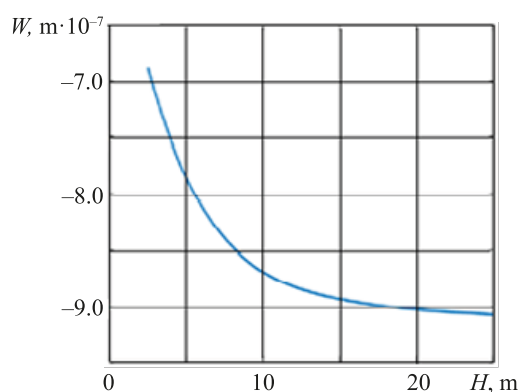
b)

Fig. 4. Change in amount of maximum deflection of ice cover depending on:
a — tangential acceleration rate; *b* — depth of reservoir

The effect of the tangential acceleration of the force movement on the maximum deflection of the ice cover is shown in Figure 4 *a*. In this case, the force speed was equal to $v = 17.5$ m/s, and the relaxation time $\tau_o = 1$ s.

Figure 4 *b* shows a graph of the dependence of the maximum deflection of the ice cover W on the reservoir depth H. Here, the speed of the load movement was $v = 17.5$ m/s, tangential acceleration $w_t = 1$ m/s², and relaxation time $\tau_o = 1$s.
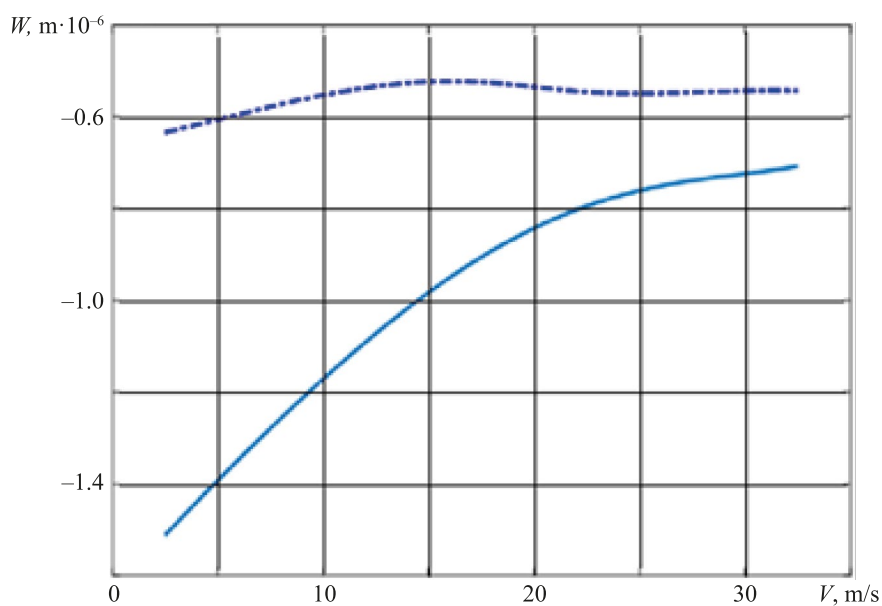
Fig. 5. Change in maximum deflection of ice cover
depending on force speed

The dependence of the maximum deflection of the ice cover on the force speed is graphically shown in Figure 5. The depth of the reservoir was assumed to be 25 m, and the tangential acceleration — $w_t = 1$ m/s². The solid line shows the dependence corresponding to the relaxation time $\tau_o = 1$ s, the dotted line corresponds to the relaxation time $\tau_o = 10$ s.

Mechanics

175

Discussion and Conclusion. The influence of the reservoir depth on the maximum deflection of the ice was studied. A picture of the deflection of the ice cover was obtained due to the action of a concentrated force moving along a complex trajectory with variable speed. Calculations showed that with increasing depth of the reservoir, the maximum deflection of the ice cover decreased (Fig. 2). At the same time, a noticeable dependence of the deflection of the ice cover on the depth of the reservoir H occurred only for H≤25 m. At great depths, the amount of the maximum deflections stabilized near a certain constant value and practically did not change. Thus, if H>25 m, then the depth of reservoirs can be considered infinite when calculating.

An increase in tangential acceleration caused an increase in the deflection of the ice cover. Moreover, the dependence of deflection on tangential acceleration was very close to the linear dependence (Fig. 4).

At low relaxation times τ_o, the speed of the load movement affected significantly the amount of ice deflection. At large times, the impact of the load movement speed on the deflection of the ice cover was noticeably reduced (Fig. 5).

To study the state of the reservoir fluid, the distribution of the velocity vector of the fluid particles due to the action of the moving force on the ice was determined (Fig. 3).

The developed method of solving problems and the results obtained with its help can be used in the construction of ice roads, design and construction of runways on ice.

References

1. Ningbo Zhang, Xing Zheng, Qingwei Ma, Zhenhong Hu. A Numerical Study on Ice Failure Process and Ice-Ship Interactions by Smoothed Particle Hydrodynamics. *International Journal of Naval Architecture and Ocean Engineering.* 2019;11(2):796–808. https://doi.org/10.1016/j.ijnaoe.2019.02.008

2. Wenxiao Pan, Tartakovsky AM, Monaghan JJ. A Smoothed-Particle Hydrodynamics Model for Ice-Sheet and Ice-Shelf Dynamics. *Journal of Glaciology*. 2012;58(208):216–222. https://doi.org/10.3189/2012JoG11J084

3. Shunying Ji. Discrete Element Modeling of Ice Loads on Ship and Offshore Structures. In: *Proceedings of the 7th International Conference on Discrete Element Methods.* Singapore: Springer; 2017. P 45–54. http://doi.org/10.1007/978-981-10-1926-5_6

4. Hisette Q, Alekseev A, Seidel J. Discrete Element Simulation of Ship Breaking Through Ice Ridges. In: *Proceedings of the 27th International Ocean and Polar Engineering Conference. International Society of Offshore and Polar Engineers*. Cupertino, CA: ISOPE; 2017. P. 1–15.

5. Tsvetkov DO. Small Motions of an Ideal Stratified Fluid Partially Covered with Elastic Ice. *Bulletin of Udmurt University. Mathematics. Mechanics. Computer Science.* 2018;28(3):328–347. https://doi.org/10.20537/vm180305

6. Wenjun Lu, Raed Lubbad, Sveinung Løset. Out-of-Plane Failure of an Ice Floe: Radial-Crack-Initiation-Controlled Fracture. *Cold Regions Science and Technology*. 2015;119:183−203. https://doi.org/10.1016%2Fj.coldregions.2015.08.009

7. Renshaw CE, Schulson EM, Sigward SJG. Experimental Observation of the Onset of Fracture Percolation in Columnar Ice. *Geophysical Research Letters.* 2017;44(4):1795−1802. https://doi.org/10.1002/2016GL071919

8. Yakimenko OV, Sirotyuk VV. Reinforcement of Ice Crossings. *Earth's Cryosphere.* 2014;18(1):88−91.

9. Kozin VM, Vasilyev AS, Zemlyak VL, Ipatov KI. Research of the Limiting State of Ice Cover under Conditions of Pure Bending with Reinforcement by Reinforcing Elements. *Tomsk State University Journal of Mathematics and Mechanics.* 2019;(61):61–69.

10. Bukatov AE, Bukatov AA, Zharkov VV, Zav'yalov DD. *Propagation of Surface Waves in Ice Conditions*. Monograph. Sevastopol: Marine Hydrophysical Institute; 2019. 204 p. (In Russ.)

11. Tkacheva LA. Behavior of Semi-Infinite Ice Cover under Periodic Dynamic Impact. *Journal of Applied Mechanics and Technical Physics.* 2017;58(4):82–94.

12. Tabata T. Studies on Visco-Elastic Properties of Sea Ice. In: *Proc. Conf. Arctic Sea Ice.* Washington, DC: US National Academy of Sciences; 1958. P. 139–147.

13. Zemlyak VI, Vasilyev AS, Zhukov DS. Determination of the Stress-Strain State of the Ice Cover with Surface Reinforcement under the Influence of Static and Dynamic Loads. *The Eurasian Scientific Journal.* 2022;14(2):51–60.

14. Guyenne P, Părău EI. Computations of Fully Nonlinear Hydroelastic Solitary Waves on Deep Water. *Journal of Fluid Mechanics.* 2012;713:307–329. https://doi.org/10.1017/jfm.2012.458

15. Shishmarev KA, Khabakhpasheva TI. Unsteady Deflection of Ice Cover in a Frozen Channel under a Moving Load. *Computational Technologies.* 2019;24(2);111–128.

16. Wang K, Hosking RJ, Milinazzo F. Time-Dependent Response of a Floating Viscoelastic Plate to an Impulsively Started Moving Load. *Journal of Fluid Mechanics.*2004;521:295–317. https://doi.org/10.1017/S002211200400179X

17. Shishmarev K, Khabakhpasheva T, Korobkin A. The Response of Ice Cover to a Load Moving along a Frozen Channel. *Applied Ocean Research.* 2016;59:313–326. http://doi.org/10.1016/j.apor.2016.06.008

18. Sturova IV. Motion of an External Load over a Semi-Infinite Ice Sheet in the Subcritical Regime. *Fluid Dynamics.* 2018;53(1):51–60.

19. Galaburdin AV. Infinite Plate Loaded with Normal Force Moving along a Complex Path. *Advanced Engineering Research (Rostov-on-Don).* 2020;20(4):370–381. https://doi.org/10.23947/2687-1653-2020-20-4-370-381

20. Galaburdin AV. Method for Solving the Problem of Load Movement over the Ice Cover of a Reservoir along a Complex Trajectory. *Advanced Engineering Research (Rostov-on-Don)*. 2023;23(1):34–40. https://doi.org/10.23947/2687-1653-2023-23-1-34-40

About the Author:

Alexander V. Galaburdin, Cand.Sci. (Phys.-Math.), Associate Professor of the Mathematics and Informatics Department, Don State Technical University (1, Gagarin Sq., Rostov-on-Don, 344003, Russian Federation), ORCID, Galaburdin@mail.ru

Об авторе:

Александр Васильевич Галабурдин, кандидат физико-математических наук, доцент кафедры математики и информатики Донского государственного технического университета (344003, Российская Федерация, г. Ростов-на-Дону, пл. Гагарина, 1), ORCID, Galaburdin@mail.ru

MACHINE BUILDING AND MACHINE SCIENCE
МАШИНОСТРОЕНИЕ И МАШИНОВЕДЕНИЕ

Check for updates

Original Theoretical Research

Implementation of a Digital Model of Thermal Characteristics Based on the Temperature Field

Vladimir V. Pozevalkin [ID] ✉, Alexander N. Polyakov [ID]
Orenburg State University, Orenburg, Russian Federation
✉ pozevalkinvv@mail.ru

EDN: EYQXQZ

Abstract

Introduction. Computer modeling allows engineers to make valid design decisions by accurately assessing the thermal characteristics of design objects. The implementation of digital twin technology in the process of designing technical facilities is the current direction of scientific research and development. To do this, it is necessary to develop computer models whose accuracy meets the requirements for digital twins. However, the scientific literature does not widely present the results of research aimed at implementing digital twin technology in the design process. The general issues related to the use of digital twins in various industries are mainly considered. Therefore, the objective of this study was the development of a digital model and a comparative analysis of the accuracy of calculations of thermal characteristics of the design object.

Materials and Methods. The main tool for conducting the research was the methodology proposed by the authors for developing a computer model of thermal characteristics for the implementation of digital twin technology. The numerical solution was implemented through constructing a thermal model for calculating the temperature field based on the finite element method in the ANSYS engineering analysis system from ANSYS, Inc. (USA). For the analytical solution, a computer model of thermal characteristics developed on the basis of the state-space method, implemented in the ANSYS Twin Builder module, was used. The state-space model was matched to the behavior of the original thermal model through approximating the transfer function to the stepwise response of the thermal load using the time domain vector approximation method. Verification of the constructed analytical model was carried out in the engineering calculation system MATLAB from the MathWorks company (USA). The research was carried out for a 400V machine model manufactured by NPO "Stankostroenie" LLC, Sterlitamak (Russia).

Results. The developed digital model makes it possible to calculate the thermal characteristics of the design object with high accuracy. The results of the comparative analysis showed a high degree of correspondence between the values of thermal characteristics obtained using the proposed digital model and the results of numerical simulation. The maximum error in calculating thermal characteristics did not exceed 0.1ºC.

Discussion and Conclusion. Computer modeling that combines numerical calculation methods and a scientific approach based on digital twin technology, provides obtaining the result as close as possible to the results of experiments. The digital model proposed in the study is an effective solution, since it provides performing calculations to evaluate thermal characteristics in real time, which is one of the most important requirements for the implementation of digital twin technology.

Keywords: digital twin, complex technical object, computer modeling, computer-aided design, temperature field, thermal characteristics

Оригинальное теоретическое исследование

Реализация цифровой модели тепловых характеристик на основе температурного поля

В.В. Позевалкин ⬤ ✉, **А.Н. Поляков** ⬤

Оренбургский государственный университет, г. Оренбург, Российская Федерация

✉ pozevalkinvv@mail.ru

Аннотация

Введение. Компьютерное моделирование позволяет инженерам принимать обоснованные проектные решения за счет точной оценки тепловых характеристик объектов проектирования. Актуальным направлением научных исследований и разработок является реализация технологии цифровых двойников в процессе проектирования технических объектов. Для этого необходимо разрабатывать компьютерные модели, точность которых соответствует требованиям, предъявляемым к цифровым двойникам. Однако в научной литературе недостаточно широко представлены результаты исследований, направленных на реализацию технологии цифровых двойников в процессе проектирования. В основном рассматриваются общие вопросы, связанные с применением цифровых двойников в различных отраслях промышленности. Поэтому целью данного исследования явилась разработка цифровой модели и сравнительный анализ точности расчетов тепловых характеристик объекта проектирования.

Материалы и методы. В качестве основного инструмента для проведения исследования выступает предложенная авторами методика разработки компьютерной модели тепловых характеристик для реализации технологии цифровых двойников. Численное решение реализовано путем построения тепловой модели для расчета температурного поля на основе метода конечных элементов в системе инженерного анализа «Ansys» от компании «Ansys Inc» (США). Для аналитического решения применяется разработанная на основе метода пространства состояний компьютерная модель тепловых характеристик, реализованная в модуле «Ansys Twin Builder». Модель пространства состояний приводится в соответствие с поведением исходной тепловой модели путем приближения передаточной функции к пошаговому отклику тепловой нагрузки с применением метода векторной аппроксимации во временной области. Верификация построенной аналитической модели выполнялась в системе инженерных расчетов «MATLAB» от компании «The MathWorks» (США). Исследования проводились для станка модели 400V производства предприятия ООО «НПО «Станкостроение» г. Стерлитамак (Россия).

Результаты исследования. Разработана цифровая модель, позволяющая с высокой точностью выполнить расчет тепловых характеристик объекта проектирования. Результаты сравнительного анализа показывают высокую степень соответствия значений тепловых характеристик, полученных с помощью предложенной цифровой модели, результатам численного моделирования. Максимальная погрешность расчета тепловых характеристик не превышает 0,1°C.

Обсуждение и заключение. Компьютерное моделирование, сочетающее численные методы расчета и научный подход, основанный на технологии цифровых двойников, позволяют получить результат максимально приближенный к результатам экспериментов. Предложенная в исследовании цифровая модель является эффективным решением, поскольку позволяет выполнить расчеты для оценки тепловых характеристик в режиме реального времени, что является одним из важнейших требований при реализации технологии цифровых двойников.

Ключевые слова: цифровой двойник, сложный технический объект, компьютерное моделирование, автоматизированное проектирование, температурное поле, тепловые характеристики

Machine Building and Machine Science

Introduction. Computer modeling has traditionally been an effective tool for solving thermal problems at an early stage of designing complex technical facilities. However, solving the problem requires an accurate assessment of the thermal characteristics of the design object to reduce the negative effects caused by an increase in temperature [1]. At the same time, one of the effective tools for preliminary assessment of thermal characteristics is simulation modeling in an engineering analysis system based on advanced digital solutions and developments. In [2], for example, a developed digital twin for determining thermal characteristics was presented by the authors Jianying Xiao and Kangoo Fan. The principle of operation of the twin was to simulate the thermal behavior of an object through displaying and correcting thermal boundary conditions. The experimental results showed a high accuracy of the model (more than 95%), which was essential for improving the accuracy of modeling thermal characteristics and thermal optimization. Therefore, the urgent direction of scientific research and development in the field of modeling is the use of artificial intelligence systems [3] and digital twins [4]. In [3] by Haoran Yi and others, an interactive model for correcting thermal boundary conditions based on a neural network was proposed to improve the accuracy of the analysis of thermal characteristics. The experimental results showed that the accuracy of calculating the temperature field exceeded 98%, and the accuracy of predicting thermal deformation was 96%, which effectively increased the simulation accuracy. In addition, in [5] by Kurganova N.V. and others, it was noted that digital twins were often used to improve physical prototypes of complex technical objects, since they not only allow for the information support for the design process, but also contribute to effective design decisions based on developments in the field of artificial intelligence.

One of the characteristic features of digital twin technology is that reduced-order computer models are often used for simulation [6]. Therefore, the development of computer models is one of the basic conditions for the implementation of digital twin technology [7]. Model order reduction is an effective and mathematically understandable approach to overcome the time constraints of multidimensional simulation models. In [8] by Mirzoev D.A. and others, for example, a simple analytical model of thermal fields was proposed for the development of digital counterparts of the industrial arc welding process. Bordachev E.V. and Lapshin V.P. [9] presented the results of mathematical modeling of the temperature in the tool–product contact zone under metal turning. This approach provides obtaining an accurate assessment of thermal characteristics corresponding to the results of numerical experiments in real time. Schröder C. and Matthias V. [10] presented a reduced-order model and proposed a new model balancing procedure based on the transformation of the state shift. In conclusion, they presented the results of a comparative analysis and the results from literature sources obtained through a series of numerical experiments.

The use of a linear and time-invariant reduced-order computer model allows for fast simulation while maintaining high calculation accuracy [11]. When developing a computer model, approximation [12] of the transfer function is performed to approximate the state space model to the step response of the initial thermal model [13]. Since the step response of the thermal load is derived from the base thermal model, the digital model should provide the same values of thermal characteristics.

However, despite the fact that recently there has been an increase in interest in the digital twin, the scientific literature does not widely present the results of research related to the implementation of digital solutions in the design of technical facilities. Based on a systematic review of the literature and thematic analysis of publications on digital twins, one of the key knowledge gaps associated with the development of mathematical, software and methodological support for high-precision computer models in the framework of the implementation of digital twin technology has been identified.

In this regard, the objective of the study was to develop a reduced-order computer model and analyze its feasibility as part of a digital model for accurate calculation of thermal characteristics of complex technical design objects.

To achieve that, it was necessary to build a thermal model and calculate the temperature field of the design object, generate independent step responses of the thermal load using the developed software scenario [14], implement a digital model for calculating thermal characteristics, determine the error of calculations obtained using numerical and analytical solutions, and conduct a comparative analysis of the simulation results.

Materials and Methods. The construction of the temperature field of the modeling object was performed for a homogeneous isotropic body on the basis of the equation of nonstationary thermal conductivity:

$$\partial T / \partial t = a^2 \Delta T + q_v / c, \tag{1}$$

where T — temperature (°C); t — time (s); $a = \sqrt{\lambda / (\rho \cdot c)}$ — diffusivity coefficient (m²/s); λ — thermal conductivity coefficient (W/m·°C); c — specific heat capacity (J/kg·°C); ρ — material density (kg/m³); Δ — Laplace operator; q_v — volumetric heat dissipation power (W/m³).

The heat flow in the heat transfer process was assumed to be equal to the amount of heat transferred through an arbitrary surface area S per unit time t. It is expressed by the following equation:

$$Q = -\int_t \int_S q_n dS dt,$$ (2)

where Q — heat flow (W); q_n — heat-flux rate (W/m^2); S — surface area (m^2).

The density of the heat flux during heat transfer was determined from the formula:

$$q_c = \alpha \cdot S \cdot (T_S - T_\infty),$$ (3)

where α — heat transfer coefficient (W/(m^2°C)); T_S — surface temperature (°C); T_∞ — ambient temperature (°C).

In this regard, to calculate the temperature field of the modeling object according to formula (1), heat flows (2) and (3) were set, which determined the amount of heat passing through the surface per unit time.

A component (Fig. 1) of a metal-cutting machine 400V model manufactured by NPO "Stankostroenie" LLC (Sterlitamak, Russia) in the form of a drillhead was selected as the object of modeling.
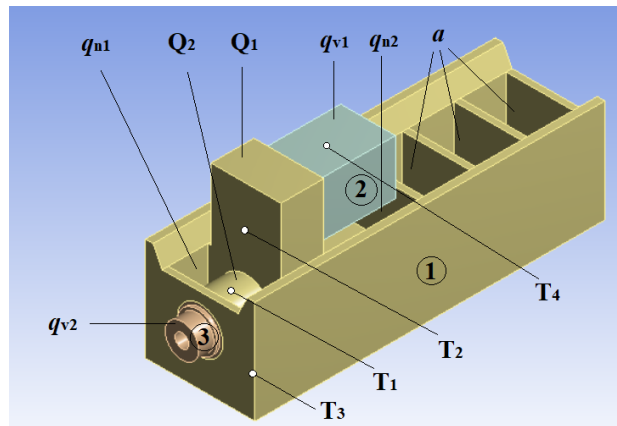
Fig. 1. Geometric model of the object in ANSYS Design Modeler: 1 — housing; 2 — electric motor; 3 — spindle assembly; Q — heat flows; qv — volume heat release power; qn — heat flux densities; a — heat transfer coefficient; T1–T4 — temperature sensors

Since the amount of heat released mainly by the electric motor (electromagnetic losses) and the spindle assembly (mechanical friction losses) was taken into account for calculating the temperature field, electric motor q_{v1} and spindle assembly q_{v2}, were taken as internal heat sources, near which the corresponding heat flows Q_1 and Q_2 were set. The densities of heat fluxes q_{n1}, q_{n2} were assigned to surfaces located near the electric motor and spindle assembly, respectively.

Convection was determined by the heat transfer coefficient α taking into account the conditions of heat transfer (natural convection in air). Since the machine is in contact with a gaseous medium (air), the amount of heat given by the heated surface to the environment per time unit t, is directly proportional to the difference in temperature between surface T_S and medium T_∞ depending on the area of the heat-emitting surface S (3).

When constructing a thermal model of an object (solid) consisting of a homogeneous material (structural steel) with constant thermophysical properties and the presence of internal heat sources, the following initial and boundary conditions were assigned:

– initial conditions took into account the fixation of a constant temperature over the entire surface of the modeling object ($t = 0$: $T = T_0 = const$);

– boundary conditions of the second kind were set by the heat flows of the electric motor (Q_1), the spindle assembly (Q_2), the density of the heat flux (q_{n1}) from the electric motor to the front wall of the housing and (q_{n2}) to the inner surfaces;

– boundary conditions of the third kind were set by the heat transfer coefficient (α) for the surfaces located inside the body of the drillhead;

– boundary conditions of the fourth kind for the contact joints of the surfaces took into account the perfect thermal contact and the absence of thermal resistance:

$$T\big|_{-0} = T\big|_{+0} \,; \lambda_1 \frac{\partial T}{\partial n}\bigg|_{-0} = \lambda_1 \frac{\partial T}{\partial n}\bigg|_{+0} + q_v.$$ (4)

Heat flows (Q_1, Q_2), heat flux densities (q_{n1}, q_{n2}), as well as volume heat dissipation capacity (q_{v1}, q_{v2}), were assigned in accordance with well-known recommendations for metal-cutting machines [1]. Boundary conditions, as well as heat flows, were set for external surfaces. Therefore, it was taken into account that the interrelationships of thermal fields were present only between the outer surfaces.

Machine Building and Machine Science

Differential equation (1), together with the initial and boundary conditions of the second (2), third (3) and fourth (4) kinds, is a mathematical formulation of the problem. The task was solved using numerical and analytical modeling methods.

The numerical solution was performed on the basis of the finite element method in the ANSYS engineering analysis system, which is being developed by ANSYS Inc. (USA) and supplied by "Modeling and Digital Twins" AO, an authorized ANSYS distributor in Russia. The geometric model (Fig. 1) of the object was imported into the ANSYS Workbench project with the addition of the Transient Thermal analysis block. In the numerical solution, the simulation parameters and boundary conditions of the thermal model were calibrated (Table 1) to approximate the model temperature values to the experimental data.

Table 1

Boundary conditions (parameters) of the thermal model

Parameter	Heat dissipation capacity		Heat flows		Heat flux densities		Heat transfer coefficient
	q_{v1}, W/m³	q_{v2}, W/m³	Q_1, W	Q_2, W	q_{n1}, W/m²	q_{n2}, W/m²	a, W/(m²·°C)
Value	6,500	1,000	28	15	32	18	15

In the ANSYS Mechanical module, the initial (initial temperature $T_0 = 24$ °C) and boundary (Table 1) conditions were assigned for the developed grid model, the temperature field was constructed (Fig. 2). In this case, the thermal conductivity coefficient was assumed to be equal to $\lambda = 60.5$ W/(m·°C) and was assigned as such for structural steel.

The thermal model of the object included two contact connections for an electric motor and a spindle cartridge with a drillhead body, and contained 7 thermal boundary conditions. The developed grid model consisted of 16,309 elements and 58,527 nodes.

The total simulation time of 21,600 seconds (6 hours) was divided into intervals (1 hour) and steps $\Delta t = 360$ seconds (6 minutes), a total of $N = 60$ steps within which the parameters of the thermal model (boundary conditions) were assumed to be constant and independent of time.
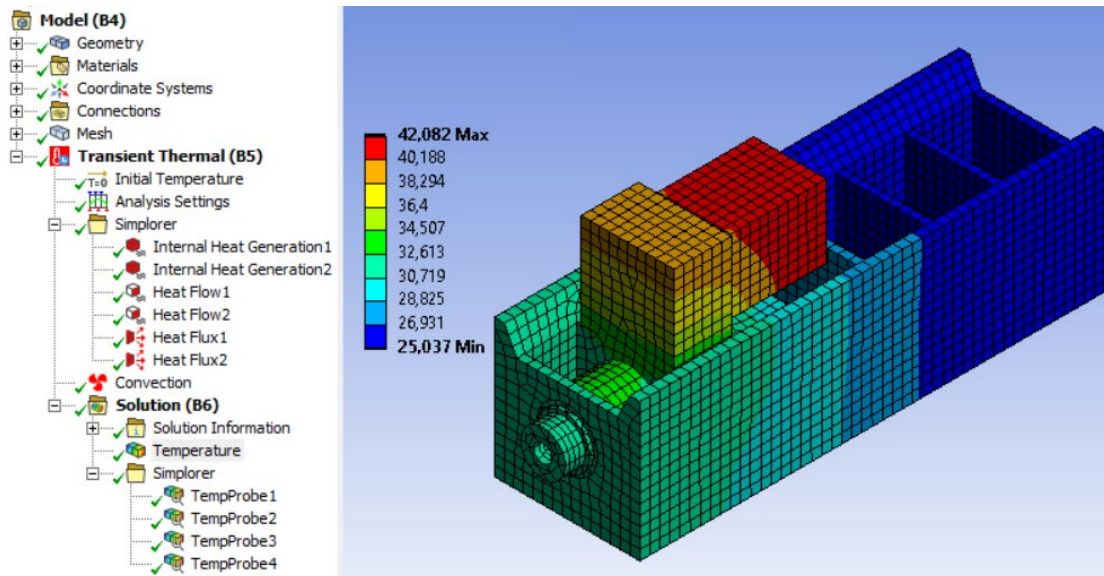
Fig. 2. Temperature field of the object in ANSYS Mechanical

The calculation of the temperature field was required to generate an independent step response of the thermal load, containing information about temperature variation over time (thermal characteristics) for each parameter (Table 1) of the thermal model separately:

$$\tilde{y}_i(t) = T_{i,j}(t), i = \overline{1, k}, \ j = \overline{1, m}, \tag{5}$$

where k — number of temperature sensors; m — number of parameters of the thermal model.

Step response generation was performed in the ANSYS Mechanical module using the Application Customization Toolkit (ACT) extension, which supported the implementation of user scenarios. This made it possible to develop a software script in the Python programming language to automatically generate a special set of files containing independent step responses [14].

The analytical solution was performed on the basis of the state-space method through constructing a model of thermal characteristics according to the formula:

$$\begin{cases} \dot{x} = Ax + Bu \\ y = Cx + Du \end{cases}, \tag{6}$$

where $\dot{x} = \partial x / \partial t$ — derivative of state vector x over time t; y and u — vectors of output and input data, respectively; A, B, C, D — matrices of constant coefficients.

In equation (6), vector $x = (x_1, x_2, \ldots, x_N)^T$ contains state variables, input vector $u = (q_{v1}, q_{v2}, Q_1, Q_2, q_{n1}, q_{n2}, T_{01}, T_{02}, \ldots, T_{0k})^T$ — values of the parameters of the thermal model (boundary and initial conditions), output vector $y = (T_1, T_2, \ldots, T_k)^T$ — values of thermal characteristics.

The transfer function model is expressed by the following equation:

$$y_i(t) = \sum_{j=1}^{m} H_{i,j}(t) u_j, \, i = \overline{1, k}, \tag{7}$$

where H — matrix complex transfer function.

Matrix transfer function H is obtained through applying the Laplace transform to formula (6), which is expressed by the following equation:

$$H(s) = C(sI - A)^{-1} B + D, \tag{8}$$

where s — Laplace complex variable; I — unity diagonal matrix.

Transfer function (8) reflects the dependence of the Laplace transform of output variable $Y(s) = H(s)U(s)$ on the Laplace transform of the input variable $U(s)$ of model (6) under zero initial conditions $x(0) = x_0 = 0$. In this case, the dimension of the transfer function matrix H depends on the output value $k = 4$ and the dimension of the input value $m = 10$, which corresponds to the dimension of the initial step response (5). Therefore, model (6) is brought into line with the behavior of the source thermal model through approximating its transfer function (7) to step response (5) using the vector approximation method [15].

To construct the coefficient matrices of model (6), a reverse transition is performed from transfer function (8) to the model in the state space. In this case, transfer function (8) takes the form of the equation, whose denominator contains a characteristic polynomial of degree $l = 4$ (the order of the system), and the numerator contains a polynomial of degree $z = l - 1$:

$$G(s) = \frac{P(s)}{Q(s)}, \, P(s) = b_0 + \sum_{i=1}^{z} b_i s^i, \, Q(s) = a_0 + \sum_{i+1}^{l} a_i s^i, \tag{9}$$

where a and b — coefficients of polynomials $Q(s)$ and $P(s)$, respectively.

The roots of polynomials $Q(s)$ and $P(s)$ represent the poles and zeros of transfer function (8), respectively. The method of indefinite multipliers is applied to equation (9) to decompose each element of matrix H into elementary fractions. Denoting the poles of the characteristic polynomial by p_i, we obtain an equation of the following form:

$$G(s) = D + \sum_{i=1}^{q} \frac{R_i}{s - p_i}, \tag{10}$$

where $R_i = \lim_{p \to p_i} (s - p_i) \frac{P(s)}{Q(s)}$ — matrix of dimension $(k \times m)$; q — number of poles.

The rank of matrix R_i is denoted by r_i, and its decomposition into the product of two matrices with the full rank of the column and row, respectively, is performed:

$$R_i = C_i^{k \times r_i} B_i^{r_i \times m}, \, rank(R_i) = r_i. \tag{11}$$

The matrices of model (6) are diagonal, of dimension $A^{n \times n}$, $B^{n \times m}$, $C^{k \times n}$, $D^{k \times m}$ ($n = 56$) and contain elements that are obtained directly from the coefficients of transfer function (10).

System matrix A and control matrix B contain the following coefficients:

$$A = \begin{bmatrix} p_{i1} & 0 & 0 & \ldots & 0 \\ \ldots & \ldots & \ldots & \ldots & \ldots \\ 0 & p_{i2} & 0 & \ldots & 0 \\ 0 & 0 & p_{i3} & \ldots & 0 \\ \ldots & \ldots & \ldots & \ldots & \ldots \\ 0 & 0 & 0 & \ldots & p_{qn} \end{bmatrix}, B = \begin{bmatrix} b_{i1} & 0 & \ldots & 0 \\ \ldots & b_{i2} & \ldots & 0 \\ b_{q1} & \ldots & \ldots & 0 \\ 0 & b_{q2} & \ldots & b_{im} \\ \ldots & \ldots & \ldots & \ldots \\ 0 & 0 & \ldots & b_{qm} \end{bmatrix}. \tag{12}$$

Output matrix C and feed forward matrix D contain the following coefficients:

$$C = \begin{bmatrix} c_{i1} & \dots & c_{1q} & 0 & \dots & 0 & 0 & \dots & 0 \\ \dots & \dots & \dots & \dots & \dots & \dots & \dots & \dots & \dots \\ 0 & \dots & 0 & c_{(k-1)i} & \dots & c_{(k-1)q} & 0 & \dots & 0 \\ 0 & \dots & 0 & 0 & \dots & 0 & c_{k,i} & \dots & c_{k,q} \end{bmatrix}, D = \begin{bmatrix} 0 & \dots & 1 & \dots & 0 & 0 \\ \dots & \dots & \dots & \dots & \dots & \dots \\ 0 & \dots & 0 & \dots & 1 & 0 \\ 0 & \dots & 0 & \dots & 0 & 1 \end{bmatrix}. \tag{13}$$

This approach makes it possible to perform the transition from a model in the form of transfer function (8) to a model in state space (6). The transition algorithms are also implemented in the MATLAB engineering calculation system of The MathWorks, Inc. (USA), in the form of special functions «ss2tf()» and «tf2ss()».

To obtain the values of thermal characteristics, the Cauchy problem is solved for a system of ordinary differential equations, since in formula (6), variable $\dot{x}$ is a derivative of the vector of states of the temperature field in time t. The solution to system of equations (6) is obtained using the fourth-order Runge-Kutta method.

Verification of the constructed analytical model was performed through conducting a series of computational experiments using an application program developed in the MATLAB system, which included the implementation of the fourth-order Runge-Kutta method (Fig. 3). Computational experiments were conducted on a personal computer (AMD Ryzen 5 5600U processor with Radeon Graphics 2.30 GHz, RAM 16.0 GB, system type 64-bit Windows 10 Pro version 21H2 operating system), whose characteristics were basic for modern computing technology.

The constructed analytical model and the application of the fourth-order Runge-Kutta method for solving a system of differential equations made it possible to calculate the values of thermal characteristics with high accuracy (Fig. 3). Due to the fact that the maximum error values, i.e., the difference between the model values of thermal characteristics obtained using numerical (FE-Model) and analytical (LTI-Model) solutions, did not exceed 0.72 °C over the entire modeling interval.
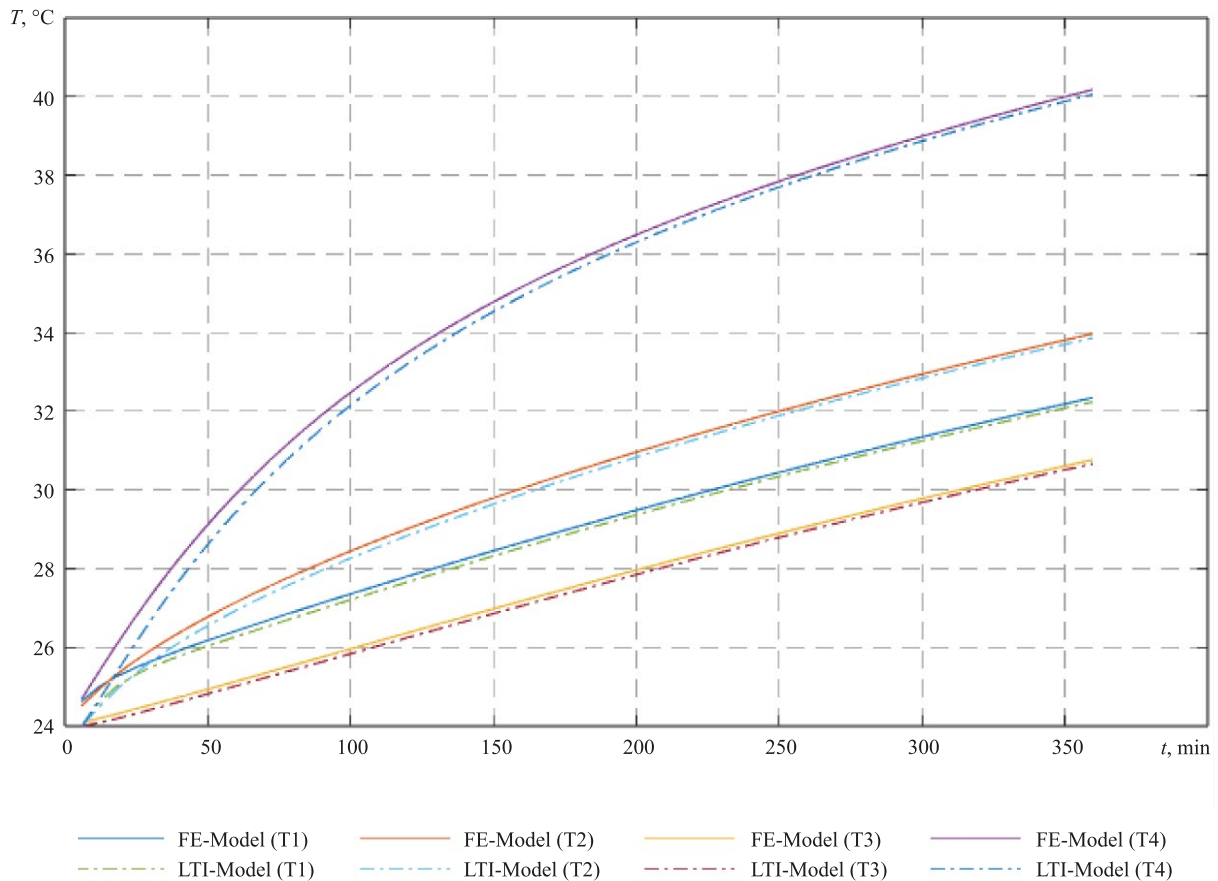
Fig. 3. Graphs of thermal characteristics in MATLAB system

Linear and Time-Invariant (LTI) Reduced Order Model (ROM) was developed in the ANSYS Twin Builder module of the ANSYS engineering analysis system based on the object's temperature field and the step response generated in the ANSYS Mechanical module.

The implementation of the digital model of thermal characteristics based on a temperature field using vector approximation consists in the sequential execution of seven main stages.

Stage 1. Importing a geometric model of an object and building a thermal model in an engineering analysis system.

Stage 2. Calculation of the object's temperature field based on the developed thermal model.

Stage 3. Generation of an independent step response based on the results of numerical modeling of the thermal characteristics of the object.

Step 4. Application of the vector approximation algorithm to obtain the poles and zeros of the transfer function of the state space model.

Stage 5. Building a model of the state space based on a known transfer function.

Stage 6. Development of a computer model of thermal characteristics.

Stage 7. Implementation of the digital model of the object.

Thus, the proposed digital model containing a computer model for an accurate assessment of the thermal characteristics of complex technical design objects was obtained through sequential completing all the above steps.

Research Results. The developed computer model (Thermal_SG400V_SML1) contains 6 inputs and 4 outputs (Fig. 4); this provides identifying the relationship between the parameters of the thermal model and the values of thermal characteristics. The volume heat release power (q_{v1}, q_{v2}), heat flows (Q_1, Q_2) and heat flux densities (q_{n1}, q_{n2}) were taken as input data of the computer model. The output data were thermal characteristics ($T1$–$T4$). The computer model is part of the digital model (Fig. 4 *a*) of thermal characteristics implemented in the ANSYS Twin Builder module.

The values of the parameters of the digital model, presented in the tabular form (Fig. 4 *c*), are fed to the input of the computer model (Fig. 4 *a*) using the STEP components. The graphic module shows the values of thermal characteristics (Fig. 4 *b*) obtained at the output of the computer model.

a)

b)

	1	2	3	4	5	6
Time, s	3,600	7,200	10,800	14,400	18,000	21,600
$q_{n}2$	18.0	18.0	18.0	18.0	18.0	18.0
$q_{v}1$	6,500.0	6,500.0	6,500.0	6,500.0	6,500.0	6,500.0
$Q1$	28.0	28.0	28.0	28.0	28.0	28.0
$Q2$	15.0	15.0	15.0	15.0	15.0	15.0
$Q_{v}2$	1,000.0	1,000.0	1,000.0	1,000.0	1,000.0	1,000.0
$q_{n}1$	32.0	32.0	32.0	32.0	32.0	32.0

c)
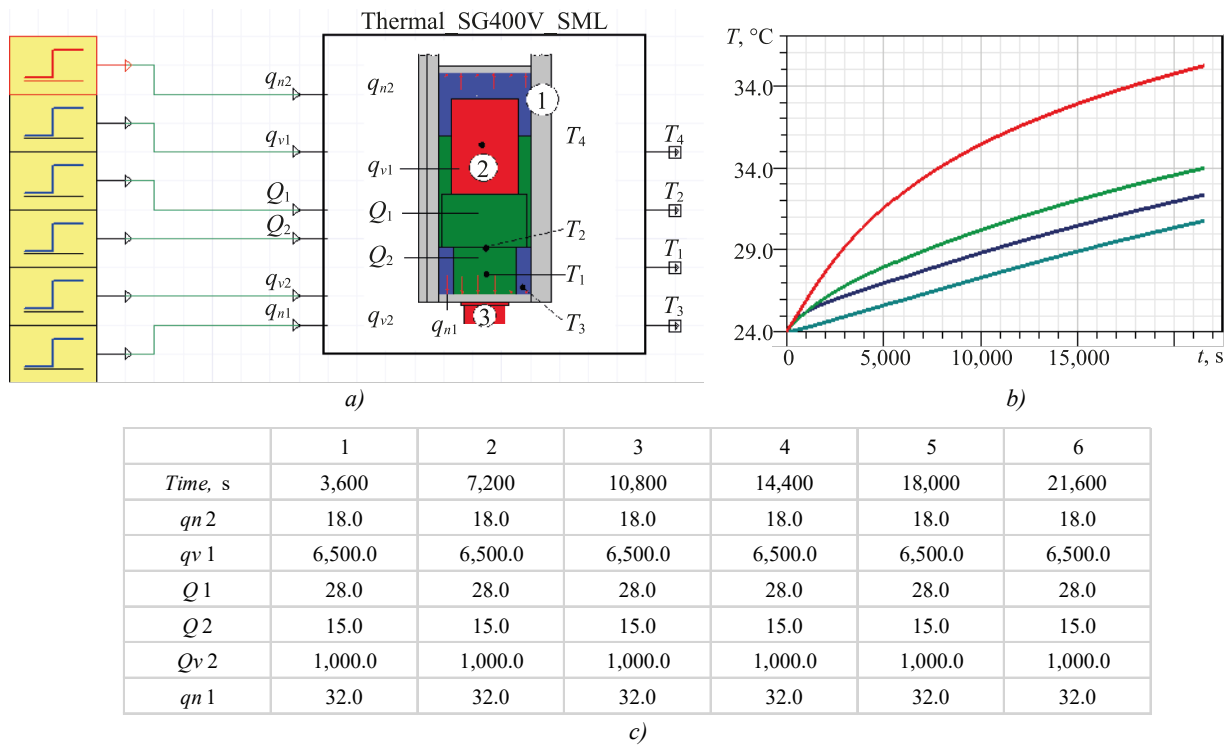
Fig. 4. Implementation of digital model in Ansys Twin Builder system: *a* — computer model of thermal characteristics; *b* — module for graphical representation of results; *c* — module for monitoring input data of the computer model

During the development of the computer model, the limits of dimension from 2 to 4 orders, values of the target error $\varepsilon = 5\times10^{-3}$, and the tolerance for the zero order $\varepsilon_0 = 2\times10^{-3}$ were set. The remaining parameters were set automatically, since the vector approximation method was as automated as possible in comparison to other methods that were supported in the ANSYS Twin Builder module.

In the process of developing a computer model, the ANSYS Twin Builder module automatically generated a special matrix of approximation errors $M_{ij} = || y_i(t) - \tilde{y}_i(t) ||_j$ in the time domain, each element of which reflected the difference between the values of the thermal characteristics of step response (5) and transfer function (7) of the model in the state space. It is expressed by the following equation:

$$M = \begin{bmatrix} 0.43 & 4.04 & 1.53 & 4.97 & 2.22 & 1.82 \\ 0.21 & 2.22 & 2.54 & 1.07 & 1.16 & 1.95 \\ 2.66 & 1.63 & 0.39 & 0.26 & 3.43 & 1.82 \\ 1.46 & 3.21 & 0.06 & 0.84 & 2.95 & 3.50 \end{bmatrix} \times 10^{-3}. \tag{14}$$

Machine Building and Machine Science

In this case, the maximum relative error did not exceed value ε = 4.97 × 10⁻³. At the same time, all other error values turned out to be less than the specified limit ε = 5 × 10⁻³. Zero-error value in matrix (14) meant that the input was ignored due to a very small contribution.

The estimation of the accuracy of the calculation of thermal characteristics using the proposed digital model was carried out through comparative analysis of the results obtained using numerical and analytical solutions. The comparative analysis was performed according to the criterion of maximum error. Maximum error ΔT_{max}, i.e., the difference between the values of thermal characteristics obtained using numerical and analytical solutions for all temperature sensors, was calculated at each time by the formula:

$$\Delta T_{max} = \max_{j=1,n} \Delta T_j, \tag{15}$$

where $\Delta T_j = |T_{j,f} - T_{j,d}|$ — error; $T_{j,f}$ and $T_{j,d}$ — temperature values of the finite element and digital models, respectively ($j = \overline{1, m}$); m — number of temperature sensors.

To assess the digital model accuracy, an error calculation was performed, whose results were presented in the form of a surface (Fig. 5 *a*) and a linear graph (Fig. 5 *b*) of the maximum time error. The surface (Fig. 5 *a*) represented the calculated error values for each temperature sensor (dT1, dT2, dT3, dT4) individually and at each time point over the entire simulation interval.

a)

b)
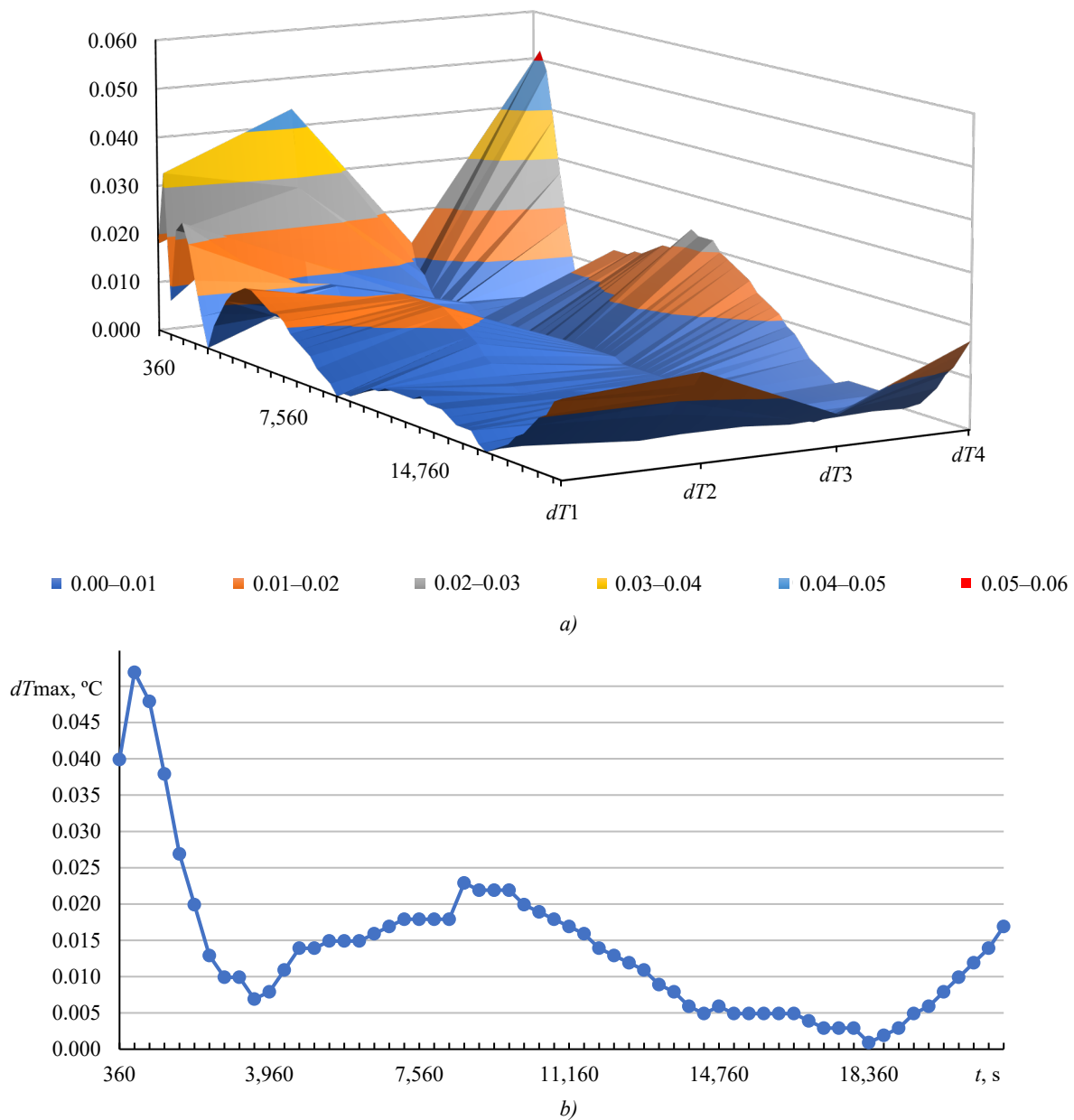
Fig. 5. Errors in the calculation of thermal characteristics: *a* — error for each temperature sensor;
b — maximum error for all temperature sensors

The graph (Fig. 5 *b*) showed that for the selected time interval, maximum errorΔT_{max} did not exceed 0.1 °C. The error in calculating the thermal characteristics for each temperature sensor separately (Fig. 5 *a*) did not exceed the specified limits either.

Discussion and Conclusion. The obtained results of computational experiments and the conducted comparative analysis confirm the efficiency of the proposed digital model, which provides calculating thermal characteristics with high accuracy $\Delta T_{max} = 0.052$ °C, for further analysis and identification of the thermal model.

The temperature field of the design object is influenced by many factors, which complicates the determination of the nominal values of thermal boundary conditions. To solve this problem, the study first analyzes the key technologies involved in the implementation of the digital twin of a complex technical object, then builds a thermal model and a computer reduced-order model LTI ROM of the transient temperature field. The developed computer model is used as part of a digital model that provides obtaining an accurate assessment of the thermal characteristics of the design object and thereby increases the efficiency of design procedures in the process of computer-aided design of complex technical facilities.

The accuracy and efficiency of calculations of the reduced-order computer model and the source full-order thermal model are evaluated by comparative analysis of the simulation results. The results of computational experiments show that, from the point of view of calculation accuracy, computer models of reduced order and finite element models of full order are generally comparable in accuracy, the maximum calculation error is within the acceptable range and does not exceed 0.1°C.

The results obtained during computational experiments do not contradict the results presented in the sources of scientific literature on similar topics and allow us to conclude that the use of the proposed digital model is effective for evaluating the thermal characteristics of complex technical objects in real time, which is one of the most important conditions for the implementation of digital twin technology.

However, changes in the temperature field of a complex technical facility still depend on many factors. Therefore, in further research, it is necessary to develop computer models of thermal deformations and conduct effective optimization algorithms based on artificial intelligence to provide the reliability of simulation results obtained using digital twins.

References

1. Bushuev VV, Kuznetsov AP, Sabirov FS, Khomyakov VS, Molodtsov VV. Precision and Efficiency of Metal-Cutting Machines. *Russian Engineering Research*. 2016;36:762–773. https://doi.org/10.3103/S1068798X16090070

2. Jianying Xiao, Kaiguo Fan. Research on the Digital Twin for Thermal Characteristics of Motorized Spindle. *The International Journal of Advanced Manufacturing Technology*. 2022;119:5107–5118. https://doi.org/10.1007/s00170-021-08508-y

3. Haoran Yi, Kaiguo Fan. Co-Simulation-Based Digital Twin for Thermal Characteristics of Motorized Spindle. *The International Journal of Advanced Manufacturing Technology*. 2023;125(9–10):4725–4737. https://doi.org/10.1007/s00170-023-11060-6

4. Kuo Liu, Lei Song, Wei Han, Yiming Cui, Yongqing Wang. Time-Varying Error Prediction and Compensation for Movement Axis of CNC Machine Tool Based on Digital Twin. *IEEE Transactions on Industrial Informatics*. 2022;18(1):109–118. https://doi.org/10.1109/TII.2021.3073649

5. Kurganova N, Filin M, Cherniaev D, Shaklein A, Namiot D. Digital Twins' Introduction as One of the Major Directions of Industrial Digitalization. *International Journal of Open Information Technologies*. 2019;7(5):105–115. http://injoit.org/index.php/j1/article/view/748

6. Jones D, Snider C, Nassehi A, Yon J, Hicks B. Characterising the Digital Twin: A Systematic Literature Review. *CIRP Journal of Manufacturing Science and Technology*. 2020;29A:36–52. https://doi.org/10.1016/j.cirpj.2020.02.002

7. Aumann Q, Benner P, Saak J, Vettermann J. Model Order Reduction Strategies for the Computation of Compact Machine Tool Models. In: *Proc. 3rd International Conference on Thermal Issues in Machine Tools*. Cham: Springer; 2023. P. 132–145. https://doi.org/10.1007/978-3-031-34486-2_10

8. Mirzaev DA, Okishev KYu, Mirzoev AA. A Simple Analytical Model of Thermal Fields to Develop Digital Twins in Industrial Arc Welding. *Vestnik of South Ural State University. Series: Mathematics. Mechanics. Physics*. 2023;15(1):76–86. https://doi.org/10.14529/mmph230109

Machine Building and Machine Science

9. Bordatchev EV, Lapshin VP. Mathematical Temperature Simulation in Tool-to-Work Contact Zone during Metal Turning. *Advanced Engineering Research (Rostov-on-Don)*. 2019;19(2):130–137. https://doi.org/10.23947/1992-5980-2019-19-2-130-137

10. Schröder C, Matthias V. Balanced Truncation Model Reduction with a Priori Error Bounds for LTI Systems with Nonzero Initial Value. *Journal of Computational and Applied Mathematics*. 2023;420:114708. https://doi.org/10.1016/j.cam.2022.114708

11. Xaver Thiem, Kauschinger B, Ihlenfeldt S. Online Correction of Thermal Errors Based on a Structure Model. *International Journal of Mechatronics and Manufacturing Systems*. 2019;12(1):49–62. https://doi.org/10.1504/IJMMS.2019.097852

12. Klochkov YuV, Nikolaev AP, Ishchanov TR, Andreev AS. FEM Vector Approximation for a Shell of Revolution with Account for Shear Deformations. *Journal of Machinery Manufacture and Reliability*. 2020;49:301–307. https://doi.org/10.3103/S105261882004007X

13. Xiao Hu, Scott Stanton, Long Cai, Ralph E White. A Linear Time-Invariant Model for Solid-Phase Diffusion in Physics-Based Lithium Ion Cell Models. *Journal of Power Sources*. 2012;214:40–50. https://doi.org/10.1016/j.jpowsour.2012.04.040

14. Polyakov AN, Pozevalkin VV. *Software Module for Generating Input Data for Building Digital Models*. RF Certificate of State Registration of a Computer Program, No. 2023660032. 2023. 1 p. (In Russ.)

15. Gourary MM, Zharov MM, Rusakov SG, Ulyanov SL, Khodosh LS. An Effective Algorithm for Realization of the Vector Fitting Method for the Identification Tasks of the Dynamical Systems. *Mechatronics, Automation, Control*. 2015;16(9):579–584. https://doi.org/10.17587/mau.16.579-584

About the Authors:

Vladimir V. Pozevalkin, Cand.Sci. (Eng.), Senior Lecturer of the Applied Computer Science in Economics and Management Department, Orenburg State University (13, Pobedy Ave., Orenburg, 460018, Russian Federation), SPIN-code: 4360-0892, ORCID, ScopusID, ResearcherID, pozevalkinvv@mail.ru

Alexander N. Polyakov, Dr.Sci. (Eng.), Professor, Head of the Department of Technology of Mechanical Engineering, Metalworking Machines and Complexes, Orenburg State University (13, Pobedy Ave., Orenburg, 460018, Russian Federation), SPIN-code: 3242-5123, ORCID, ScopusID, anp_temos@mail.ru

Об авторах:

Владимир Владимирович Позевалкин, кандидат технических наук, старший преподаватель кафедры прикладной информатики в экономике и управлении Оренбургского государственного университета (460018, Российская Федерация, г. Оренбург, пр. Победы, 13), SPIN-код: 4360-0892, ORCID, ScopusID, ResearcherID, pozevalkinvv@mail.ru

Александр Николаевич Поляков, доктор технических наук, профессор, заведующий кафедрой технологии машиностроения, металлообрабатывающих станков и комплексов Оренбургского государственного университета (460018, Российская Федерация, г. Оренбург, пр. Победы, 13), SPIN-код: 3242-5123, ORCID, ScopusID, anp_temos@mail.ru

Claimed Contributorship:

VV Pozevalkin: software development, calculation analysis, description of the theoretical part of the study, design of the research article.

AN Polyakov: academic advising, formulation of research objectives and tasks, analysis of the research results, correction of the conclusions.

Заявленный вклад авторов:

В.В. Позевалкин: разработка программного обеспечения, проведение расчетов, описание теоретической части исследования, оформление научной статьи.

А.Н. Поляков: научное руководство, формирование цели и задач исследования, анализ результатов исследований, корректировка выводов.

MACHINE BUILDING AND MACHINE SCIENCE
МАШИНОСТРОЕНИЕ И МАШИНОВЕДЕНИЕ

Original Theoretical Research

Modeling the Dynamic Loads Affecting a Bridge Crane during Start-Up

Imad Rezakalla Antypas [ORCID]
Don State Technical University, Rostov-on-Don, Russian Federation
✉ Imad.antypas@mail.ru

Abstract

Introduction. The dynamic loads during the start-up of a bridge crane can cause excessive stress in the structure and components, leading to potential safety hazards and increased wear and tear. To reduce the influence of the dynamic loads, various strategies can be implemented including optimization of the acceleration and deceleration profiles, using the soft start controls, implementing the vibration damping systems. It is vital to ensure that the proper crane maintenance and inspection protocols are in place. By reducing the impact of dynamic loads during the start-up, the overall performance and longevity of a bridge crane can be improved, ultimately enhancing safety and efficiency of the industrial operations. The present research offers a new approach to improving the efficiency and safety of industrial operations by providing a more precise account of the dynamic loads during the start-up of a bridge crane. The objective of this study is to develop a mathematical model for investigating the mechanical properties of the bridge cranes by analyzing the dynamic loads that occur during lifting operations.

Materials and Methods. The development of the mathematical model was based on the kinetic model of the system, which included three connecting blocks and two flexible connections for a more accurate description of the bridge crane structure. Lagrange's equations incorporating the information about the geometry and structure of a bridge crane were used. They made it possible to describe the motion of a system with the multiple elements and degrees of freedom. Processing and analysis of the results of the mathematical model were carried out in the MATLAB program using the Runge-Kutta method.

Results. As a result of the research, a mathematical model was developed to study the dynamic loads affecting a bridge crane during lifting operations. Graphs describing the dependences of speed, acceleration, load, and rope angle over time, and their influence on the crane beam were plotted. The changes in these parameters over time, including their maximum values, were analyzed. The reasons for load changes and factors influencing the extension of lifting machines' service life as well as reducing metal consumption during production thereof were identified.

Discussion and Conclusion. The developed mathematical model and its numerical solution using the specialized software (MATLAB) allow for conducting the dynamic analysis of the bridge crane structures and determining the optimal design solutions. The analysis of the factors influencing the load changes leads to the conclusion that the use of this model can significantly reduce the load magnitudes and metal consumption, as well as increase the service life of lifting machines. The results obtained with the developed mathematical model and its numerical solution are useful for optimizing the crane structures, providing compliance with the operational requirements, and extending the service life of lifting machines.

Keywords: bridge crane, dynamic load, kinetic model, load lifting, dynamic analysis

Моделирование динамических нагрузок, воздействующих на мостовой кран в момент пуска

И.Р. Антибас 🆔

Донской государственный технический университет, г. Ростов-на-Дону, Российская Федерация

✉ Imad.antypas@mail.ru

Аннотация

Введение. Динамические нагрузки во время запуска мостового крана могут вызывать избыточные напряжения в конструкции, приводя к потенциальным рискам и увеличению износа. Для снижения влияния динамических нагрузок можно применять различные стратегии, включая оптимизацию профилей ускорения и замедления, использование плавного пуска, внедрение систем амортизации. Важно обеспечивать исполнение правильных протоколов обслуживания и инспекции кранов. Путем снижения воздействия динамических нагрузок во время запуска можно улучшить общую производительность и долговечность мостового крана, повысив в конечном итоге безопасность и эффективность промышленных операций. Данное исследование предлагает новый подход к повышению эффективности и безопасности промышленных операций за счет более точного учета динамических нагрузок мостового крана при пуске. Цель работы — разработка математической модели для изучения механических свойств мостовых кранов путем анализа динамических нагрузок, возникающих во время подъемных операций.

Материалы и методы. Разработка математической модели была выполнена на основе кинетической модели системы, включающей три соединительных блока и два гибких соединения для более точного описания конструкции мостового крана. Использованы уравнения Лагранжа, включающие информацию о геометрии и структуре мостового крана. Они позволили описать движение системы с несколькими элементами и несколькими степенями свободы. Обработка и анализ результатов математической модели были произведены в программе MATLAB с применением метода Рунге-Кутты.

Результаты исследования. В результате исследования была разработана математическая модель для изучения динамических нагрузок на мостовой кран во время подъемных операций. Построены графики, описывающие зависимости скорости, ускорения, нагрузки и угла каната относительно времени и их влияние на балку крана. Проанализировано изменение этих параметров во времени, включая их максимальные значения. Определены причины изменений нагрузки и факторы, влияющие на увеличение срока службы и снижение металлоемкости при производстве подъемных машин.

Обсуждение и заключение. Разработанная математическая модель и ее численное решение с использованием специализированного программного обеспечения (программа MATLAB) позволяют проводить динамический анализ конструкций мостового крана и определять оптимальные конструктивные решения. Анализ факторов, влияющих на изменение нагрузки, позволяет сделать вывод, что при использовании данной модели можно значительно снизить величину нагрузок и металлоемкость, а также увеличить срок службы подъемных машин. Результаты, полученные при помощи разработанной математической модели, и ее численное решение полезны при оптимизации конструкции кранов, обеспечении соответствия операционных требований и продлении срока службы подъемных машин.

Ключевые слова: мостовой кран, динамическая нагрузка, кинетическая модель, подъем грузов, динамический анализ

Introduction. The analysis of dynamic processes in the mechanical part plays an important role in the development of new overhead cranes and modernization of existing ones in order to reduce loads on control devices and extend their service life [1].

The bridge crane is subjected to dynamic loads during non-static operations, such as acceleration and braking. Analysis of these processes allows identifying hidden impacts on the dynamic behavior of the bridge crane. Therefore, it is paramount for the researcher to make an optimal design choice to reduce these loads, ensuring that the crane can meet the required operating conditions [2].

In [3], a dynamic model of a crane lifting system was developed, using which an accurate direct numerical integration method was proposed for calculating the dynamic loads of the system.

Papers [4, 5] studied dynamic loads in a metal structure, taking into account fatigue of the metal material. However, the researcher neglected the impact of forces from the drive of the lifting mechanism operating with artificial parameters.

In [6], dynamic loads in a bridge crane were determined during the operation of a lifting mechanism when hoisting a load suspended on a rope. The most important case studied was the effect of dynamic loads on the crane when removing a load from a solid foundation, at the moment of lifting-off.

Steel structures of bridge cranes experience non-stationary loads with different stress amplitudes and asymmetry of the working cycle [7]. To study the real load of bridge cranes under typical operating conditions, constant recording of their stress state is required, which is labor-intensive [8]. Therefore, statistical processing of the obtained results is used to assess the loading elements of metal structures of bridge cranes [9]. This involves changing individual components of the total load of metal elements, such as the gravity of the load being lifted, the angle of rotation of the load, and weather loads, and then summing them according to the laws of probability theory [9, 10]. This approach is less labor-intensive than a comprehensive study of loading under typical operating conditions. However, determining the probabilistic characteristics of individual random loads also takes time, so the method for calculating load combinations is widely used in crane construction [11].

In [12], it was found that during the stage of selecting the rope slack, the value of the stator current of the electric motor of the lifting mechanism did not depend on the mass of the suspended load. However, as the load increased, the time of its rise also increased, and at the stage of separating the load from the surface, the amplitude values of the current increased. Furthermore, a noticeable difference appeared after five periods of mains voltage from the beginning of the stage. However, the researcher neglected the significant influence of forces arising from the drive of the lifting mechanism working with artificial elements.

By using the developed mathematical model, the research aims at optimizing the design of bridge cranes through studying the dynamic loads that occur during lifting operations, ensuring that the crane has the ability to meet the required operating conditions.

Materials and Methods

Kinetic Model of the System under Study. When developing a kinetic model of the system under study, it can be represented that the construction of a bridge crane for a given motion form consists of three connecting blocks and two flexible joints, and has the form shown in Figure 1:
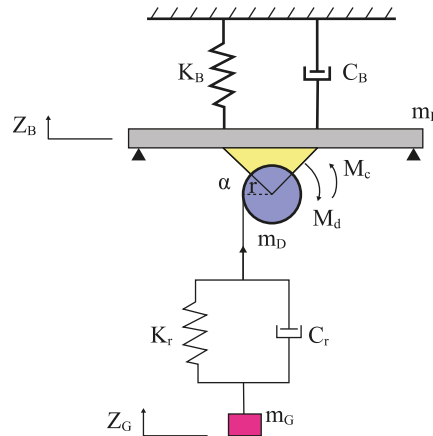
Fig. 1. Bridge crane kinetic model

m_B — mass of the main bridge, moving along the X-axis; m_D — mass of the lifting mechanism, moving along the Y-axis; m_G — payload; K_B and C_B — elasticity modulus and damping coefficient of the main bridge; K_R and C_R — elasticity modulus and damping coefficient of the ropes; α — swing angle of lifting mechanism winding.

Derivation of Kinetic Equations Reflecting the Motion of the Dynamic Model

Mathematical equations representing the motion of the dynamic model are derived from the partial differential Lagrange equation, which is considered to be one of the best methods used specifically in cases where the system consists of more than one element and when it has several degrees of freedom.

$$\frac{\partial}{\partial t}\left(\frac{\partial L}{\partial \dot{q}_i}\right) - \frac{\partial L}{\partial q_i} + \frac{\partial D}{\partial q_i} = Qi \tag{1}$$

$$L = T - U \tag{2}$$

$$\Rightarrow \frac{\partial}{\partial t}\left(\frac{\partial}{\partial \dot{q}_i} - \frac{\partial U}{\partial \dot{q}}\right) - \frac{\partial T}{\partial q_i} + \frac{\partial U}{\partial q_i} + \frac{\partial D}{\partial \dot{q}_i} = Q_i, \tag{3}$$

where T — kinetic energy; U — potential energy; D — damping energy; Q — external forces affecting the whole system; q_i — common system of coordinates; i — degrees of freedom of the model under study.

Kinetic energy equation:

$$T = 0.5m_B \dot{z}_B^2 + 0.5m_D \dot{z}_B^2 + 0.5m_G \dot{z}_G^2 + 0.5J \cdot \dot{\alpha}^2. \tag{4}$$

Potential energy equation:

$$U = 0.5K_B z_B^2 + 0.5K_r \left(z_G - r\alpha + z_B \right)^2. \tag{5}$$

Damping equation:

$$D = 0.5C_B \dot{z}_B^2 + 0.5C_r \left(\dot{z}_G^2 - r\dot{\alpha} + \dot{z}_B \right)^2. \tag{6}$$

System equations:

$$\left(m_B + m_D \right)\ddot{z}_B + K_B z_B + K_r \left(z_B - r\alpha + z_G \right) + C_B \dot{z}_B + Cr \left(\dot{z}_B - r\dot{\alpha} + \dot{z}_G \right) = 0 \tag{7}$$

$$^* m_G \ddot{z}_G + K_r \left(z_G - r\alpha + z_B \right) + C_r \left(\dot{z}_G - r\dot{\alpha} + \dot{z}_B \right) = 0 \tag{8}$$

$$^* J \cdot \ddot{\alpha} + K_r r \left(\alpha - z_G - z_B \right) + C_r \cdot r \left(\dot{\alpha} - \dot{z}_G - \dot{z}_B \right) = M_d - M_c, \tag{9}$$

where M_d, M_c — resistance momentum and lifting mechanism momentum; J — inertia of rotating mass of the lifting mechanism.

Numerical Solution of a Mathematical Model Using the Fourth-Degree Equation of Runge-Kutta

The numerical solution to equations (7–9) was obtained using the Runge-Kutta method in the MATLAB program. The dynamic equations were derived within the program, incorporating the input data and a set of commands to process these equations. The resulting graphs illustrate the interconnections between the various blocks and components of the crane structure under consideration.

The Conditioning of the Input Values Required to Solve the Model

The study was conducted on an ACE type bridge crane consisting of three parts (Fig. 2):

– lifting trolley;

– main bridge, which supports the lifting mechanism;

– end trucks, which support the main bridge.

Fig. 2. Main parts of bridge crane ACE

To align the operation of the bridge crane with a standard set of coordinate axes, the following assumption was made:

– the lifting trolley functions as a unit responsible for raising a load along the Z-axis and allows for horizontal motion along the Y-axis relative to the main bridge, which is the axis along which the crane moves.

A study was conducted on a prototype bridge crane with a lifting capacity of 10 tons and a width of 21.5 meters. The following characteristics were considered:

– payload: $m_G = 10,000$ kg;

– mass of the two main bridges: $m_B = 8,100$ kg;

– mass of the lifting mechanism with the trolley: $m_D = 700$ kg.

When determining the input values, all the laws of designing the structures of lifting devices were followed, and the connections of all components were taken into account. The main factors considered were:

– power of the drive of the lifting mechanism along the Z-axis;

– stiffness coefficient of the steel structure (K_B);

– stiffness coefficient of the rope (K_r);

– damping coefficient of the metal frame (C_B);

– damping coefficient of the ropes (C_r).

Machine Building and Machine Science

Table 1

Shows the elements of the design structure of the bridge crane that was studied.

Element name	Value	Unit of measurement	Notation
Load	10	Ton	m_G
Crane mass	8,100	Kg	m_B
Trolley mass	700	Kg	m_D
Crane length	21.5	m	L
Height of lift	5	m	H
Beam device degree	2	–	A
Gear box ratio	4.5	–	i_m
Coil radius	0.25	m	R
Rope diameter	16.5	mm	d_k
Engine power	30	kW	N_n
Speed of the engine rotor core	905	r.p.m	n_n
Rope stiffness coefficient	11,169.8	N/mm	K_B
Rope damping coefficient	23,934.4	N/mm	K_r
Rope damping coefficient	83.37	N.sec/m	C_r
Metal frame damping coefficient	30.29	N.sec/m	C_B

Research Results
Study of the Model Operation Using a Computer
Structural Behavior of a Metal Bridge Crane under Momenta Loads
The structural behavior of a metal bridge crane during the process of lifting a load is depicted by three curves (Fig. 3).
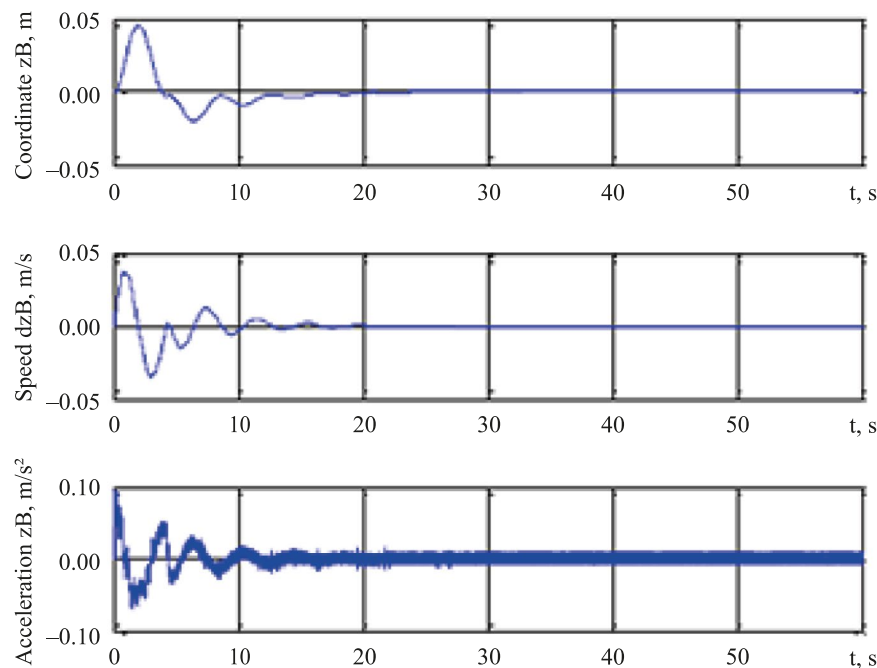
Fig. 3. Coordinates of vertical motion, speed and acceleration of the COG of the bridge cranes versus time curves

In Figure 3, the first curve shows the coordinates of the bridge crane along the ordinate axis as a function of time. During lifting, some vibration of the crane's metal structure is observed for 5–10 seconds, which then stabilizes and does not affect its rigidity.

The second curve in this figure depicts the change in the speed of the center of gravity of the bridge crane over time. During lifting the load, the speed initially increases and then gradually decreases until stabilization. This indicates that the center of gravity of the bridge crane assumes a stable position within the specified time period, during which the vibration stabilizes.

The third curve reflects the change in the center of gravity of the bridge crane over time. It is noteworthy that the acceleration value at the moment of lifting the load is 0.07 m/s², with the dynamic load reaching its maximum.°

Load Curves

Figure 4 shows three curves that reflect motion of the load during the crane operation at the time of lifting.
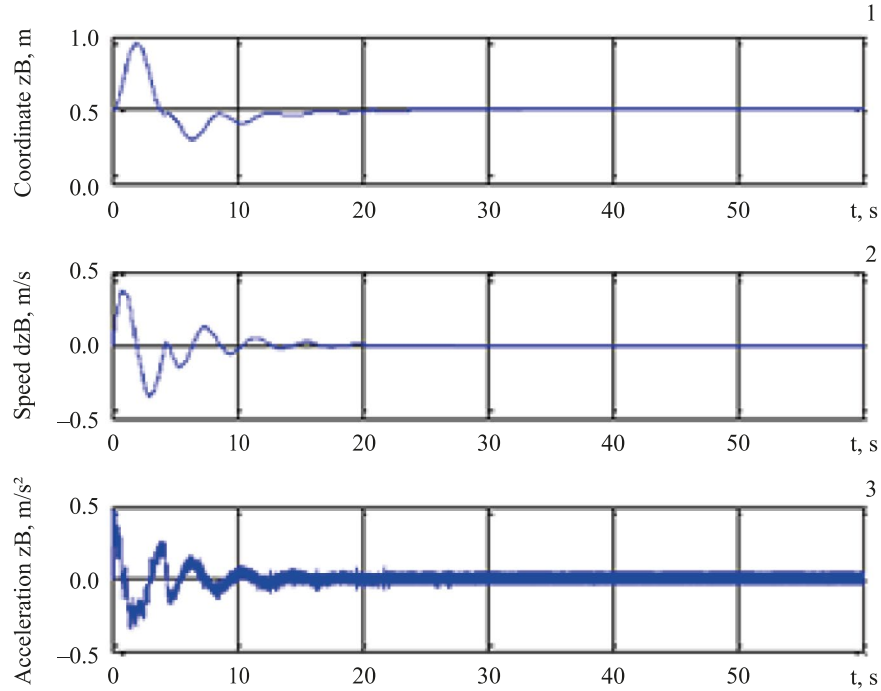
Fig. 4. Coordinates of the speed and acceleration of the load lifting versus time curves

In Figure 4, the first curve reflects the change in the position of the center of gravity of the load over time during its lifting to a certain height, calculated by the program, by rotating the drum by 180 degrees and then stopping. The height of the load suspension indicated on the graph is 0.78 m.

The second curve on this graph shows the change in the lifting speed of the load over time. When the drum rotates, the lifting speed of the load initially increases, then gradually decreases until it stabilizes.

The third curve represents the change in the acceleration of the load lifting over time. At the moment of lifting the load, the acceleration reaches a maximum value of 0.26 m/s² in 0.8 seconds, and then stabilizes.

From the analysis of these three curves, it can be noticed that the stabilization time of the crane operation is almost constant.

Coil Angle Curve

Figure 5 shows the dependence of the winding rotation on time in degrees.
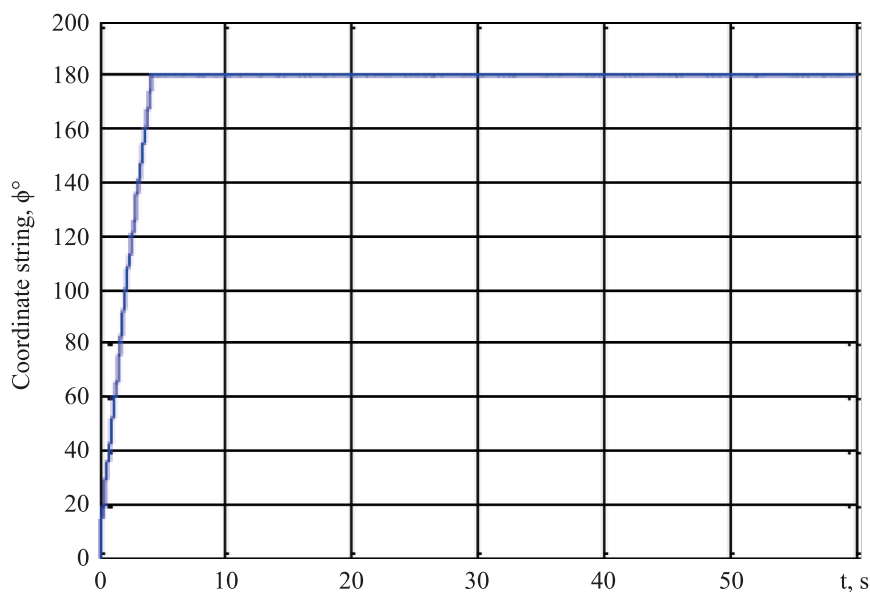
Fig. 5. Coil Angle Curve

Figure 5 shows the change in the angle of rotation of the drum over time. The rotation angle stabilizes when reaching a value of 180 degrees, after which it remains stable, meaning it repeats.

Discussion and Conclusion. Analysis of the above graphs leads to the following conclusions.

The mathematical model and algorithms allow for a detailed study of the motion of a bridge crane at all stages. Adjusting the winch operation and improving the metal structure of the crane have many positive aspects, including reducing dynamic displacements in the metal frame of the crane and transmission elements (such as clutch, gearbox, motor, and pulleys), as well as in the hoisting ropes. This reduction in dynamic loads leads to a decrease in rapid wear of these elements. Additionally, cost savings on maintenance and the development of an optimal metal structure design are achieved, as well as an increase in the crane's service life. This is evident from changes in the center of gravity of the load, speed, and acceleration during its lifting over time. It has been established that the height of the load during lifting, which is directly related to the length of the hoisting ropes, as well as the mass of the lifted load and the design of the main bridge, including its shape and dimensions, significantly influence the dynamic loads experienced by the structure.

The mathematical model offers a new approach to improving the efficiency and safety of industrial operations by providing a more precise understanding and accounting for dynamic loads during the start-up of a bridge crane.

References

1. Fedjaeva GA, Kochevinov DV, Lozbinev VP, Lozbinev FYu. Dynamics Simulation of Bridge Crane Electromechanical System. *Bryansk State University Herald*. 2014;41(1):63–67.

2. Mirsad Čolić, Nedim Pervan, Muamer Delić, Adis J Muminovic, Senad Odzak. Mathematical Modelling of Bridge Crane Dynamics for the Time of Non-Stationary Regimes of Working Hoist Mechanism. *Archive of Mechnical Engineering*. 2022;69(2):189–202. http://doi.org/10.24425/ame.2022.140415

3. Hanjun Pu, Xiaopeng Xie, Guangchi Liang, Xiangyong Yun, Haining Pan. Analysis for Dynamic Characteristics in Load-Lifting System of the Crane. *Procedia Engineering*. 2011;16:586–593. https://doi.org/10.1016/j.proeng.2011.08.1128

4. Goncharov KA, Denisov IA. Maintenance of Working Capacity of Movement Mechanism of Load Trolley with Linear Traction Electric Drive of Bridge Type Crane. *IOP Conference Series: Earth and Environmental Science*. 2017;87(6):062004. https://doi.org/10.1088/1755-1315/87/6/062004

5. Jaafar HI, Mohamed Z, Shamsudin MA, Mohd Subha NA, Liyana Ramli, Abdullahi AM. Model Reference Command Shaping for Vibration Control of Multimode Flexible Systems with Application to a Double-Pendulum Overhead Crane. *Mechanical Systems and Signal Processing*. 2019;115:677–695. https://doi.org/10.1016/j.ymssp.2018.06.005

6. Dooroo Kim, William Singhose. Reduction of Double Pendulum Bridge Crane Oscillations. In: *Proc. 8th International Conference on Motion and Vibration Control*. Daejeon: Genicom Co., Ltd.; 2006. P. 300–305.

7. Akhtulov AL, Kirasirov OM, Kirasirov MO. Features of Calculation of Steel Structures of Bridge Cranes at Variable Loads. *MATEC Web of Conferences*. 2019;298:00032. https://doi.org/10.1051/matecconf/201929800032

8. Antulov AL. Algorithm of Numerical Calculation of Reactions of Constraints in a Dynamic System of Transport Machine. *Journal of Physics: Conference Series*. 2018;944:012002. https://doi.org/10.1088/1742-6596/944/1/012002

9. Akhtulov AL Kirasirov MO, Kirasirov OM, Mashonsky VA. Building the Automation System for Designing Load-Lifting Cranes of Bridge Type. In: *Proc. XVII International Research and Practice Conference "European Science and Technology"*. Munich: Vela Verlag Waldkraiburg; 2017. P. 29–35. URL: https://portal.kuzstu.ru/file/view/68427 (accessed: 08.12.2023).

10. Spitsyna DN, Polikarpov KV. *Dynamics of Cranes with Rigid Load Suspension*. Moscow: Bauman Moscow State Technical University; 2009. P. 160. (In Russ.).

11. Yihai Fang, Yong K Cho, Jingdao Chen. Framework for Real-Time Proactive Safety Assistance for Mobile Crane Lifting Operations. *Automation in Construction*. 2016;72:367–379. https://doi.org/10.1016/j.autcon.2016.08.025

12. Semykina IYu, Kipervasser MV, Gerasimuk AV. Study of Drive Currents for Lifting Bridge cranes of metallurgical enterprises for early diagnosis of load excess weight. *Journal of Mining Institute*. 2021;247:122–131. http://doi.org/10.31897/PMI.2021.1.13

About the Author:

Imad Rizakalla Antipas, Cand.Sci. (Eng.), Associate Professor of the Fundamentals of Machinery Design Department, Don State Technical University (1, Gagarin sq., Rostov-on-Don, 344003, Russian Federation), SPIN-code: 7371-0223, ORCID, ScopusID, ResearchID, imad.antypas@mail.ru

Об авторе:

Имад Ризакалла Антибас, кандидат технических наук, доцент кафедры основ конструирования машин Донского государственного технического университета (344003, Российская Федерация, г. Ростов-на-Дону, пл. Гагарина, 1), SPIN-код: 7371-0223, ORCID, ScopusID, ResearchID, imad.antypas@mail.ru

Conflict of Interest Statement: **the author declares no conflict of interest.**

Конфликт интересов: **автор заявляет об отсутствии конфликта интересов.**

All author has read and approved the final manuscript.

Автор прочитал и одобрил окончательный вариант рукописи.

INFORMATION TECHNOLOGY, COMPUTER SCIENCE AND MANAGEMENT
ИНФОРМАТИКА, ВЫЧИСЛИТЕЛЬНАЯ ТЕХНИКА И УПРАВЛЕНИЕ

[Check for updates]

Features of Bearing on Underwater Object Using Phase Information of a Differential Stereo Sensor

Vladimir A. Shirokov [ID]**, Aigul I. Bazhenova** [ID][✉]**, Vladimir N. Milich** [ID]
Udmurt Federal Research Center, the Ural Branch of the Russian Academy of Sciences, Izhevsk, Russian Federation
✉ aigul_bazh@udman.ru

EDN: FPQRSJ

Abstract

Introduction. Safety of navigation and development of underwater mineral deposits require the accurate detection of various underwater objects. The literature discusses the issues of tracking their motion and trajectory. Sonar methods are proposed to maintain high accuracy of underwater object positioning. High accuracy of the bearing of stereo sensors with an ultrashort base is noted. However, this equipment is sensitive to the sampling rate of the signals, which causes "sampling noise". There are no publicly available publications dedicated to the solution to this problem. The presented study is designed to fill this gap. This work is aimed to study the possibility of obtaining data clarifying information about the bearing of underwater objects through using the phase information about echoed probing signals and an additional procedure for resampling the source data.

Materials and Methods. The location of the object was determined using the experimental complex for studying hydroacoustic sensors created by V.A. Shirokov and V.N. Milich at the Udmurt Federal Research Center, the Ural Branch of the Russian Academy of Sciences. A stereo sensor with a small base (30 mm) was used compared to the distance to the object (≈800–900 mm). Digital filtering methods and mathematical apparatus of correlation analysis of return hydroacoustic signals obtained by the phase method were used for data processing.

Results. The results of comparing two methods for determining the bearing on an object are presented: by the difference in the time of arrival of the pulse-leading edges and by the maximum of the cross-correlation function (CCF). The change in bearing as the object moves, is graphically shown. The use of the leading edge of the signal caused small outliers of values along the entire bearing curve (less than 0.12 rad). At the maximum CCF, emissions were recorded only in some areas, but they were quite significant (about 0.17 rad). It showed how to select points corresponding to a smoother and more valid object trajectory, and how to work with erroneous points. The presented method of error correction can be implemented programmatically. With a quasi-harmonious signal, rare measurements of the original signal are interpolated by frequent calculated values. Thanks to this virtual increase in the sampling rate (oversampling), intermediate indicators can be recorded in the digitized source data. Interpolation of the signal values by a cubic spline allowed us to obtain 20 points for 1 period of the signal instead of 5 points in the original version. In this case, the trajectory formed with the maximum CCF is more correct.

Discussion and Conclusion. The direction-finding problem can be solved with the accuracy required for practical application. Taking into account the factor of smoothness and continuity of the object's trajectory makes it possible to qualitatively correct the selection of the maximum of the cross-correlation function of the stereo sensor signals. The proposed methods have great potential for the development of underwater vision systems.

Keywords: determination of the location of an object in a hydraulic environment, phase direction finding, pulse-leading edges, cross-correlation function, sampling noise

Оригинальное эмпирическое исследование

Особенности определения пеленга на подводный объект с использованием фазовой информации дифференциального стереодатчика

В.А. Широков[ID]**, А.И. Баженова**[ID]✉**, В.Н. Милич**[ID]

Удмуртский федеральный исследовательский центр Уральского отделения Российской академии наук, г. Ижевск, Российская Федерация

✉ aigul_bazh@udman.ru

Аннотация

Введение. Безопасность судоходства и разработок подводных месторождений полезных ископаемых требуют точного обнаружения различных подводных объектов. В литературе рассматриваются вопросы отслеживания их перемещений и траектории движения. Предлагаются методы гидролокации, обеспечивающие высокую точность позиционирования подводных объектов. Отмечена высокая точность пеленга стереодатчиков с ультракороткой базой. Однако такое оборудование чувствительно к частоте дискретизации сигналов, что вызывает «шум дискретизации». В открытом доступе нет публикаций, посвященных решению этой проблемы. Представленное исследование призвано восполнить данный пробел. Цель работы — изучение возможности получения данных, уточняющих информацию о пеленге подводных объектов за счет использования фазовой информации отраженных зондирующих сигналов и дополнительной процедуры передискретизации исходных данных.

Материалы и методы. Местоположение объекта определяли с помощью экспериментального комплекса для исследования гидроакустических датчиков, созданного В.А. Широковым и В.Н. Милич в Удмуртском федеральном исследовательском центре Уральского отделения Российской академии наук. Использовали стереодатчик с малой базой (30 мм) по сравнению с расстоянием до объекта (≈800–900 мм). Для обработки данных применяли методы цифровой фильтрации и математический аппарат корреляционного анализа отраженных гидроакустических сигналов, полученных фазовым методом.

Результаты исследования. Представлены итоги сопоставления двух способов определения пеленга на объект: по разности времени прихода передних фронтов импульсов и по максимуму кросс-корреляционной функции (ККФ). Графически показано изменение пеленга при движении объекта. Использование переднего фронта сигнала обусловило небольшие выбросы значений вдоль всей кривой пеленга (менее 0,12 рад). При максимуме ККФ выбросы фиксировались лишь в некоторых областях, но были довольно значительными (около 0,17 рад). Показано, как выбрать точки, соответствующие более гладкой и валидной траектории объекта, и как работать с ошибочными точками. Представленный метод устранения ошибки можно реализовать программно. При квазигармоничном сигнале редкие измерения исходного сигнала интерполируются частыми вычисленными значениями. Благодаря такому виртуальному увеличению частоты дискретизации (передискретизации) можно фиксировать промежуточные показатели в оцифрованных исходных данных. Интерполяция значений сигнала кубическим сплайном позволила получить 20 точек на 1 период сигнала вместо 5 точек в исходном варианте. В этом случае более корректна траектория, сформированная с максимумом ККФ.

Обсуждение и заключение. Задачу пеленгации можно решить с точностью, необходимой для практического применения. Учет фактора гладкости и непрерывности траектории движения объекта позволяет качественно корректировать выбор максимума кросс-корреляционной функции сигналов стереодатчика. Предложенные методы обладают большим потенциалом для разработки систем подводного видения.

Ключевые слова: определение местоположения объекта в гидросреде, пеленгация фазовым методом, передние фронты импульсов, кросс-корреляционная функция, шум дискретизации

Информатика, вычислительная техника и управление

Introduction. Safety of navigation and work in underwater mineral deposits require high-quality detection of underwater objects and tracking their movements [1]. Hydroacoustic sensors are used in underwater surveillance systems. They capture the signal reflected from the object and provide for the calculation of its location using the trilateration method [2]. In this process, each sensor provides information about the time interval of the probing signal reflected from the object. In the case of using several sensors [3], it becomes possible to solve the problem of spatial resection and determine the coordinates of the observed object [4]. To increase the accuracy of measurements, it seems promising to use stereo sensors with an ultrashort base as a receiver [5], which allow obtaining phase information [6] and determining the bearing on an object [7]. The possibilities of using sonar data on remote underwater targets, as well as on the bearing of underwater objects [8] through the use of phase [9] or frequency [10] information of reflected probing signals have been studied.

At the same time, it is known that the signal sampling procedure causes errors in determining the parameters of the trajectory of underwater objects [11]. This applies to both distance measurements and bearing determination procedures. Digitization of the analog sensor signal, which is required for further digital processing, introduces the so-called "sampling error". The error caused by the signal amplitude quantization is estimated by the number of quantization levels of the analog-to-digital converter. The error caused by time sampling is proportional to the range of the quantization time interval and the stress rate. Therefore, the sampling frequency of the signal is sought to be as high as possible above the upper frequency of the signal itself. However, increasing the sampling rate in a number of cases is limited by the capabilities of recording equipment: processor, analog-to-digital converter, data transmission channels, data storage devices. The limited possibilities of sampling in time when performing trajectory measurements do not allow for accurate recording of the extreme values of the trajectory (range and bearing). As a result, the accuracy of measurement results decreases, and outliers appear on the fixed trajectories. To eliminate this disadvantage, it is necessary to study the potential of oversampling the digitized sonar signal. There are no publicly available publications dedicated to solving this problem. The materials of this article fill in the existing gap.

The objective of the presented study is to evaluate the possibilities of determining the bearing on an object using phase information, and to develop a phase method of bearing using the resampling of a digitized sonar signal.

Materials and Methods. An algorithm for determining coordinates using the direction-finding phase method is considered. The results of its testing for an object moving along a circular trajectory in an experimental pool are presented.

Setting up an experiment. During the experiments, an experimental assembly created by V.A. Shirokov and V.N. Milich at the Udmurt Federal Research Center of the Ural Branch of the RAS was used to determine the location of an object in the hydroenvironment with the direction finding by the phase method [12]. This is a laboratory measuring complex with a linear aqua medium in the form of an extended cylindrical tank (hydro waveguide) and a basin equipped with a system for generating test sonar signals. The installation elements used in the experiments are described in detail below.

1. Hydroacoustic signal emitter with known coordinates *S* (Fig. 1). An amplitude-modulated signal is used in the work [13].
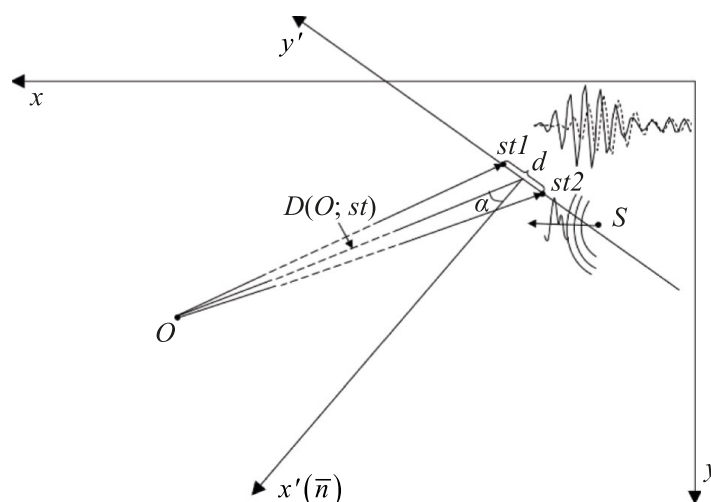

Fig. 1. Location of the receiving sensors (stereo sensor with two receivers *st*1 and *st*2) and emitter (*S*) in the plane of experimental tank (*xy*). Here, *d* — stereo sensor base; *D(O; st)* — distance between the stereo sensor and the object; α — bearing on the object; plate (*x'y'*) is formed by the plane of the stereo sensor and normal *n* to it

2. Reflecting object. In the experiment, an extended cylindrical object is used as a test object — a copper wire whose diameter (0.15 mm) is significantly less than the acoustic wave length (1.5 mm). In the presented work, the problem is solved on a plane; therefore, for the compilation of computational procedures for calculating coordinates, this object can be considered a point.

3. Stereo sensor that converts a sonar signal into an electrical one. The coordinates of each of the two receivers of the stereo sensor are known (see *st*1, *st*2 in Fig. 1).

4. Hardware-software complex that performs amplification, digitization and processing of sensor signals.

The measurement result is a recording file of the received two-channel signal.

Algorithm for processing measurement results. Using a stereo sensor with a small base (30 mm) compared to the distance to the object ($\approx$ 800–900 mm) allows us to apply simplified formulas.

Now then, we calculate the coordinates of the object under study in the system $x'y'$, formed by the plane of the stereo sensor and the normal to it. To do this, we use the algorithm that includes five stages.

1. Preprocessing:

− removal of the blind zone (the first N counts);

− signal filtering.

High-frequency filtering is used in the work.

2. Selecting informative fragments *imp*1, *imp*2 (in two channels) containing pulses reflected from the object under study. To do this, thresholding is performed according to amplitude A of the signal. The threshold is assumed to be equal to $p \times max(A)$ ($p = 0.5$).

This processing allows for determining the leading edge of the pulse (*BeginIndex*), reflected from the object. Sections [*BeginIndex*–0.5×*LenSignal*; *BeginIndex*+*LenSignal*] are cut from two signal channels. Here, *LenSignal* — length of the input signal. As a result, we get two signals *imp*1 and *imp*2 with a length of 1.5×*LenSignal*. Each of them contains the pulse reflected from the object.

3. Calculation of distance $D(O; st)$ between the object and the stereo sensor.

− Determination of the distance traveled by the pulse from the emitter to the object and from the object to the reception sensor, using formula $D(S,O,st)=BeginIndex \times \underline{dt} \times C$. Here, $C = 1475$ m/s — acoustic wave velocity, $dt = 0.2 \times 10{-6}$ s — sampling interval.

− Calculation of value

$$D(O,st) = \frac{D(S,O,st) - D(S,st)}{2}. \tag{1}$$

4. Determination of bearing α on object [14]:

$$\alpha = arcsin\left(\frac{\lambda \times F \times dt \times m}{d}\right), \tag{2}$$

where λ — wavelength; F — signal frequency; dt — sampling interval; m — difference in the arrival of the reflected pulse to two stereo sensors (in counts); d — base of the stereo sensor (in the presented study $\lambda = 1.5$ mm, $F = 1$ MHz, $dt = 0.2$ μs, $d = 30$ mm).

5. Calculation of the coordinates of the analyzed object in the system formed by the plane of the stereo sensor and its normal (Fig. 1), according to the formulas: $x' = D(O, st) \times cos(\alpha)$; $y' = D(O, st) \times sin(\alpha)$.

Determining the bearing on an object. Assume the condition of the smallness of the stereo base compared to the distance from the sensor to the object. In this case, the stereo sensor allows us to determine the bearing on the object using information about the phase difference of the received pulses previously reflected from the object, as well as the difference in the time of arrival of the leading edges of the pulses received by the stereo sensor (Fig. 2).
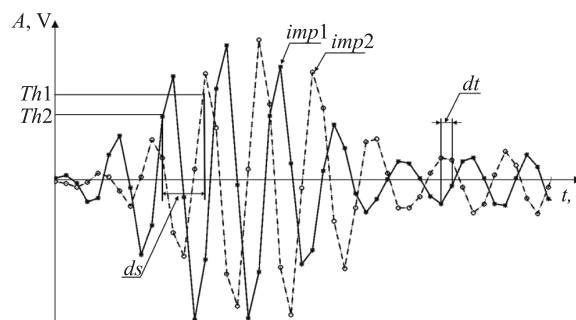

Fig. 2. Determination of difference in the moments of arrival of stereo signals ds, which are indicated by solid *imp*1(*t*) and dotted *imp*2(*t*) lines. *Th*1, *Th*2 — thresholds for the first and second stereo pair signals, respectively; *dt* — sampling interval; *A* — signal value in volts; *t* — time

To implement this approach, the following procedures are performed.

1. Identification of the moments of arrival of the leading edges of stereo signals using thresholding [15] with threshold $p \times max(A)$. In this paper, coefficient p is assumed to be 0.5 [16].

2. Calculation of difference ds (number of intervals dt) between the leading edges of the pulses registered in two receivers of the stereo sensor.

3. Calculation of bearing α by formula (1). We take value d for m.

With this method of calculating the phase shift, the leading edge of the signal is the main indicator of the pulse reflected from the object. The internal structure of the signal is not taken into account, which may be crucial for the correct determination of the bearing on the object. We take into account the similarity of the received signals and consider another approach to calculating the bearing — based on the cross-correlation function (CCF) of stereo signals. It is logical to determine the phase shift by the CCF maximum. The elements of the bearing calculation algorithm using CCF are described below.

1. Calculation of the CCF pulses arrived at two receivers of one stereo sensor: $r = xcorr(imp1, imp2)$. The value of function $xcorr$ at the shift of m of the second signal relative to the first is calculated as follows:

$$\text{xcorr}_{imp1,imp2}(m) = \begin{cases} \sum_{n=0}^{N-m-1} imp1_{n+m} \times imp2_n, & m \geq 0, \\ \text{xcorr}_{imp2,imp1}(-m), & m < 0. \end{cases}$$

Here, N — length $imp1$ and $imp2$, $-N<m<N$.

2. Determination of the maximum CCF and the corresponding shift dc (in counts).

3. Calculation of bearing α from formula (1) taking into account that value dc is taken as m.

Research Results

Testing the bearing determination methods. The presented methods for determining the bearing on an object (by the difference in the time of arrival of the pulse-leading edges and by the CCF maximum) were tested for an object moving along a circular trajectory in the experimental pool. A harmonic signal with a duration of 7 periods and a frequency of 1 MHz was used. Digitized stereo signals were recorded at 256 points of the object's trajectory. The digitization frequency was 5 MHz.

Figure 3 shows the change in bearing values as the object moves around the circle for the two proposed approaches (difference of the leading edges, CCF maximum).
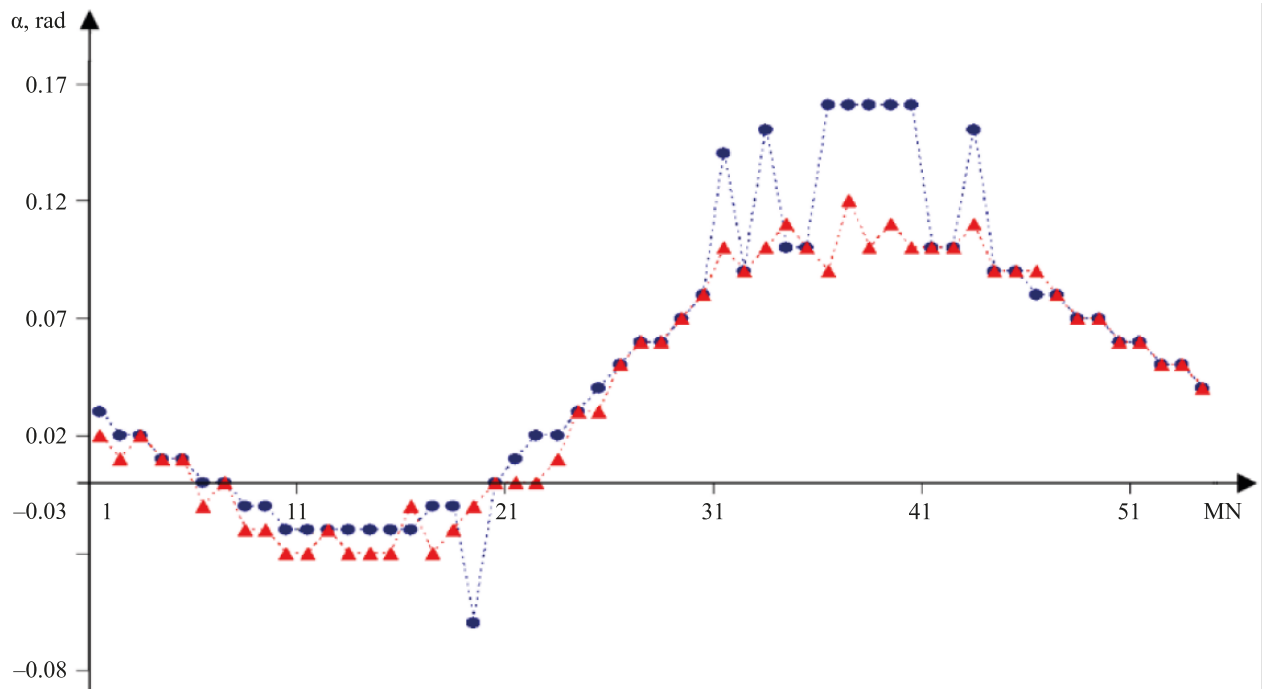

Fig. 3. Deviation of bearing α on the object making a circular motion. Indicators were obtained using two approaches (red marker — difference in the time of arrival of the leading edges of stereo signals, blue marker — CCF maximum). MN — measurement number, α — bearing on the object

When using the signal-leading edge (Fig. 3, red marker), small outliers of values are observed almost along the entire curve of the bearing on the object. When using the CCF maximum (Fig. 3, blue marker), only in some areas there are outliers of bearing values, but they are quite large. Perhaps this is due to the peculiarities of the object's movement in the area where the probing and reflected signals cross the zone of turbulence caused by the object's movement. When finding the phase shift of stereo signals using the CCF maximum, additional errors occur, which is then reflected in the calculated trajectory of the object. Also, outliers in the calculated bearing values may be due to an insufficiently high sampling rate. The values of these errors are significantly higher than the emission values observed for the method using the pulse-leading edge.

Figure 4 *a* presents the trajectories of the object, calculated using the global CCF maximum and its neighboring local maxima.
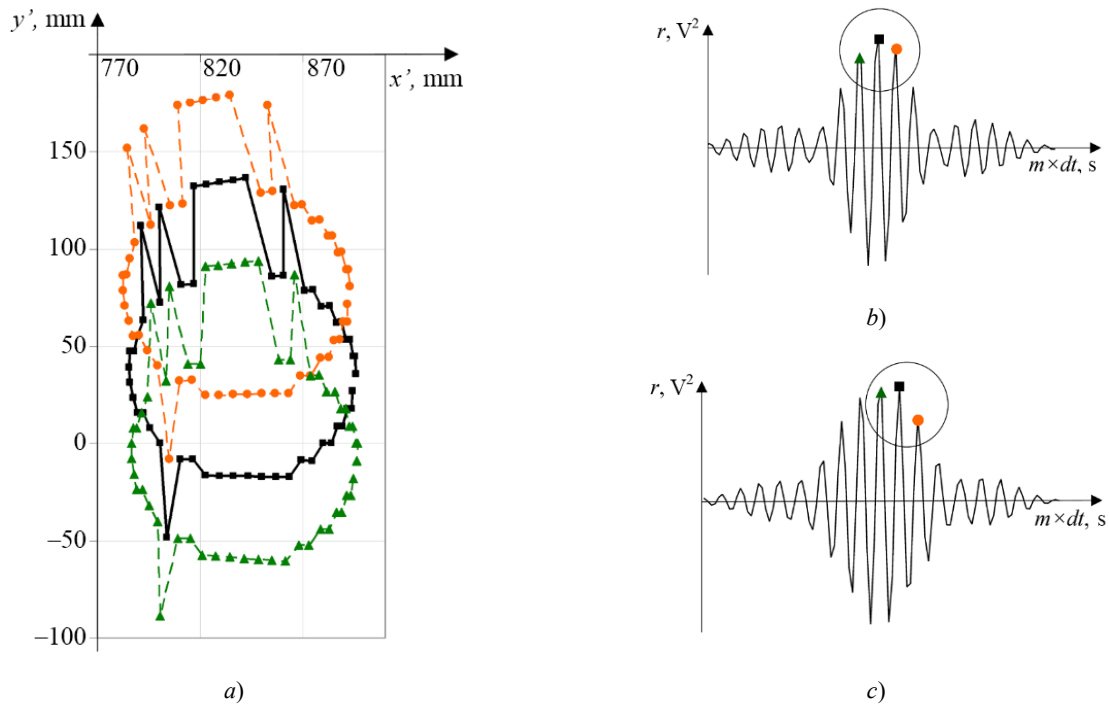

Fig. 4. Analysis of the trajectories of the circular motion of the object:
a — trajectories calculated using the global CCF maximum (black marker),
local nearest right CCF maximum (orange marker), local nearest left CCF maximum (green marker);
b — example of CCF, whose global maximum corresponds to the correct value of the coordinates of the object;
c — example of CCF, in which the left local CCF maximum corresponds to the correct value of the coordinates of the object

Using aprior information about the smoothness of the movement of the experimental object, it is possible to select points that correspond to a smoother and more valid trajectory. This approach is used in other works [17]. In Figure 4 *a*, at $x' \epsilon [800;870]$, $y' > 0$, the correct values are on the curve for the trajectory calculated from the left local CCF maximum. There are also erroneous points. If they are replaced by the points of the trajectory obtained as a result of using the right local CCF maximum, the correct value of the trajectory point can be calculated ($x' \approx 800$, $y' < 0$ in Fig. 4 *a*). This graphical method of error correction can be implemented programmatically.

Thus, at some points of the trajectory, the correct phase shift of the stereo signals required for calculating the bearing may correspond not to the global CCF maximum, but to one of the neighboring local extremes (Fig. 4 *b*, *c*). This shift of the CCF maxima may be due to an insufficiently high sampling rate of the signals. This also explains the stepwise nature of the resulting trajectory.

Taking into account the quasi-harmonicity of the signal, it is proposed to use interpolation of rare measurements of the original signal with frequent calculated values. This virtual increase in the sampling rate (oversampling) makes it possible to fix intermediate values in the digitized source data. Interpolation of the signal values by a cubic spline allowed us to obtain 20 points for 1 period of the signal instead of 5 points in the original version. Figure 5 shows the calculated trajectories of the object, formed with preliminary resampling of the signals.
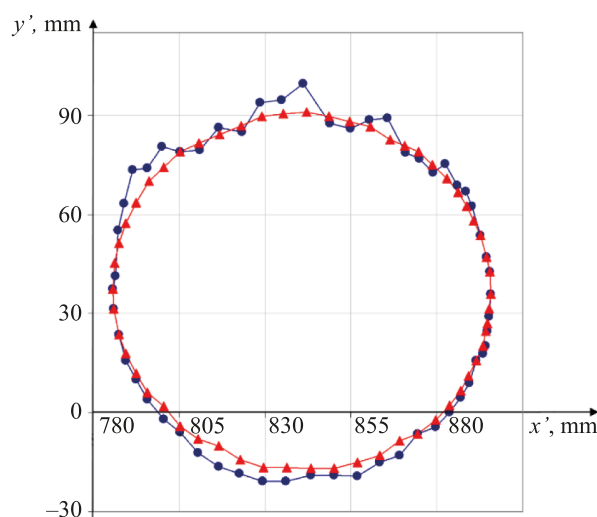
Fig. 5. Calculated object motion trajectories obtained for stereo signals with a virtually increased sampling rate:
blue marker — difference in the time of arrival of the signal-leading edges is used;
red marker — CCF maximum is used

The red line is the object's trajectory, obtained using the CCF maximum to calculate the bearing from pre-interpolated data. It seems to be more correct compared to a similar trajectory obtained using the difference in the leading edges of reflected pulses (blue line).

Discussion and Conclusion. Analysis of the features of determining the bearing on an underwater object using the mutual phase information of the differential stereo sensor signals makes it possible to draw the following conclusions.

− The difference in the arrival time of the pulse-leading edges recorded by the stereo sensor allows us to obtain bearing values indicating the direction of the object. The quality of the result depends on the accepted threshold value (used in determining the pulse-leading edge) and the variability of the amplitudes of the received signals.

− The application of the approach using the maximum of the cross-correlation function at an insufficient sampling rate of the initial signals leads to significant outliers in the calculated trajectory (Fig. 3).

− Resampling of signals through interpolation of the original quasi-harmonic signals using the CCF maximum for the calculation of the bearing and coordinates of the object provides obtaining a smooth trajectory (Fig. 5), corresponding to the smooth movement of the object in a circle. This approach requires significantly higher computational costs compared to the others discussed in this article. This may affect the speed of real-time signal processing.

Thus, the investigated possibilities of refining the phase direction finding method (resampling of digitized signals and using the CCF maximum) make it possible to effectively assess the trajectory of an underwater object.

The conditions for obtaining a smooth correct trajectory of the tracked object are described. The oversampling of interpolated quasi-harmonic stereo signals digitized with insufficient sampling rate serves this goal. At the same time, the bearing calculation method is used with the maximum of the cross-correlation function of the stereo sensor signals.

The data in Figure 5 confirm that the direction-finding problem can be solved with the accuracy required for practical application. Taking into account the factor of smoothness and continuity of the object's trajectory allows for the unique adjustment of the selection of the maximum of the cross-correlation function of the stereo sensor signals (Fig. 4).

The proposed methods are of great importance for the development of underwater vision systems.

References / Список литературы

1. Meng Joo Er, Jie Chen, Yani Zhang, Wenxiao Gao. Research Challenges, Recent Advances, and Popular Datasets in Deep Learning-Based Underwater Marine Object Detection: A Review. *Sensors.* 2023;23(4):1990. https://doi.org/10.3390/s23041990

2. Andreev MYa, Ochrimenko SN, Parshukov VN, Rubanov IL, Kozlovsky SV, Illarionov AA. Bistatic System for Searching Underwater Objects (Bistatic Hydrolocator). *Sensors & Systems.* 2019;233(2):50–56.

3. Matveeva IV, Shejnman EL. Determination of Current Target Coordinates in Bistatic Echo Ranging Mode at Uncertainty of Bearing Estimation. *Hydroacoustics.* 2017;31(3):9–12.

4. Matveeva IV, Sheinman EL, Shkol'nikov IS. Efficiency of Determination of Coordinates and Motion of Sea Objects at Bistatic Location of Moving Observing Systems. *Hydroacoustics.* 2016;26(2):28–32.

5. Arsent'ev V, Krivolapov G. Positioning of Objects in Hydroacoustic Navigation System with Ultrashort Base. *The Herald of the Siberian State University of Telecommunications and Information Science.* 2018;(4):66-75.

6. Matvienko YuV, Khvorostov YuA, Kuleshov VP. Peculiarities of Application of Scalar-Vector Sound Receivers in Systems for Control of Underwear Situation in Local Areas. *Underwater Investigations and Robotics.* 2022;42(4):4–15.

7. Terrachiano DS, Costanzi R, Manzari V, Stifani M, Caiti A. Passive Bearing Estimation Using a 2-D Acoustic Vector Sensor Mounted on a Hybrid Autonomous Underwater Vehicle. *IEEE Journal of Oceanic Engineering.* 2022;47(3):799–814. https://doi.org/10.1109/JOE.2021.3132647

8. Yanhou Zhang, Chao Wang, Qi Zhang, Lianglong Da, Zhaozhen Jiang. Bearing-only Motion Analysis of Target Based on Low-Quality Bearing-Time Recordings Map. *IET Radar, Sonar & Navigation.* 2024;18(5):765–781. https://doi.org/10.1049/rsn2.12519

9. Profatilova GA, Soloviev GN. Low Elevation Measurements Using Phase Method in the Presence of Interference. *Herald of the Bauman Moscow State Technical University. Series Instrument Engineering.* 2013;90(1):3–12.

10. Kaevitser VI, Krivtsov AP, Smolyaninov IV, Elbakidze AV. Frequency Method for Measuring the Angular Coordinates of an Underwater Vehicle by a Hydroacoustic System of Local Positioning. *Journal of Radio Electronics.* 2021;3:11. https://doi.org/10.30898/1684-1719.2021.3.1

11. Arsent'ev V, Krivolapov G. On the Characteristics of Phase Direction Finder of the Hydroacoustic System Drive for Delivering Autonomous Uninhabited Underwater Vehicle. *The Herald of the Siberian State University of Telecommunications and Information Science.* 2021;53(1):23–35.

12. Shirokov VA, Milich VN. Experimental Complex for Studying the Possibilities of Using Hydroacoustic Sensors in Underwater Vision Systems. *Vestnik IzhGTU named after M.T. Kalashnikov.* 2021;24(4):54–64.
2021;24(4):54–64. https://doi.org/10.22213/2413-1172-2021-4-54-64

13. Arsent'ev V, Krivolapov G. Hydroacoustic Phase Direction Finder with Amplitude-Modulated Navigation Signal. *The Herald of the Siberian State University of Telecommunications and Information Science.* 2021;54(2):14–26.

14. Matvienko YuV. Estimation of the Practically Attainable Accuracy of Modern Ultrashort Baseline Hydroacoustic Navigation Systems for Underwater Robots. *Gyroscopy and Navigation.* 2023;14(2):166.

15. Egorov SB, Gorbachev RI. Determination of Level and Time Thresholds for Detectors with Normalized Indicator Process. *Marine Intellectual Technologies.* 2020;2(2):144–147.

16. Abraham DA. *Underwater Acoustic Signal Processing. Modeling, Detection, and Estimation.* Cham: Springer; 2019. P. 457–619. https://doi.org/10.1007/978-3-319-92983-5

17. Denisov VP, Dubinin DV, Krutikov MV, Mescheryakov AA. Algorithm of Abnormal Direction Errors Rejecting for Phase Finder. *Proceedings of TUSUR University.* 2012;26(2):36–42.

About the Authors:
Vladimir A. Shirokov, Cand.Sci. (Eng.), Senior Researcher, Udmurt Federal Research Center, the Ural Branch of the Russian Academy of Sciences (34, T. Baramzina Str., Izhevsk, 426067, Russian Federation), SPIN-code: 9007–5928, ORCID, ResearcherID, shirokovva@udman.ru

Aigul I. Bazhenova, Cand.Sci. (Eng.), Researcher, Udmurt Federal Research Center, the Ural Branch of the Russian Academy of Sciences (34, T. Baramzina Str., Izhevsk, 426067, Russian Federation), SPIN-code: 5641-9184, ORCID, ResearcherID, ScopusID, aigul_bazh@udman.ru

Vladimir N. Milich, Cand.Sci. (Eng.), Leading Researcher, Udmurt Federal Research Center, the Ural Branch of the Russian Academy of Sciences (34, T. Baramzina Str., Izhevsk, 426067, Russian Federation), SPIN-code: 5612–2634, ORCID, ResearcherID, ScopusID, mili@udman.ru

Об авторах:
Владимир Анатольевич Широков, кандидат технических наук, старший научный сотрудник Удмуртского федерального исследовательского центра Уральского отделения Российской академии наук (426067, Российская Федерация, г. Ижевск, ул. им. Татьяны Барамзиной, 34), SPIN-код: 9007–5928, ORCID, ResearcherID, shirokovva@udman.ru

Айгуль Илсуровна Баженова, кандидат технических наук, научный сотрудник Удмуртского федерального исследовательского центра Уральского отделения Российской академии наук (426067, Российская Федерация, г. Ижевск, ул. им. Татьяны Барамзиной, 34), SPIN-код: 5641-9184, ORCID, ResearcherID, ScopusID, aigul_bazh@udman.ru

Владимир Николаевич Милич, кандидат технических наук, ведущий научный сотрудник Удмуртского федерального исследовательского центра Уральского отделения Российской академии наук (426067, Российская Федерация, г. Ижевск, ул. им. Татьяны Барамзиной, 34), SPIN-код: 5612–2634, ORCID, ResearcherID, ScopusID, mili@udman.ru

Claimed Contributorship:
VA Shirokov: basic concept formulation, research objectives and tasks, conducting experiments.
AI Bazhenova: processing and analysis of the results, preparation of the text and figures.
VN Milich: tasks formulation, drawing conclusions, finalizing the text.

Заявленный вклад авторов:
В.А. Широков: формирование основной концепции, цели и задачи исследования, проведение экспериментов.
А.И. Баженова: обработка и анализ результатов, подготовка текста и рисунков.
В.Н. Милич: постановка задачи, формирование выводов, доработка текста.

Conflict of Interest Statement: **the authors declare no conflict of interest.**

Конфликт интересов: **авторы заявляют об отсутствии конфликта интересов.**

All authors have read and approved the final manuscript.

Все авторы прочитали и одобрили окончательный вариант рукописи.